All-Optical Manipulation and Hyperfine Characterization of Silicon T-centres

by

Nicholas Brunelle

B.Sc., University of Washington, 2019

Thesis Submitted in Partial Fulfillment of the
Requirements for the Degree of
Master of Science

in the
Department of Physics
Faculty of Science

© Nicholas Brunelle 2023
SIMON FRASER UNIVERSITY
Spring 2023

Copyright in this work is held by the author. Please ensure that any reproduction or re-use is done in accordance with the relevant national copyright legislation.

Declaration of Committee

Name:	**Nicholas Brunelle**
Degree:	**Master of Science**
Thesis title:	**All-Optical Manipulation and Hyperfine Characterization of Silicon T-centres**
Committee:	**Chair:** Igor Herbut Professor, Physics
	Stephanie Simmons Supervisor Associate Professor, Physics
	Michael Thewalt Committee Member Professor Emeritus, Physics
	Jeff Sonier Examiner Professor, Physics

Abstract

With the continued growth of different platforms towards large-scale quantum computation and quantum communication, the development of new systems that provide quantum memory and networked entanglement continues. Spin-photon interfaces are one such group of systems, which aim to combine the best properties of long-lived spin qubits with the ability to transmit information and entanglement through photons. Silicon, a platform with mature microelectronic and nanophotonic fabrication industries, is home to the T-centre, a spin-photon interface with emission at 1326 nm, which is in the telecommunications O-band. The properties of the T-centre must be determined in order to efficiently control T-centre spins for quantum computation and quantum communication applications.

In this thesis we take the first steps towards all-optical control of the T-centre through simulation and experiment. When compared to direct magnetic controls, optical control methods can have higher speeds and improved scalability. We compare different optical control techniques through simulations. To carry out the measurements necessary to eventually achieve optical control, we developed a multi-channel ultra-stable laser system with a linewidth less than 2.6 kHz. We then demonstrate the first steps towards all-optical control of T-centre qubits using T-centre ensembles in isotopically enriched ^{28}Si. First, we measure optical Rabi oscillations, of which Rabi frequencies > 7 MHz were observed. We also measure the ground state hyperfine structure, enabling a determination of the hydrogen spin hyperfine tensor [34]. We find that the zero-field hyperfine splittings of the T-centre are 3.482(3) MHz, 3.713(4) MHz, and 4.268(3) MHz. Finally, we report the first observation of optical coherent population trapping with the T-centre. These measurements and simulations identify conditions for full optical control of the T-centre in the context of both ^{28}Si ensembles and single centres in nanophotonic devices.

Keywords: Spin-photon interface; silicon T-centre; optical control; hyperfine; coherent population trapping

Acknowledgements

I would like to respectfully acknowledge that SFU is on unceded Coast Salish territory, the traditional territories of the Squamish, Musqueam, Tsleil-Waututh, Katzie, and Kwikwetlem peoples.

I want to begin by thanking my family for their endless support and guidance over the years that has helped shape who I am. From music, to sports, to academics, my parents have always encouraged me to pursue my interests. With these interests leading to a graduate degree, I am thankful to be able to lean on my parents' wisdom, having pursued similar levels of education. Through all the ups and downs, they have always been there for me, and I couldn't imagine making it this far with anyone else. Thank you Mom, Dad, and Megan.

I am thankful to have had the supervision of Stephanie Simmons and Mike Thewalt through the course of this degree. I was instantly hooked by Dr. Simmons' vision and enthusiasm for the future of the field, which not only drew me to her lab, but also gave me the confidence to fully commit myself to this field of physics. Her ability to piece together the minutia of individual experiments to the bigger picture of where the science is heading has been a useful source of guidance and instruction whenever I hit roadblocks in my work. I am fortunate that I can also rely on the experience Dr. Thewalt. When it comes to experimental design and debugging, his wisdom is second to none, and I doubt I could have completed half the work I did in these past two years without his assistance. In addition, his infectious curiosity has inspired a similar curiosity in myself, making the struggles of experimental work much more enjoyable.

The entire crew at SQT has been amazing to work with, and I am thankful to have had the pleasure to work with and befriend you all. There are a few particular members who have been integral to the completion of this thesis that I would like to start with. Daniel Higginbottom, who has been a mentor to me since day one, has been a vital source of instruction and guidance. So many of the things that went into this thesis I did not know existed until he first showed them to me. Whenever a problem arose, I knew I could go to Daniel, as he would either have a solution or somewhere I could begin looking to find a solution. Josh Kanaganayagam was closely involved with the ODMR measurements used to determine the hyperfine tensor, and conducted all of the analysis and fitting of the data. It has been a pleasure collaborating with him, bridging theory and experimental work.

Since he joined the lab, Mehdi Keshavarz has been my partner in crime, and was by my side for many of the measurements that make up this thesis, particularly the hyperfine measurements. Together we have had many great conversations trying to decipher the experimental results we have found, which have been of great help for my analysis in this thesis. Myles Ruether created the sample mount for the disk magnets used in part of this work and was very accomodating with my partially-formulated design requests for other parts used in related measurements that ultimately didn't make it into this thesis. In the lab Myles has helped me to understand the inner workings of our cryogenic systems, while out of the lab he has been a great ski buddy for when we need to give our minds a rest. Adam, Amir, Camille B., Camille C., Chloe, and Mehdi all provided insightful feedback on this thesis that helped shape it into its current form, and I cannot thank them enough for this help. I would also like to thank the other members of SQT for their support and camaraderie, who include Austin, Ian, Larissa, Leea, Melanie, Michael, Moein, and Yehudah. One final shoutout to those who frequent Grotto for the great discussions both on and off topic.

While not a large distance, moving to Canada has been a big change in my life, and it would not have gone so smoothly without those who have helped welcome me into the area. This includes all those I have mentioned so far with regards to SQT, but I would also like to mention Adam, Ashwin, Jon, Motoki, Ryan, and my ultimate frisbee teammates for making this area feel more like home.

Finally, I would like to thank Inky, Max, Cleo, and Clyde. Your endless love has meant the world to me.

Table of Contents

List of Tables

List of Figures

Chapter 1

Introduction

1.1 Quantum Computation

One of the hallmarks of the past century is the invention and rapid development of the transistor-based computer. The increased ubiquity of computers in our daily lives demonstrates the power of this tool to change our lives in many ways. From automating tasks to keeping people interconnected, we have become reliant on computers for everyday tasks.

The modern computer relies on silicon-integrated microelectronic circuits with long-distance internet communication utilizing a system of optical fibers, repeaters, and amplifiers designed for infrared wavelengths referred to as the telecommunications (telecom) bands [36, 66, 53]. Integrated transistors store information as a binary digit (bit) through gating current in an "on" or "off" state [43, 32]. The state of a bit is typically represented by a 0 or 1. In order to efficiently scale up the computing power of these silicon integrated circuits, the size of transistors has been shrinking towards a fundamental atomic limit, at which the effects of quantum mechanics will start to interfere with their functionality [57]. Even if transistor size was not limited by quantum mechanics, certain problems scale inefficiently with the best known classical algorithms, making them infeasible on the largest supercomputers. Meanwhile, quantum computers offer exponentially faster algorithms that make certain problems tractable in comparison to the classical counterparts [51].

The ability for a quantum bit (qubit) to be held in a superposition distinguishes the quantum computer from its classical counterpart. When measured, the state must collapse to either a 0 or 1, with the probability of measuring each dependent on the state coefficients given by the superposition. Entanglement is an extension of superposition, which involves an inseparable superposition of two or more qubits, a phenomena irreproducible in a classical system [31]. Due to state collapse in readout, classical and quantum computing have the same range of solvable problems given sufficient time, though the computation time of certain classical algorithms are exponentially slower than the corresponding quantum algorithms [51]. Quantum computing utilizes entanglement and superpositions during

computation before state collapse to achieve this speed up. There are currently about 60 algorithms that achieve a polynomial or greater-than-polynomial speedup over classical algorithms, including Shor's algorithm for prime factorization and an algorithm for solving systems of linear equations [60, 25, 31]. Showing that these algorithms can produce improvements in real quantum systems, known as quantum advantage, has become a test for the viability of quantum computing [3].

1.2 Quantum Computing Platforms

Several platforms, such as superconducting circuits, photonics, and spins have been pursued for quantum computation [1]. So far, the most developed platforms are the superconducting circuits and photonics. IBM has announced the launch of the largest quantum computer to date with 433 qubits [39], which is built upon superconducting qubits. However, these systems are currently limited by short coherence times and surface code connectivity [38]. Photonic-based quantum computers have comparatively better connectivity through the wiring of optical fibres and photonic devices, but lack a long quantum memory [46]. Despite this, quantum advantage through photonic qubits has been demonstrated through Gaussian boson sampling [71, 46].

Meanwhile, a number of spin qubit platforms exist including ion traps, 2D materials, quantum dots, and solid state defect centres, which can all have long coherence times [1]. In order for these spin systems to function as a quantum computer, they will need long coherence times, controllable spin states, and a practical method for entangling separate qubits. The coherence time is a measure of how long the phase of the superposition state remains well-defined, setting a limit on how long quantum information can be stored. One of the most promising avenues towards spin qubit quantum computers is via spin-photon interfaces, which possess a spin quantum memory and state-dependent single-photon emission [1, 5]. A spin-photon interface emitting indistinguishable photons allows for remote, optically-mediated spin entanglement [5]. Conditional gates and single-qubit gates can be created when coupling a spin-photon interface to a photonic cavity with spin-dependent transitions, which forms the basis for a quantum computer [49].

As a platform for generating entanglement between distant qubits, spin-photon interfaces enable quantum communications on preexisting networks [52]. Quantum communication could be carried out through a series of fibers and quantum repeaters that propagate entanglement [12, 14]. Such communications open the door for quantum cryptography schemes, such as the BB84 and Y-00 protocols [9, 64]. Quantum networks have already been developed on the existing system of telecom wavelength optical fibers that compose long-distance classical communication systems for use in quantum communication protocols [19].

1.3 Solid-State Defects

Solid-state defects have garnered attention as spin-photon interface candidates thanks to pioneering work on the nitrogen-vacancy (NV) centre in diamond [5]. Such experiments include room temperature spin readout [20], dynamical decoupling (periodic control to reduce decoherence) [41], entanglement of electron and nuclear spins [29, 65], and spatially separated spin entanglement [12, 54, 26]. The NV centre has an optically accessible electron spin, potentially coupled nearby nuclear spins, room temperature spin coherence, and photonic structure integration. However, its lack of telecom emission coupled with the difficulties of diamond photonics impact the long-term feasibility of the NV centre as a spin-photon interface for quantum computing [5]. Other colour centres being researched in diamond include the negatively-charged silicon vacancy (SiV^-) centre, the germanium vacancy (GeV) centre, the neutrally-charged silicon vacancy (SiV^0) centre, and the tin vacancy (SnV) centre [5]. These defects also lack emission in a telecom band, which would allow for low-loss optical networking, and require the use of diamond photonics, a less-developed field than silicon photonics that has production difficulties.

Aside from diamond, other solid-state platforms for spin-photon interfaces exist, such as silicon carbide (SiC), rare earth ion (REI) doped crystals, and silicon [1, 5]. REI crystals have emitters with narrow transitions and long coherences in the telecom band, though suffer from low emission rates [1]. Silicon stands out due to its ubiquity in integrated circuits and integrated photonics that has lead to nanoscale complementary metal–oxide-semiconductor (CMOS) fabrication [36, 15]. Given the classical systems in place, it is advantageous to build a quantum computer on the same platform to make use of the many advancements already achieved in classical systems. With these fabrication capabilities, photonic devices could be developed around a spin-photon interface. Therefore, it is advantageous to find a spin-photon interface in silicon that emits in the telecom band with long coherence times, narrow linewidths, and efficient transitions.

1.4 Donors and Damage Centres in Silicon

Silicon hosts donors/acceptors and radiation damage centres, which can contain spin qubits. With silicon photonic devices such as waveguides, grating couplers, and cavities, emission from a spin-photon interface can be networked to telecom optical fibers in order to produce and distribute entanglement. Finally, the Avogadro project demonstrated high isotopic purification of silicon, a feat not seen in diamond [8]. Isotopic purification leads to increased uniformity between local environments within the substrate, reducing inhomogeneity and decoherence [16, 10, 17, 62].

The optical and spin properties of donors/acceptors and damage centres in silicon improve through isotope purification [16, 10, 17, 62]. Natural silicon (^{nat}Si) has an isotope

abundance of 92.23% ^{28}Si, 4.67% ^{29}Si, 3.10% ^{30}Si. Of these isotopes ^{29}Si possesses a non-zero spin ($I = 1/2$). By purifying the isotope composition to nearly 100% ^{28}Si, the homogeneity of the silicon substrate is improved in regards to both mass and spin. The optical transitions of the qubits broaden inhomogeneously due to shifts in the local mass environment from isotope variation, and the coupling of the qubit spin to the nuclear spin of the ^{29}Si leads to shorter spin coherences [16].

In this thesis we focus on the T-centre, one of the known radiation damage centres in silicon. The T-centre emits near 1326 nm in the telecom O-band and splits under magnetic field due to the electron and nuclear spins in the ground state and the hole and nuclear spins in the excited state [10]. The T-centre matches the criteria of a spin-photon interface in silicon that emits at a telecom wavelength. The specific characteristics of the T-centre will be given in §2.1.

1.5 Optical Control of Spin Qubits

Spin-photon interfaces have spin-dependent optical transitions, but may lack direct optical transitions between the spin qubit states, as with the T-centre. A spin-photon interface may use an optical interface for initialization, readout, and remote entanglement, so using lasers to manipulate the spin could reduce the resource overhead of wiring involved in scaling up a cryogenic quantum computer. Optical fields also allow for faster driving between spin states compared to directly addressing the spins [6].

This desire to control spin qubits using optical transitions has lead to the development of all-optical control schemes [24, 18, 7, 6, 68, 2, 11]. Through coherent laser excitation of two optical transitions to a common excited state, a so-called 'Raman' transition is formed between the two ground states. When the two ground states encode a qubit the optical Raman transition provides an indirect means of qubit control. Physical implementation of all-optical control has already been shown for a number of spin-photon interfaces, which we will discuss in detail in §2.5 [59, 55, 37, 50, 22, 18, 6, 68].

No previous attempts have been made to optically control the spin qubits of the silicon T-centre. Such a protocol for all-optical control of the T-centre may allow for high speed, high fidelity, and arbitrary spin rotations. Since optical control will focus on controlling the ground state, a good understanding of the ground state structure of the T-centre will be required, which, prior to this work, has not been well characterized.

1.6 Thesis Structure

In this thesis we determine the conditions under which optical control of the T-centre is feasible through simulation and experimental characterization. In Chapter 2 we discuss the relevant T-centre properties, the theory of atom-light interactions and the hyperfine

interaction, and optical control schemes. In Chapter 3 we simulate T-centre optical control. These simulations compare the fidelity of different optical control schemes for ^{28}Si T-centre ensembles and isolated T-centres in ^{nat}Si. The results of these simulations inform the experimental choices made in this work, as well as provide insight into the viability of optical control of the T-centre.

Chapter 4 lays out the experimental design used for the measurements in this work. Three major apparatuses were constructed for this work. First, a multi-channel ultra-stable laser system was built in order to ensure the proper characterization of optical coherent population trapping (CPT), which requires narrow-linewidth, coherent excitation. This system may provide the necessary coherent excitation for optical control in future work. Second, we made a static magnetic field apparatus with a sample rotation mount, which allows for the spectral isolation of T-centre orientations. We used the static magnetic field apparatus to measure optical Rabi oscillations. Third, we built a variable magnetic field apparatus for characterization of the ground state structure and observing optical CPT.

Chapters 5 through 7 describe the results of this work. In order, these chapters detail findings with regards to optical Rabi oscillations, the T-centre hyperfine structure, and optical CPT, all performed on ^{28}Si T-centre ensembles. The demonstration of the optical Rabi oscillations in Chapter 5 shows the necessary optical powers needed to drive such oscillations in our ensemble apparatus. The ground state structure informs control schemes for the electron and nuclear spin qubits. Therefore, it is essential that the tensor which represents the anisotropic hyperfine coupling to the hydrogen nuclear spin is determined. This characterization is performed in Chapter 6. With the hyperfine tensor it will be possible to determine in advance the static magnetic field(s) at which the T-centre can be optimally utilized with regards to storing and processing quantum information in spins. Finally, the measurement of optical CPT in Chapter 7 demonstrates the ability to coherently drive the T-centre into a dark state, a necessary component of optical control.

Chapter 2

Background & Theory

Before discussing the work done in this thesis, we first describe the known properties relevant to the silicon T-centre to provide the context of our system for optical control considerations. This is followed by two sections detailing the relevant theory for atom-light interactions and hyperfine structure. The tools developed in these sections help to explain the mathematics in the following section on optical control theory. Finally, this chapter ends with a literature review on optical control.

2.1 The Silicon T-centre

In trying to determine chemical impurities in irradiated silicon, a number of spectral lines corresponding to radiation damage centres were discovered and labelled during the 1970s and 1980s [48]. A number of these centres were found to emit at telecom wavelengths, including the T-centre [48, 28].

2.1.1 Energy Level Structure

Recent studies have determined key characteristics of the T-centre in isotopically purified ^{28}Si [10]. The T-centre is believed to have two carbon atoms bonded together sharing a lattice site in the silicon with one hydrogen attached to a carbon and an unpaired electron from the dangling bond of the other carbon [10]. The electron spin couples through the hyperfine interaction to the nuclear spin of the hydrogen. This hyperfine interaction is known to be anisotropic [10], but the corresponding hyperfine tensor was, prior to this work, unknown.

Under resonant photoexcitation the T-centre gains a bound exciton (BE) such that the two bound electrons pair off into a spin-0 state, leaving only the hole spin system [10]. At zero field the hole spin states split 1.76 meV due to internal stress caused by the centre geometry, producing two split doublets labelled TX_0 and TX_1 with energies of 935.06 meV and 936.82 meV [10]. A hole-burning measurement conducted in the course of this project and reported in [21] demonstrated that the ground state at zero field comprises a high

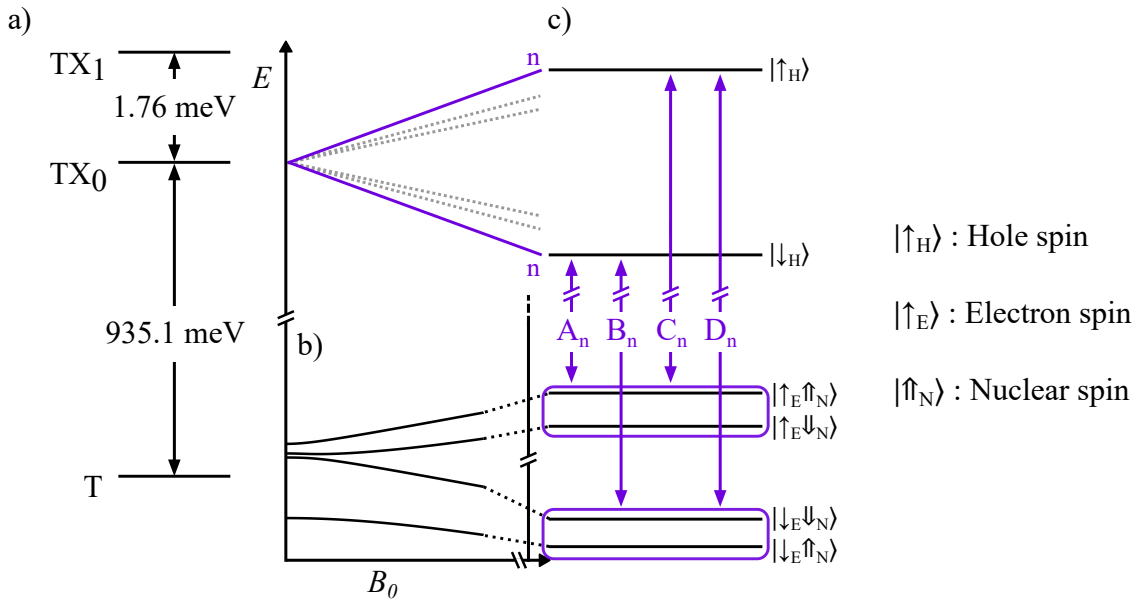

Figure 2.1: T-centre energy level diagram. a) Coarse T-centre structure for the ground and first excited states. The ground state and two lowest excited states of the T-centre are labeled T, TX_0 and TX_1 respectively. b) Low to intermediate field ground state structure. The exact level structure depends on the orientation of the magnetic field. c) Example intermediate field splitting of the ground and excited states. The exact eigenstate ordering in the ground state will depend on the field direction, but we shall use this ordering in all following figures for consistency. The optically resolved transitions A–D between the electron and hole spin states are shown for one of the 24 T-centre orientations labelled 'n'.

energy broken-symmetry triplet and low energy singlet split by 3.85(1) MHz. The energy level structure of the T-centre is shown in Figure 2.1.

TX_0 splits under magnetic field, and, for a given T-centre, there will be four lines corresponding to the four different transitions between the ground and excited states (A–D in 2.1). Due to anisotropy in the hole spin, an ensemble of T-centres will produce PL spectra with up to 48 lines from 12 distinguishable orientation subsets, depending on magnetic field magnitude and direction [10]. Each subset will have a different effective hole g-factor (g_h) for a given magnetic field direction (though it is also possible that different orientations overlap for specific field directions). The electron spin g-factor (g_e) has been measured to be 2.005(8), while g_h has been seen to vary from 1.069 to 3.457 depending on orientation, with a theoretical range from 0.85 to 3.50 [10, 27]. Depending on whether g_e is larger or smaller than g_h, the ordering of the transitions B and C in energy can swap. The energy difference between A/B as well as C/D will always correspond to the electron spin splitting regardless of orientation.

2.1.2 Optical Properties

The ability to perform optical control requires optical transitions with narrow linewidths. For the T-centre we focus on the zero-phonon line (ZPL) of TX_0, as it corresponds to the direct optical transitions from the ground to excited states, allowing for coherent optical driving.

Much like other systems in silicon [16, 35, 70, 69, 62, 17], isotopic purification of the host silicon benefits the T-centre by narrowing the ZPL linewidth. While in ^{nat}Si the inhomogeneous distribution of T-centres produces a 6.5 GHz line at 1.4 K, T-centre ensembles in ^{28}Si produce an inhomogeneous linewidth of 33 MHz at 1.4 K [10]. Follow-up hole-burning experiments carried out during this work determined that the instantaneous homogeneous linewidth of the T-centre in ^{28}Si at 1.4 K was only 690(10) kHz, nearing the 170 kHz lifetime limit [21].

The T-centre ZPL linewidth has a thermal dephasing linked to the activation energy of the TX_0-TX_1 splitting

$$\gamma(T) = P_0 + \frac{P_T}{\exp(E_a/k_B T) - 1}, \tag{2.1.1}$$

with the parameters given in Table 2.1. As these numbers were fit from an ensemble measurement, it is likely that the zero temperature value does not represent the true dephasing at 0 K, but rather includes an inhomogeneous distribution.

Parameter	Value
0 K dephasing (P_0)	0.137 μeV
Temperature dephasing coefficient (P_T)	78 μeV
Activation energy (E_a)	1.6 meV

Table 2.1: T-centre temperature-dependent dephasing coefficients [10].

The transition energies of solid state emitters vary in time in response to local environmental effects such as neighboring charges that fluctuate. Such 'spectral diffusion' acts as a broadening mechanism on the transition. Measurements of the spectral diffusion in bulk ^{nat}Si and ^{28}Si reveal similar values of 16(7) MHz and 27(12) MHz respectively [45]. Reducing spectral diffusion is critical for improving the indistinguishability of the T-centre, which is necessary for rapidly generating entanglement [33], as well as improving the effective optical drive strength of optical control schemes.

Through photoluminescence (PL) measurements it has been determined that the BE in TX_0 has a lifetime of 940(1) ns and the ratio of the ZPL emission to total emission, ZPL plus phonon sideband (PSB), known as the Debye-Waller factor (DWF), is 0.23 [10]. It is not currently known if any non-radiative decay paths exist for the T-centre, but recent

measurements determined a lower bound on the radiative efficiency of 3% [27]. These properties directly impact the efficiency of driving the ZPL, where a higher efficiency will require less optical excitation power.

2.1.3 Spin Properties

To date, optical linewidths have been insufficient to resolve hyperfine structure at achievable fields. However, direct manipulation of the electron and nuclear spins has been shown using RF and MW frequencies at field through the use of optically detected magnetic resonance (ODMR) [10]. These experiments utilize the electron paramagnetic resonance (EPR) and nuclear magnetic resonance (NMR) transitions for the electron spin and nuclear spin splitting respectively while also pumping an optical transition that addresses the two levels for a given ground state electron spin.

Parameter		^{28}**Si**	$^{\mathbf{nat}}$**Si**	$^{\mathbf{nat}}$**Si SOI**	
				Ensemble	**Single**
Optical	Linewidth	33(2) MHz (inhom.) [10] 0.69(1) MHz (inst. hom.) [21]	6.5(2) GHz [10]	18.0(1) GHz (inhom.) [45] 54(1) MHz (inst. hom.) [21]	660 MHz [27]
	Lifetime ($1/\Gamma$)	940(10) ns [10]		802(7) ns – 960(10) ns [27] [21]	
	Spectral diffusion	27(12) MHz [45]	$< 16(7)$ MHz [45]	1.0(2) GHz [45]	$0.4 - 2$ GHz [27]
	DWF (η_{ZPL})	0.23(1) [10]	-	-	-
	Radiative efficiency (η_{R})	-	-	-	$> 3\%$ [27]
Electron spin	Lifetime ($T_{1\mathrm{e}} = 1/\Gamma_{\mathrm{e}}$)	> 16 s [10]	-	$> 80(50)$ ms [21]	$> 1.2(1)$ ms [27]
	Coherence time ($T_{2\mathrm{e}} = 1/\gamma_{\mathrm{e}}$)	> 2.1 ms [10]	-	-	-
Nuclear spin	Lifetime ($T_{1\mathrm{n}} = 1/\Gamma_{\mathrm{n}}$)	> 16 s [10]	-	-	-
	Coherence time ($T_{2\mathrm{n}} = 1/\gamma_{\mathrm{n}}$)	> 1.1 s [10]	-	-	-

Table 2.2: Best recorded values for T-centre characteristics across different silicon platforms.

Bergeron et al. measured the effective hyperfine constant (A_{eff}) for three subsets, which represents the hyperfine interaction for a given orientation (see §2.3), finding effective hyperfine values: $A_{\text{eff}} = 2.93$ MHz, 2.57 MHz, 0.40 MHz [10]. By pulsing the EPR and NMR transitions in a Hahn-echo protocol, the electron and nuclear spin were found to have lifetimes ($T_{1\text{e,n}}$) greater than 16 s and coherences ($T_{2\text{e,n}}$) of 2.1 ms and 1.1 s respectively [10]. These coherences and lifetimes represent limits for how long quantum information can be stored in the T-centre ground state. Optical spin manipulation must operate significantly faster than these bounds.

2.1.4 Final Notes

The T-centre characteristics described above detail the best observed optical and spin properties as they relate to implementing optical control. In this work we consider both T-centre ensembles in bulk, isotopically-enriched ^{28}Si, which account for most of the above-mentioned characteristics, as well as single centres in silicon-on-insulator (SOI) photonic devices. To do so we use the best measured properties from these respective platforms, with consideration of near-term improvements. A summary of these T-centre characteristics is given in Table 2.2. Ultimately, we decided to perform our measurements on bulk ^{28}Si T-centre ensembles.

2.2 Atom-Light Interactions

To develop a framework for optical control, we need to understand how atom-like systems interact with optical fields. The final simulations utilize a four-level model, but here we build up the core concepts found in simpler systems, which we also use for simulation and analysis, where computation time with the four level system is prohibitive. We use density matrix formalism to describe the atom-light interactions involved in optical control. This not only provides intuition as to the inner workings of optical control schemes, but also provides a mathematical basis upon which simulations of the T-centre can be built with regards to optical control.

2.2.1 Density Matrix Formalism

A quantum mechanical particle's state exists in a waveform, which in a pure state is denoted as $|\psi\rangle$ in bra-ket notation, whose evolution in time is governed by a Hamiltonian, $\hat{H}$, and the Schrödinger equation [40]

$$i\hbar \frac{\partial}{\partial t} |\psi(t)\rangle = \hat{H} |\psi(t)\rangle \ . \tag{2.2.1}$$

$|\psi\rangle$ can be written as a superposition of the basis states $|n\rangle$ that represent eigenstates of an observable

$$|\psi\rangle = \sum_n c_n |n\rangle \,, \tag{2.2.2}$$

where the c_n are complex numbers such that $\sum_n |c_n|^2 = 1$. The $|c_n|^2$ values represents the probability of measuring eigenstate n.

The system may be in a mixed state rather than a pure state, which is a statistical mixture of pure states. For a more general description of quantum states, we make use of a density operator $\hat{\rho}$, which is given by the relation [40]

$$\hat{\rho} = \sum_{n,m} \rho_{nm} |n\rangle\langle m| \,, \tag{2.2.3}$$

where the coefficients ρ_{nm} are the matrix elements of ρ. For pure states $\mathrm{Tr}(\hat{\rho}^2) = 1$.

For a pure state these coefficients correspond to the combined coefficients $c_n c_m^*$. The diagonal elements, ρ_{nn}, are the probabilities of measuring the system in the states $|n\rangle$, referred to as the population in each state. The off-diagonal terms, ρ_{nm}, are referred to as coherences as they are related to the phase difference between the components c_n and c_m. With the polar representation of c_n as $r_n e^{i\phi_n}$, we can write the off-diagonal terms as: $\rho_{nm} = r_n r_m e^{i(\phi_n - \phi_m)}$. By definition, these coherence terms obey the relationship $\rho_{nm} = \rho_{mn}^*$. The state is considered to be mixed if $\mathrm{Tr}(\hat{\rho}^2) < 1$, which means it cannot be simplified down to some state $|\psi\rangle$.

2.2.2 Two-Level Atom Dynamics

Here we consider the case of an atom with two levels; a ground state $|g\rangle$ and an excited state $|e\rangle$. The transition energy E_{eg} and frequency ω_{eg} relate to the the difference in energy between the two atomic levels: $E_{eg} = \hbar\omega_{eg} = \hbar\omega_e - \hbar\omega_g$. For an atom in an electromagnetic field the total Hamiltonian of the system is of the form

$$\hat{H} = \hat{H}_\mathrm{a} + \hat{H}_\mathrm{f} + \hat{H}_\mathrm{int} \,, \tag{2.2.4}$$

where $\hat{H}_\mathrm{a}$, $\hat{H}_\mathrm{f}$ and $\hat{H}_\mathrm{int}$ are the atomic, field and interaction Hamiltonians respectively.

For a monochromatic field of frequency ω oscillating along a single mode the field Hamiltonian is [40]

$$\hat{H}_\mathrm{f} = \hbar\omega \hat{a}^\dagger \hat{a} \,. \tag{2.2.5}$$

Here we have used the annihilation and creation operators $\hat{a}$ and $\hat{a}^\dagger$ together in the form of the number operator $n = \hat{a}^\dagger \hat{a}$, which represents the number of photons in the system.

We will also define the relevant atomic operators based on the Pauli spin matrices:

$$\hat{\sigma}_x = |e\rangle\langle g| + |g\rangle\langle e| = \begin{bmatrix} 0 & 1 \\ 1 & 0 \end{bmatrix} \tag{2.2.6}$$

$$\hat{\sigma}_y = -i(|e\rangle\langle g| - |g\rangle\langle e|) = \begin{bmatrix} 0 & -i \\ i & 0 \end{bmatrix} \tag{2.2.7}$$

$$\hat{\sigma}_+ = \frac{1}{2}(\hat{\sigma}_x + i\hat{\sigma}_y) = |e\rangle\langle g| = \begin{bmatrix} 0 & 1 \\ 0 & 0 \end{bmatrix} \tag{2.2.8}$$

$$\hat{\sigma}_- = \frac{1}{2}(\hat{\sigma}_x - i\hat{\sigma}_y) = |g\rangle\langle e| = \begin{bmatrix} 0 & 0 \\ 1 & 0 \end{bmatrix} \tag{2.2.9}$$

$$\hat{\sigma}_z = |e\rangle\langle e| - |g\rangle\langle g| = \begin{bmatrix} 1 & 0 \\ 0 & -1 \end{bmatrix}. \tag{2.2.10}$$

The operators $\hat{\sigma}_\pm$ are known as the raising and lowering operators, representing the operation of going from the ground to excited state and vice versa.

The atomic Hamiltonian describes the energy levels of the system. In the two level case, the atomic Hamiltonian takes the form [40]

$$\hat{H}_\mathrm{a} = \frac{1}{2}\hbar\omega_{eg}\,|e\rangle\langle e| - \frac{1}{2}\hbar\omega_{eg}\,|g\rangle\langle g| = \frac{1}{2}\hbar\omega_{eg}\sigma_z\,, \tag{2.2.11}$$

where the energy of states $|e\rangle$ and $|g\rangle$ are given as $E_{e,g} = \pm\frac{1}{2}\hbar\omega_{eg}$.

For the interaction Hamiltonian we must consider how the transition dipole reacts to an external electric field. The resonant wavelength for most atomic systems is much larger than the size of the atom, such that we can treat the field as effectively constant over the atomic system in what is known as the dipole approximation. The transition dipole is then defined as $\hat{\mathbf{d}} = e\hat{\mathbf{r}}$. Here e is the elementary charge and $\hat{\mathbf{r}}$ is the radial position operator. We can write the interaction Hamiltonian as the dot product of the dipole operator with the electric field

$$\hat{H}_\mathrm{int} = -\hat{\mathbf{d}}\cdot\hat{\mathbf{E}} = \hbar g(\hat{\sigma}_- + \hat{\sigma}_+)(\hat{a} + \hat{a}^\dagger)\,, \tag{2.2.12}$$

where the resonant atom-field coupling is represented by the vacuum Rabi frequency $g = \sqrt{\frac{\omega_{eg}}{2\hbar\epsilon_0 V}}(\mathbf{e}\cdot\mathbf{d}_{eg})$ for a volume V, transition frequency ω_0, vacuum permittivity ϵ_0, and field polarization $\mathbf{e}$.

2.2.3 The Interaction Picture

In order to simplify the system for the dynamics of interest, we will move our system into the interaction picture and make the rotating wave approximation [40]. For the interaction picture, we consider the free evolution operator for total subsystem energy

$\hat{H}_0 = \hat{H}_\mathrm{a} + \hat{H}_\mathrm{f}$ as

$$\hat{U} = e^{i\hat{H}_0 t/\hbar}\,. \tag{2.2.13}$$

We transform the interaction Hamiltonian using $\hat{H}_0$, which will give us the full Hamiltonian for state evolution. The atomic and field operators commute, allowing them to be treated separately in our Hamiltonian [40]

$$\hat{\tilde{H}} = \hat{U}^\dagger \hat{H}_\mathrm{int} \hat{U} = \hbar g(e^{i\omega_{eg}t}\hat{\sigma}_+ + e^{-i\omega_{eg}t}\hat{\sigma}_-) \otimes (e^{-i\omega t}\hat{a} + e^{i\omega t}\hat{a}^\dagger) \tag{2.2.14}$$

$$\begin{aligned} &= \hbar g(\hat{a}^\dagger \hat{\sigma}_- e^{i(\omega-\omega_{eg})t} + \hat{\sigma}_+ a e^{-i(\omega-\omega_{eg})t} \\ &\quad + \hat{a}^\dagger \hat{\sigma}_+ e^{i(\omega+\omega_{eg})t} + \hat{\sigma}_- a e^{-i(\omega+\omega_{eg})t})\,. \end{aligned} \tag{2.2.15}$$

The first two terms involve near-resonant transitions, where $\Delta = \omega - \omega_{eg} \ll \omega_{eg}$. The first of these operators, $\hat{a}^\dagger\hat{\sigma}_-$, represents the creation of a photon while the atom transitions from its excited state to its ground state. The second operator, $\hat{a}\hat{\sigma}_+$, represents the inverse process where a photon is absorbed and the atom is driven from its ground state to excited state. By the rotating wave approximation, the other two high frequency terms are neglected since they average away on our timescales of interest. From this we get a simplified Hamiltonian

$$\hat{\tilde{H}} = \hbar g\left(\hat{a}^\dagger \hat{\sigma}_- e^{i\Delta t} + \hat{\sigma}_+ \hat{a} e^{-i\Delta t}\right)\,. \tag{2.2.16}$$

By transforming back into the Schrödinger picture, we get back a simplified interaction Hamiltonian

$$\hat{H}_\mathrm{int} = \hbar g\left(\hat{\sigma}_+ \hat{a} + \hat{a}^\dagger \hat{\sigma}_-\right)\,, \tag{2.2.17}$$

and combining the interaction Hamiltonian with the atomic and field components gives us our final Hamiltonian

$$\hat{H} = \frac{1}{2}\hbar\omega_{eg}\hat{\sigma}_z + \hbar\omega\hat{a}^\dagger\hat{a} + \hbar g\left(\hat{\sigma}_+\hat{a} + \hat{a}^\dagger\hat{\sigma}_-\right)\,. \tag{2.2.18}$$

This description of an atomic dipole in a monochromatic single-mode field is known as the Jaynes-Cummings (JC) Hamiltonian (for more details see [40]).

2.2.4 Semi-Classical Approximation

In order to relate the atom-field coupling to the scenario of a strong laser beam, we can ignore how this interaction affects the field and treat the field as a plane wave rather than a quantized field. This gives us our electric field

$$\mathbf{E} = 2\mathbf{e}|E_0|\cos(\omega t - \phi) = \mathbf{e}\left(E_0 e^{-i\omega t} + E_0^* e^{i\omega t}\right)\,, \tag{2.2.19}$$

where the phase term ϕ has been included. We can then use this equation to rewrite our interaction picture Hamiltonian from equation 2.2.16, by plugging the classical field into

equation 2.2.12

$$\hat{\tilde{H}} = -\hbar \left[\frac{(\mathbf{d}_{eg} \cdot \mathbf{e})|E_0|}{\hbar} e^{-i\Delta t} \hat{\sigma}_+ + \frac{(\mathbf{d}_{eg} \cdot \mathbf{e}^*)|E_0|}{\hbar} e^{i\Delta t} \hat{\sigma}_- \right] . \tag{2.2.20}$$

To simplify our notation, we can rewrite this using the the cycling rate of population moving between the two levels, which is known as the Rabi frequency (Ω). The Rabi frequency takes the form

$$\Omega = (\mathbf{d}_{eg} \cdot \mathbf{e})|E_0|/\hbar \, . \tag{2.2.21}$$

Plugging this into the new interaction picture Hamiltonian, we get

$$\hat{\tilde{H}} = -\hbar \left[\Omega e^{-i\Delta t} \hat{\sigma}_+ + \Omega^* e^{i\Delta t} \hat{\sigma}_- \right] . \tag{2.2.22}$$

Now all that remains is to transform back into the Schrödinger picture. Because we are now using a different field definition, we have to redefine our free evolution operator. Our Hamiltonian should rotate based on the optical field frequency ω, giving us our free evolution operator and transformation

$$\hat{U} = e^{i\omega \hat{\sigma}_{ee} t} \tag{2.2.23}$$

$$\hat{H}' = -i\hbar \hat{U}^\dagger \frac{\mathrm{d}\hat{U}}{\mathrm{d}t} + \hat{U}^\dagger \hat{H} \hat{U} \, . \tag{2.2.24}$$

Plugging in the Hamiltonian in equation 2.2.22 we get our final two level Hamiltonian, $\hat{H}'$,

$$\hat{H}' = -\hbar \Delta \hat{\sigma}_{ee} - \hbar(\Omega \hat{\sigma}_+ + \Omega^* \hat{\sigma}_-) \, . \tag{2.2.25}$$

with the operator $\sigma_{ee} = |e\rangle \langle e|$ in the first term that describes the detuning of the classical field from the transition energy. For a two level system, this is the final state of the Hamiltonian we will use to model our system. However, there are irreversible, incoherent effects that we have yet to take into account.

Our T-centre simulations make use of the master equation [40]

$$\frac{\partial}{\partial t} \hat{\rho} = -\frac{i}{\hbar} [\hat{H}, \hat{\rho}] + \hat{\mathcal{L}}(\hat{\rho}) \, . \tag{2.2.26}$$

The master equation is equivalent to the Schrödinger equation except for the Liouvillian superoperator $\hat{\mathcal{L}}(\hat{\rho})$ that will contain relaxation and decoherence terms. This superoperator takes the Lindblad form:

$$\hat{\mathcal{L}} = \sum_i \hat{C}_i \hat{\rho} \hat{C}_i^\dagger - \frac{1}{2} (\hat{C}_i^\dagger \hat{C}_i \hat{\rho} - \hat{\rho} \hat{C}_i^\dagger \hat{C}_i) \, . \tag{2.2.27}$$

The operators in the Liouvillian, $\hat{C}_i$, are known as the collapse operators. This addition makes the total Hamiltonian non-Hermitian.

2.2.5 Spontaneous Emission and Decoherence

We shall first consider relaxation from the excited state down to the ground state. We incorporate relaxation through the operator

$$\hat{C}_{eg} = \sqrt{\Gamma_{eg}}\hat{\sigma}_{-}\,. \tag{2.2.28}$$

The term Γ_{eg} is the relaxation rate, which is related to its reciprocal, the lifetime $T_1 = 1/\Gamma_{eg}$.

In addition to relaxation, the system may lose coherence through dephasing processes, such as phase fluctuations in the resonant field. The total rate of coherence loss is given by [40]

$$\gamma_{eg} = \frac{1}{2}\Gamma_{eg} + \gamma_{ee}\,, \tag{2.2.29}$$

where γ_{ee} represents additional dephasing processes unrelated to the relaxation, such as phase fluctuations of the field. The dephasing rate corresponds to the dephasing time $T_2 = 1/\gamma_{eg}$. In the limit that $\gamma_{ee} \ll \Gamma_{eg}$, Eq 2.2.29 becomes $\gamma_{eg} \approx \frac{1}{2}\Gamma_{eg}$, which is referred to as the lifetime limit. To incorporate the additional dephasing into the master equation we use [61]

$$\hat{C}_{ee} = \sqrt{\frac{\gamma_{ee}}{2}}\hat{\sigma}_z\,. \tag{2.2.30}$$

The steady-state excited state population of this two-level system in the presence of an optical field, found by taking the limit as $t \to \infty$, is [61]

$$\rho_{ee}(\infty) \propto \frac{1}{\Delta^2 + \gamma_{eg}^2 + \frac{\gamma_{eg}|\Omega|^2}{\Gamma_{eg}}}\,. \tag{2.2.31}$$

This is Lorentzian with respect to Δ, where the full-width half-max (FWHM)

$$\Delta\omega_{\text{FWHM}} = 2\gamma_{eg}\sqrt{1 + \Omega^2/(\gamma_{eg}\Gamma_{eg})}\,, \tag{2.2.32}$$

represents the instantaneous homogeneous linewidth. In the lifetime limit our spectral linewidth is

$$\Delta\omega_{\text{FWHM}} = \Gamma_{eg}\sqrt{1 + 2\Omega^2/\Gamma_{eg}^2}\,. \tag{2.2.33}$$

This demonstrates the power broadening effect from the resonant laser field. At sufficiently high laser power ($\Omega \gg \Gamma$), $\Delta\omega_{\text{FWHM}} \propto \Omega$. However, when $\Omega \ll \Gamma$, this reduces to the lifetime-limited linewidth $\Delta\omega_{\text{FWHM}} \approx \Gamma$.

Ω is determined by the laser intensity and the relaxation rate. To do so we rewrite the dipole moment in terms of Γ [61]

$$\mathbf{d}_{eg} = \sqrt{\frac{3\pi\epsilon_0\epsilon_R\hbar\eta_{\mathrm{R}}\eta_{\mathrm{ZPL}}\Gamma_{eg}c^3}{n^3\omega_0^3}}\,, \tag{2.2.34}$$

where ϵ_R is the relative permittivity, η_{R} is the radiative efficiency, η_{ZPL} is the ZPL fraction, and n is the index of refraction. If we assume that our optical field polarization matches the dipole, we plug our dipole into Eq. 2.2.21

$$\Omega = \sqrt{\frac{3\pi\epsilon_0\epsilon_R\hbar\eta_{\mathrm{R}}\eta_{\mathrm{ZPL}}\Gamma_{eg}c^3}{n^3\omega_0^3}}\frac{E_0}{\hbar}\,. \tag{2.2.35}$$

E_0 is related to the optical intensity I by

$$E_0 = \sqrt{\frac{2I}{\epsilon_0\epsilon_R c}}\,. \tag{2.2.36}$$

With this substitution, the Rabi frequency in terms of laser intensity is

$$\Omega = \sqrt{\frac{6\pi\eta_{\mathrm{R}}\eta_{\mathrm{ZPL}}\Gamma c^2 I}{\hbar n^2\omega_0^3}}\,. \tag{2.2.37}$$

With this two-level system we have a basic representation of the optical transition that defines the T-centre ZPL. Population is driven coherently between the ground and excited states at the rate Ω. This driving is impacted by the relaxation and decoherence rates Γ_{eg} and γ_{eg} as well as the detuning from the resonance Δ. However, this two-level system fails to capture the spin dynamics of the T-centre ground state.

2.2.6 Three-Level Dynamics

In order to incorporate a spin qubit into this model, we now include an additional energy level. The new level $|s\rangle$ is referred to as the metastable state. There are three possible configurations, which we label Ξ, V, and Λ based on their energy level diagrams (See Figure 2.2). The Λ-system will be most relevant to optical control of the T-center (See §2.1 and §3 for more details).

For a Λ-system, there exists $|g\rangle \rightarrow |e\rangle$ and $|s\rangle \rightarrow |e\rangle$ transitions. Both of these transitions can be driven, which may lead to a two-photon transition between $|g\rangle$ and $|s\rangle$ referred to as a Raman transition. We derive the conditions for a Raman transition in §2.4.

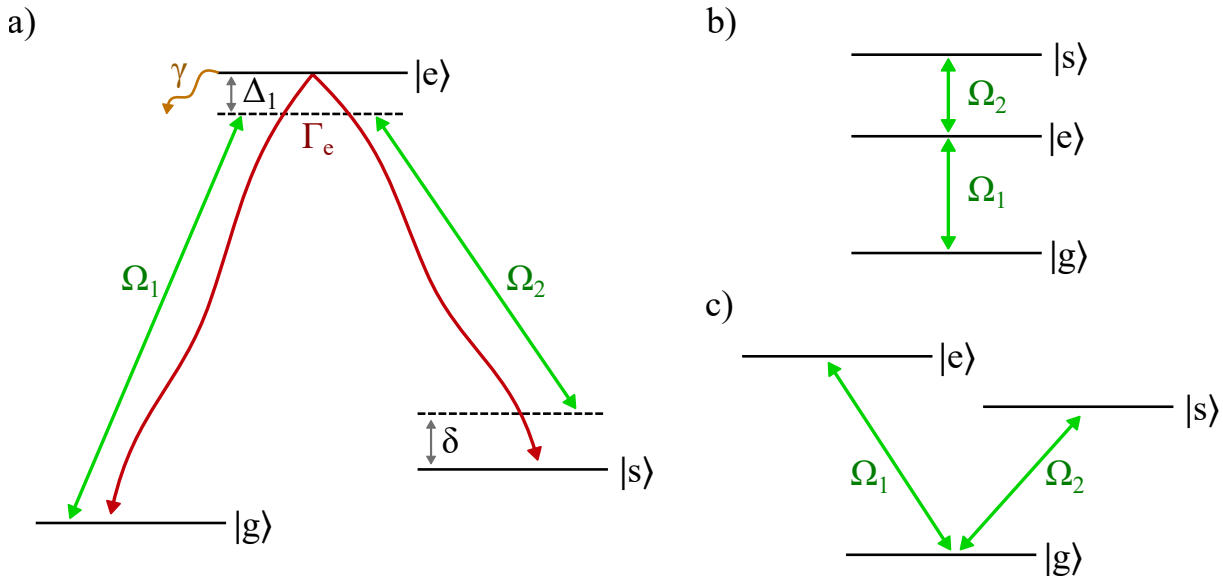

Figure 2.2: Three different configurations for a three-level system with two transitions: a) Λ, b) ladder (Ξ), and c) V.

We expand our Hamiltonian to include the metastable state. We define $\hat{\sigma}_{ij} = |i\rangle\langle j|$ and get our atomic and interaction Hamiltonian components [40],

$$\hat{H}_{\mathrm{a}} = \hbar\omega_g\hat{\sigma}_{gg} + \hbar\omega_e\hat{\sigma}_{ee} + \hbar\omega_s\hat{\sigma}_{ss} \tag{2.2.38}$$

$$\hat{H}_{\mathrm{int}} = \hat{\mathbf{d}}\cdot\hat{\mathbf{E}} = \hat{\mathbf{d}}_{ge}\cdot\hat{\mathbf{E}}_1 + \hat{\mathbf{d}}_{se}\cdot\hat{\mathbf{E}}_2\,, \tag{2.2.39}$$

where $\hat{\mathbf{E}}_{1,2}$ represent the fields for each transition.

We make the rotating wave approximation in the interaction picture once again with the unitary operator in Eq. 2.2.23, giving

$$\hat{H} = -\hbar\left(\Delta_1\hat{\sigma}_{ee} + \delta\hat{\sigma}_{ss}\right) - \hbar\left(\Omega_1\hat{\sigma}_{eg} + \Omega_2\hat{\sigma}_{es} + \Omega_1^*\hat{\sigma}_{ge} + \Omega_2^*\hat{\sigma}_{se}\right)\,. \tag{2.2.40}$$

The subscripts on Δ and Ω have been used to distinguish the properties relating to transitions 1 and 2 ($|g\rangle \to |e\rangle$ and $|s\rangle \to |e\rangle$ respectively). The term δ attached to the $\hat{\sigma}_{ss}$ operator is the two-photon detuning from $|g\rangle$ to $|s\rangle$, $\delta = \Delta_1 - \Delta_2$ (see Fig. 2.2).

Again there will be relaxation from the excited state, but now there are two paths of decay. For relaxation from the excited state to the ground and metastable state we define two collapse operators:

$$\hat{C}_{eg} = \sqrt{\Gamma_{eg}}\hat{\sigma}_{eg} \tag{2.2.41}$$

$$\hat{C}_{es} = \sqrt{\Gamma_{es}}\hat{\sigma}_{es}\,. \tag{2.2.42}$$

For our dephasing, we can again define two terms relating to each transition: $\hat{C}_{gg} = \sqrt{\gamma_{gg}}\hat{\sigma}_{gg}$ and $\hat{C}_{ss} = \sqrt{\gamma_{ss}}\hat{\sigma}_{ss}$. However, in the case that $\gamma_{gg} \approx \gamma_{ss}$, we can simplify our dephasing by attaching it to the excited state in one term

$$\hat{C}_{ee} = \sqrt{\gamma_{ee}}\hat{\sigma}_{ee}\,. \tag{2.2.43}$$

Only certain instances of the Λ-system have analytical solutions. In the remaining cases, numerical solutions become necessary. The simulations in this thesis use numerical integration with the Quantum Toolbox in Python (QuTiP) [30] and analytical solutions calculated in Mathematica [67].

2.3 Hyperfine Structure

A complete understanding of the ground state structure is required for general optical control. In this thesis we measure the (previously unknown) hyperfine ground state structure. In this section we introduce the theory of spin interactions in the T-centre ground state that governs this structure.

The T-centre hyperfine structure is due to the spin-spin interaction between the electron and hydrogen nucleus. The electron is known to be a spin-1/2 particle ($S = 1/2$), which can be in the spin up ($m_S = +1/2$) or spin down ($m_S = -1/2$) configuration. The electron has a magnetic moment $\mu = -g_S\mu_B\mathbf{S}$ where the spin g-factor is $g_S \approx 2$ and μ_B is the Bohr magneton [23].

The nucleus of the hydrogen atom has a magnetic moment $\boldsymbol{\mu}_I$ due to the nuclear spin $\mathbf{I}$ given by the equation [23]

$$\boldsymbol{\mu}_I = g_I\mu_N\mathbf{I}\,. \tag{2.3.1}$$

The term μ_N is simply the Bohr magneton μ_B scaled by the ratio of the electron mass to the proton mass such that we get $\mu_N = (m_e/M_P)\mu_B \approx \mu_B/1836$. Since $\mathbf{I} = 1/2$ for the hydrogen nucleus in the T-centre, this magnetic moment will interact with the magnetic field produced by the electron spin [23].

The hyperfine interaction Hamiltonian is [23]

$$H_{\mathrm{HF}} = -\boldsymbol{\mu}_I \cdot \mathbf{B}_{\mathrm{e}}\,, \tag{2.3.2}$$

where $\mathbf{B}_{\mathrm{e}}$ is the magnetic field produced by the electron [23]. Because $\mathbf{B}_{\mathrm{e}} \propto \mathbf{S}$, we can rewrite the hyperfine Hamiltonian to better reflect the spin-spin interaction at play as

$$H_{\mathrm{HF}} = \mathbf{IAS} = \sum_{i,j} A_{ij} I_i \otimes S_j\,, \tag{2.3.3}$$

where **A** is our hyperfine tensor. The hyperfine axis is defined as the axis where the tensor is diagonalized:

$$\mathbf{A} = \begin{bmatrix} A_x & 0 & 0 \\ 0 & A_y & 0 \\ 0 & 0 & A_z \end{bmatrix}. \tag{2.3.4}$$

For a nuclear spin (considered to be localized at a point) coupled to an electron bound to the same nucleus in a spherically symmetric s orbital the hyperfine interaction is the isotropic Fermi contact hyperfine [58]

$$H_{\mathrm{HF}} = A\mathbf{I}\cdot\mathbf{S}\,. \tag{2.3.5}$$

in which the hyperfine tensor **A** reduces to the constant A.

The eigenenergies of the isotropic hyperfine Hamiltonian are [23]

$$E_{\mathrm{HF}} = A\langle\mathbf{I}\cdot\mathbf{S}\rangle = \frac{A}{2}[F(F+1) - I(I+1) - S(S+1)]\,, \tag{2.3.6}$$

where $F = I + S$. Since $S = 1/2$ and $I = 1/2$, there will be two values for the total angular momentum, $F = 0, 1$, which give the energies $E_1 = A/4$ and $E_0 = -3A/4$. The splitting between these levels will be $\Delta E_{\mathrm{HF}} = A$.

We will extend this simple case to introduce the Zeeman effect in §2.3.1. However, when the electron spin and nuclear spin are displaced, as they are in the T-centre, or when the electron has orbital angular momentum (is not s-type) then the dipole-dipole interaction is anisotropic. In Chapter 6 we determine the anisotropic hyperfine tensor of the T-centre through optically-detected magnetic resonance experiments.

2.3.1 The Zeeman Effect

This spin-spin interaction combines with the Zeeman effect when a magnetic field is applied. We determine the magnetic field behavior of the hyperfine interaction in this work in order to characterize the hyperfine interaction.

The magnetic moment combines both the electron and nuclear magnetic moments

$$\boldsymbol{\mu}_{\mathrm{a}} = -g_S\mu_B\mathbf{S} + g_I\mu_N\mathbf{I} \approx -g_S\mu_B\mathbf{S}\,; \tag{2.3.7}$$

however, the nuclear component gets dominated by the electronic moment since $\mu_N \ll \mu_B$. Therefore, we shall ignore the nuclear magnetic moment in the low fields used in this work. Our Zeeman Hamiltonian for an atom in an external magnetic field takes the form

$$H_{\mathrm{Ze}} = g_S\mu_B\mathbf{S}\cdot\mathbf{B}\,. \tag{2.3.8}$$

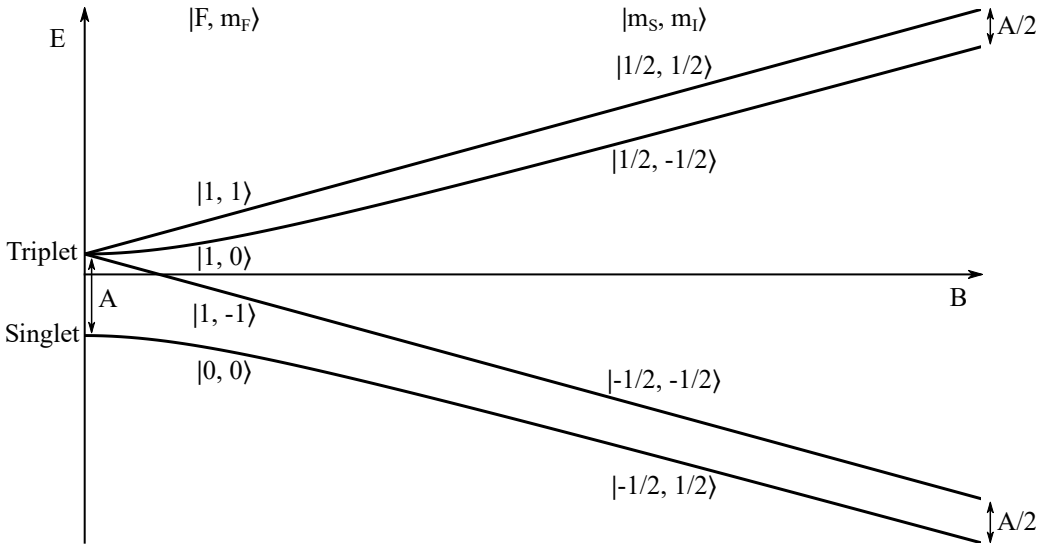

Figure 2.3: The hyperfine structure of a hydrogen-like atom is isotropic and completely determined by the Fermi contact interaction. Displacing the electron and nuclear spins (as in the T-centre) introduces anisotropic components and breaks the symmetry in the triplet states, see §6.2.

Together with the hyperfine Hamiltonian, we get the hyperfine-Zeeman Hamiltonian

$$H_{\mathrm{HZ}} = g_S \mu_B \mathbf{S} \cdot \mathbf{B} + \mathbf{IAS}\,. \tag{2.3.9}$$

When calculating the eigenenergies of this Hamiltonian, the eigenstates will transition between the weak-field eigenstates $|F, m_F\rangle$ and the high-field eigenstates $|m_S, m_I\rangle$ as the magnetic field increases [23]. Figure 2.3 shows the eigenenergies of H_{HZ} as a function of magnetic field in the isotropic case of the Fermi contact hyperfine. At zero-field we recover $\Delta E_{\mathrm{HF}} = A$, while in the intermediate-field, where the nuclear Zeeman splitting can still be ignored, each of the m_S levels is split into two sublevels for m_I with a hyperfine splitting equal to $A/2$. The exact solutions for E_{HZ} in terms of B are [23, 61]

	$\lvert F, m_F\rangle$	$\lvert m_S, m_I\rangle$	E_{HZ}
Triplet	$\lvert 1, 1\rangle$	$\lvert 1/2, 1/2\rangle$	$\frac{A}{4} + \mu_B B$
	$\lvert 1, 0\rangle$	$\lvert 1/2, -1/2\rangle$	$-\frac{A}{4} + \frac{1}{2}\sqrt{A^2 + (2\mu_B B)^2}$
	$\lvert 1, -1\rangle$	$\lvert -1/2, -1/2\rangle$	$\frac{A}{4} - \mu_B B$
Singlet	$\lvert 0, 0\rangle$	$\lvert -1/2, 1/2\rangle$	$-\frac{A}{4} - \frac{1}{2}\sqrt{A^2 + (2\mu_B B)^2}$

For the general, anisotropic hyperfine structure, the eigenenergies at field will depend on the direction of the magnetic field. In the intermediate-field range, the hyperfine splittings $A/2$ vary with field direction, which results in an effective hyperfine value A_{eff} for a given field direction. Additionally, the anisotropy from the electron and nuclear spin

displacement can break the degeneracy of the triplet states at zero field. Finally, in the isotropic case, the $|F, m_F\rangle = |1, \pm 1\rangle$ wavefunctions did not mix in the transition between the two field limits, though in the anisotropic case all states could mix.

Determining the different A_i components of an anisotropic hyperfine tensor, as well as the tensor rotation, requires measuring the energy level splittings as a magnetic field is applied in different directions. The optically-detected magnetic resonance experiment in Chapter 6 varies the magnetic field direction and magnitude in order to identify the ground state structure.

2.4 All-Optical Control

Boiling down the level structure of the T-centre to a three-level Λ-system as in §2.2.6, we see that there are already many different ways to approach optical control compared to direct spin transitions. For the T-center, the Λ-system we focus on comprises two electron spin states in the ground state, with the common excited state being one of the hole spin states.

Ideally, the chosen method of optical control will have high speed and high fidelity when producing arbitrary spin rotations. As we shall see from the following sections, there is typically a trade-off between the gate speed and fidelity.

2.4.1 Coherent Population Trapping

Coherent population trapping (CPT) is a method of arbitrary qubit state preparation. In Chapter 7 we report the first instance of optical CPT of the T-centre.

The Λ-system we established in §2.2.6 has Hamiltonian and collapse operators:

$$\begin{aligned} \hat{H} =& -\hbar \left(\Delta_1 \hat{\sigma}_{ee} + \delta \hat{\sigma}_{ss}\right) \\ & -\hbar \left(\Omega_1 \hat{\sigma}_{eg} + \Omega_2 \hat{\sigma}_{es} + \Omega_1^* \hat{\sigma}_{ge} + \Omega_2^* \hat{\sigma}_{se}\right) \end{aligned} \tag{2.4.1}$$

$$\hat{C}_{eg} = \sqrt{\Gamma_{eg}}\hat{\sigma}_{eg} \tag{2.4.2}$$

$$\hat{C}_{es} = \sqrt{\Gamma_{es}}\hat{\sigma}_{es} \tag{2.4.3}$$

$$\hat{C}_{ee} = \sqrt{\gamma_{ee}}\hat{\sigma}_{ee}\,. \tag{2.4.4}$$

If we consider the case where the two-photon detuning δ is much smaller than either single-photon detuning ($|\delta| \ll |\Delta_{1,2}|$), we can find an analytical solution.

For CPT we focus on small single-photon detunings, where we have the relation $\Delta_{1,2} = \Delta \lesssim \Omega_{1,2}$,. We also assume here that there is a fixed phase relation between Ω_1 and Ω_2, which is to say the fields are coherent. In our $\{|g\rangle, |e\rangle, |s\rangle\}$ basis, we can simplify our

Hamiltonian [40]

$$\hat{H} = -\hbar \begin{bmatrix} 0 & \Omega_1 & 0 \\ \Omega_1 & \Delta & \Omega_2 \\ 0 & \Omega_2 & 0 \end{bmatrix} . \tag{2.4.5}$$

This Hamiltonian has eigenvalues and corresponding eigenvectors:

$$\lambda_0 = 0,\ \lambda_\pm = -\Delta/2 \pm \sqrt{\Omega_1^2 + \Omega_2^2 + (\Delta/2)^2} \tag{2.4.6}$$

$$|D\rangle = \frac{1}{\sqrt{\Omega_1^2 + \Omega_2^2}} [\Omega_2 |g\rangle - \Omega_1 |s\rangle] \tag{2.4.7}$$

$$|B_\pm\rangle = \frac{1}{\sqrt{\Omega_1^2 + \Omega_2^2 + \lambda_\pm^2}} [\Omega_1 |g\rangle - \lambda_\pm |e\rangle + \Omega_2 |s\rangle] . \tag{2.4.8}$$

The eigenstates $\{|D\rangle, |B_\pm\rangle\}$ are denoted as the dark and bright states. The dark state does not incorporate the excited state, whereas the bright states do.

Assuming negligible spin relaxation or decoherence, $|D\rangle$ is the stationary state of the system. The dark state can be rewritten in the form

$$|D\rangle = \cos\Theta |g\rangle - \sin\Theta |s\rangle , \tag{2.4.9}$$

where $\tan\Theta = \Omega_1/\Omega_2$ and Θ is known as the mixing angle. Through coherent driving of the two transitions that maintains the two-photon resonance from the ground state to metastable state, any population not already in $|D\rangle$ will rapidly decay into $|D\rangle$, where it remains. This phenomenon is known as coherent population trapping (CPT).

CPT is an effect that is in the steady-state solution of the Λ-system, providing coherent state preparation. By adiabatically varying the fields in time, CPT can be used to transfer population between any two states. The following sections consider what happens when the two optical fields are varied in time.

2.4.2 Stimulated Raman Adiabatic Passage

The first time-dependent situation we shall consider involves adiabatic time dependence for our Λ-system, with the adiabatic criteria $\left|\dot{\Theta}\right| \ll |\lambda_\pm - \lambda_0|$, where $\lambda_{0,\pm}$ are the eigenvalues from Eq. 2.4.6. Rewriting the mixing angle Θ in terms of Ω we get [40]

$$\left| \frac{\dot{\Omega}_1 \Omega_2 - \Omega_1 \dot{\Omega}_2}{\Omega_1^2 + \Omega_2^2} \right| \ll |\lambda_\pm - \lambda_0| . \tag{2.4.10}$$

The process of Stimulated Raman Adiabatic Passage (StiRAP) [11] makes use of two equal Gaussian pulses separated by the FWHM in time (see Fig. 2.4a). The first pulse coresponds to the second transition $|s\rangle \leftrightarrow |e\rangle$, while the second corresponds to the first

transition $|g\rangle \leftrightarrow |e\rangle$. This may seem counterintuitive, since the first pulse addresses two unoccupied states given our initial condition $|\psi(t_0)\rangle = 0$, but flipping the order of pulses will cause the ground state population to be driven into the upper excited state, moving the system out of the dark state and into the bright states.

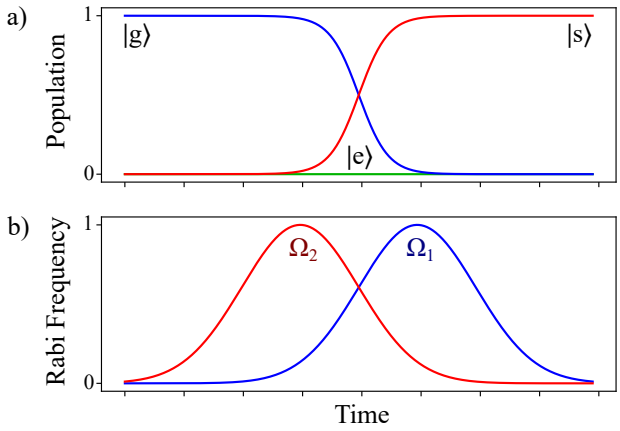

Figure 2.4: The stimulated Raman adiabatic passage pulse scheme. a) Population response in time to the applied fields in StiRAP. Population initialized in the ground state is transferred to the metastable state without any population passing through the excited state. b) Optical field drive strength in terms of Rabi frequency as a function of time during StiRAP.

This method produces a coherent transfer of population from one spin state to another. However, StiRAP has limited applicability. Due to the adiabaticity requirement, StiRAP is a relatively slow process when compared to time scale of the peak Rabi frequency for the pulses. In addition, we must consider how StiRAP moves about the spin population. StiRAP requires starting with a known state, otherwise resonant excitation out of $|D\rangle$ will occur. Universal optical control requires applying a known rotation regardless of what state the system is in.

2.4.3 Far-Detuned Raman Scheme

In order to achieve a universal pulse scheme, we look to the far-detuned regime, where our single-photon detuning for each optical transition is large.

Once again, we maintain the condition that our two-photon detuning is small, $0 \approx |\Delta_1 - \Delta_2| \ll |\Delta_{1,2}|$, but now we require that $|\Delta_{1,2}| \gg \gamma_e, \Omega_{1,2}$. In this limit the excited state population vanishes. We shall define two relevant terms, the effective Rabi frequency and effective detuning for the two photon transition:

$$\Omega_{\text{eff}} \approx -\frac{\Omega_1 \Omega_2}{\Delta_1} \tag{2.4.11}$$

$$\delta_{\text{eff}} = \Delta_1 - \Delta_2 + \frac{|\Omega_1|^2 - |\Omega_2|^2}{\Delta_1}. \tag{2.4.12}$$

As long as the two optical fields have the same strength ($\Omega_1 = \Omega_2$), δ_{eff} reduces to the typical two-photon detuning: $\delta = \Delta_1 - \Delta_2$.

If we use the same initial condition as before ($|\psi(t_0)\rangle = |g\rangle$), it can be shown that the solutions for the state coefficients c_g and c_s are [40]

$$c_g(t) = e^{i\frac{\delta_{\text{eff}}}{2}t}\left[\cos(\bar{\Omega}_{\text{eff}}t) - i\frac{\delta_{\text{eff}}}{2\bar{\Omega}_{\text{eff}}}\sin(\bar{\Omega}_{\text{eff}}t)\right] \tag{2.4.13}$$

$$c_s(t) = ie^{i\frac{\delta_{\text{eff}}}{2}t}\frac{\Omega_{\text{eff}}}{\bar{\Omega}_{\text{eff}}}\sin(\bar{\Omega}_{\text{eff}}t)\,, \tag{2.4.14}$$

where we have defined $\bar{\Omega}_{\text{eff}} = \sqrt{\Omega_{\text{eff}}^2 + (\delta_{\text{eff}}/2)^2}$ as the detuned effective two-photon Rabi frequency. When δ_{eff} goes to 0

$$c_g(t) = \cos(\Omega_{\text{eff}}t) \tag{2.4.15}$$

$$c_s(t) = i\sin(\Omega_{\text{eff}}t)\,, \tag{2.4.16}$$

which gives

$$|\psi(t)\rangle = \cos(\Omega_{\text{eff}}t)\,|g\rangle + i\sin(\Omega_{\text{eff}}t). \tag{2.4.17}$$

This solution is the rotation of our spin qubit through the use of optical transitions, with the same form as directly addressing the qubit. By simultaneously turning the two optical fields on and off in square pulses we can produce pulses that coherently drive spin rotations with a Rabi frequency Ω_{eff} [6, 68, 55]. This means that, regardless of the initial state, the same amount of spin rotation can be driven by using the same square pulse length. One feature of far-detuned Raman pulses is the ability to change the axis of rotation on the Bloch sphere by changing the relative phase between Ω_1 and Ω_2. Pairing this with pulse timing allows for arbitrary single qubit gates. This process of driving far-detuned Raman pulses is sometimes referred to as driving stimulated Raman transitions [68, 55].

Since this Raman scheme requires $|\Delta_{1,2}| \gg \gamma_e, \Omega_{1,2}$, we will be limited in the effective Rabi frequency we can drive by $|\Omega_{\text{eff}}| \ll |\Omega_{1,2}|$. The main tradeoff with Raman control schemes is the limit to the rate of spin rotations for a given detuning.

2.5 All-Optical Control in Other Systems

A number of solid-state spin defects have been used to demonstrate all-optical control schemes. While not an exhaustive list, we shall take a look at some key examples of optical control from quantum dots, rare-earth ions (REI), and diamond colour centres.

2.5.1 All-Optical Control of Quantum Dots

Individual quantum dots have been engineered with improved optical transitions for the purposes of optical control. InGaAs quantum dots are one such example, where the Λ-system formed by the splitting of the ground state spin levels has been used to drive stimulated Raman transitions [55]. Since the excited state of this system also splits under field, they use a far-detuned 4ps pulse with circular polarization to ensure population never enters the excited state and the two Λ-systems constructively add towards the effective Rabi frequency of the spin rotation. Initialization and readout of the spin states was done by weakly driving a resonant optical transition from one of the spin states constantly with an initialization fidelity of 92%. Varying pulse intensity showed Rabi oscillations out to 13π, at which point the system began breaking the adiabatic limit where $\Delta \gg \Omega$. Using this spin control it was possible to perform a Ramsey measurement in which the Larmor frequency appropriately matched the spin state splitting, and the $T_2^\star$ was reduced due the constant optical pumping [55].

Following this work, it was shown that two vertically stacked quantum dots that were tunnel coupled due to proximity could be entangled and controlled purely through optical transitions [37]. The two dot state can be initialized into the singlet state $|\uparrow\downarrow\rangle - |\downarrow\uparrow\rangle$ through optical pumping on the triplet state. Single-qubit gates are accomplished by fast, broadband pulses that spectrally span the splitting between the ground state singlet and triplet states [37]. A π-pulse of this form transforms the singlet state $|\uparrow\downarrow\rangle - |\downarrow\uparrow\rangle$ to the mixed triplet state $|\uparrow\downarrow\rangle + |\downarrow\uparrow\rangle$.

More recent experiments that included photocurrent readout [50] and waveguide integration [22] produced similar or improved results. In the case of waveguide integration, different linear and circular polarizations were used for the far-detuned Raman pulses in order to drive spin rotations about all 3 axes of the Bloch sphere with 99% rotation fidelity [22].

2.5.2 All-Optical Control of Rare Earth Ions

REIs can possess extremely narrow optical transitions and long spin coherence times [1]. These qualities make REIs interesting platforms to demonstrate optical control of spin qubits. Nanophotonic cavities were designed for Nd^3+ ions within yttrium orthovanadate (YVO_4) crystals providing improved optical coupling that allowed for measurable Rabi oscillations in the optical qubit [72]. In addition, Ramsey interference fringes showed that this cavity integrated system had a linewidth near its lifetime limit. These first steps towards optical control help to characterize the optical properties of the spin-photon interface for their use in driving spin rotations.

Other REI work has focused on Eu^3+ ions within Y_2O_3 nanoparticles. This system put to use a similar method to the far-detuned Raman scheme mentioned in §2.4.3, though

notably obtained spin rotations with two-frequency square pulses that were not detuned from the single-photon resonances [59]. With these Raman pulses, spin control and characterization was demonstrated by all-optical spin echo and dynamical decoupling sequences, in which spin coherences of multiple milliseconds were found [59]. This instance of spin dynamical decoupling sequence represents one of the first to make use of an all-optical approach for spin control.

2.5.3 All-Optical Control of Diamond Colour Centres

Some diamond colour centres have demonstrated optical control, including the NV centre [68] and the SiV centre [6]. With the NV centre, CPT is both demonstrated and used as a method for spin initialization and readout [68]. The initialization of the spin state using CPT had an effective Rabi frequency of 50 MHz with a fidelity of 80%, being limited in each direction by either coupling to the excited state through fast driving or spin dephasing kicking in with slow driving [68]. In a similar way to Press et al. [55], the detuned Raman pulses were designed to constructively interfere the two Λ-systems when rotating the ground state spin [68]. Notably, only two axes of rotation are available to be driven in this system without changing the angle of excitation and π-rotations have a fidelity of only 69%, though this did allow for an all-optical Hahn-echo measurement of the homogeneous spin coherence.

Further study of optical control with the NV centre has explored the theoretical potential of different optical pulse schemes [18]. In particular, while StiRAP is slow, a pump-dump process by which spin evolution in the excited state leads to spin control could produce faster results with reasonable fidelities [18]. Rather than a Λ-structure, this process would make use of a V-system in which the ground state is degenerate with the spin rotation occurring naturally in the excited state. To remove the sensitivity to pulse shape generation, a pulse train of partially excited pulses could be used to periodically pump some population to the excited state where it can evolve to flip its spin with the advantage that minimal laser power is needed [18].

Aside from the NV centre, the SiV, GeV, and SnV centres have all garnered attention recently as alternatives within diamond. Recent work on the SiV centre has begun characterizing optical control in this system. Initial work focused on a Λ-system formed by split orbital states at zero magnetic field [7]. Resonant driving of the optical transitions showed optical Rabi oscillations up to 10π for a given transition with 95% fidelity for a π-rotation, allowing for a Ramsey interference measurement. Driving between the ground states through two-photon resonance was done using a far-detuned broadband Raman pulse with a 1 ps duration. The small 30% π-rotation fidelity was limited by optical pulse rise and fall tails overlapping.

In Ref. [6], Zeeman-split ground state rotations were carried out using 10 ns bichromatic square pulses. Rabi oscillations of the ground state spin between 1.5 MHz and

4.1 MHz were observed. A discrepancy between T_2 and $T_2^\star$ from Ramsey and spin echo measurements suggests that there is some unaccounted for source of dephasing.

Theoretical work has been done to compare the SiV centre and GeV centre as platforms to make use of StiRAP. At high field (9 T) it should be possible to achieve a population transfer rate of 10 GHz between the spin states of the SiV centre with a fidelity of 97% [24]. The GeV centre has improved transition resolution due to increased splitting for a given field strength and narrower linewidth, leading to a simulated process fidelity greater than 99.9%.

Finally, the SnV centre is the most recent diamond defect to be explored. Measurements on the optical qubit demonstrated a 1.7 ns π-rotation with 71% fidelity with multi-axis control [2].

2.5.4 Conclusion

Quantum dots, REIs, and diamond colour centres have all demonstrated optical control to different levels of success. Prior to this thesis it has been unclear what is required to achieve T-centre optical control. Some of the findings here reported demonstrations of optical Rabi oscillations and optical CPT, which we shall demonstrate in Chapters 5 & 7. Through careful characterization of the T-centre ground state structure and demonstrations of coherent optical driving, we can develop a process for all-optical control of T-centre spins.

Chapter 3

Optical Control Simulations

In order to best implement optical control, we first simulate the control schemes for the T-centre electron spin qubit. The following optical schemes aim to coherently control the spin through the use of optical transitions to the TX_0 state. These simulations provide insight into the potential for all-optical control protocols utilizing the T-centre. Specifically, we determine which parameter regimes of optical power, detunings, and temperatures are required to perform optical Rabi pulses, StiRAP, and Raman optical control of the electron spin qubit. We considered the best available T-centre ensembles in bulk ^{28}Si and single T-centres in SOI in order to determine whether to use the bulk spectroscopy apparatus in Bergeron et al. [10] or the confocal microscope for single centre characterization from Higginbottom et al. [27] in our optical control experiments.

On one hand, using single centres removes problems from inhomogeneity. In particular, environmental differences, such as the local magnetic field or laser intensity can lead to spectral features being lost or 'washed out' in ensemble measurements. However, single T-centres in SOI have not yet demonstrated homogeneous linewidths as narrow as the 0.69(1) MHz linewidth measured in bulk ^{28}Si [21].

T-centres in bulk ^{28}Si offer the narrowest linewidths observed and brighter signals than measured for any single T-centre to date. To eliminate inhomogeneities in laser intensity across the ensemble it will be important to illuminate the sample with a uniform beam that covers the entire surface of the sample. This means that the laser intensity for a given output power will be considerably lower than it could be for a single centre in the confocal microscope. It will be particularly hard to deal with inhomogeneities in laser intensity caused by reflections and scattering.

To compare the feasibility of optical control in these two apparatuses, we shall use the fidelity and discuss the necessary laser powers. For this work we shall set 99.9% as the fidelity threshold we wish to hit for optical control.

Measured Parameters		
Parameter	**Bulk ^{28}Si**	**^{nat}Si SOI Singles**
Spectral Diffusion	27 MHz [45]	400 MHz [27]
Γ	$\sim 2\pi \cdot 0.16$ MHz [10]	
γ	γ_T (See Eq 2.1.1) [10]	
γ_e	$\sim$500 Hz [10]	$\sim$500 Hz*
g_e	2.005 [10]	
η_{ZPL}	0.23 [10]	
Estimated/Chosen Parameters		
Temperature	1.5 K	4.2 K
Beam Radius	4 mm	1 µm
Magnetic field	110 mT	
g_h	1-3.5 (Chose 2.5)	
η_R	0.03-1	

Table 3.1: T-centre parameters used for simulation. *Assumed from bulk ^{28}Si measurement.

3.1 Parameters

Table 3.1 lists the parameters used in the following simulations and calculations performed in this chapter, except where otherwise noted. The measured parameters come from the known optical and spin properties for the T-centre as were previously given in Table 2.2. The term γ_e represents the electron spin dephasing, which is calculated from $\gamma_e = 1/T_{2,e}$. The remaining parameters consist of unknown T-centre characteristics and experimental parameters that were chosen based on the bulk spectroscopy and confocal microscopy apparatuses. The bulk sample in the apparatus used in Bergeron et al. [10] was cooled below 1.5 K through direct contact with liquid He. The apparatus used by Higginbottom et al. [27] utilized a closed-cycle cryostat with a base temperature of 2.7 K that cooled the T-centres down to a minimum temperature of 4.2 K. The bulk and single T-centres we compare in this chapter are under the conditions of these two apparatuses. We have chosen a 110 mT magnetic field, which is similar to the fields in the two apparatuses [10, 27], and matches the field in the setup we build in §4.5.1.

3.2 Rabi Frequency from Laser Power

We begin by estimating the relationship between the laser power, spot size, and the Rabi frequency for the T-centre in order to determine the optical powers needed. From

Equation 2.2.37,

$$\Omega = \sqrt{\frac{6\pi\eta_R\eta_{ZPL}\Gamma c^2 I}{\hbar n^2 \omega_0^3}}. \tag{3.2.1}$$

At field TX_0 splits, branching between the two transitions for each excited state and impacting Γ for each transition. The branching ratio changes with the magnetic field orientation and magnitude, but a rough estimate of the ratio from the B/C transitions to the A/D transitions (as defined in Fig. 2.1) for a single centre under a single magnetic field gave the value $r = 1.2$ [27]. We shall use this value as a 'typical' value, but the branching ratio could change significantly from this value, depending on magnetic field direction. We choose to focus on the stronger dipoles of B/C, attaching a factor of $r/(1+r) \approx 6/11$ to Γ in Equation 3.2.1.

Most of the parameters in Eq. 3.2.1 can be found in Table 3.1. For the index of refraction, we use the known value of 3.4 for silicon [42]. Bulk samples will be illuminated by a collimated beam, while single centres sit at the centre of the focal point of the confocal microscope from Higginbottom et al. [27]. The main difference in calculations for these systems are the radius of the excitation spot. The radiative efficiency, which is not precisely known, will be critical in determining the required power.

3.3 Two-Level System

We begin QuTiP simulations of the T-centre with a two-level system representing the TX_0 transition. This is a useful first step to check that the optical properties are behaving as expected and serves as a system to demonstrate the visibility of optical Rabi oscillations for different scenarios.

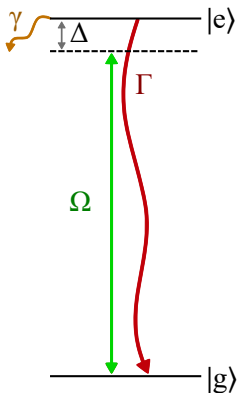

Figure 3.1: Diagram of the two-level system simulated in QuTiP. The ground and excited states are given by $|g\rangle$ and $|e\rangle$ respectively. Ω and Δ represent the optical field drive strength and detuning, while the relaxation and dephasing rates of the excited state are labelled Γ and γ.

QuTiP utilizes a master equation solver, which matches the density matrix formulation shown in §2.2. We use the same Hamiltonian and collapse operators derived for a two-level system

$$\hat{H} = -\hbar\Delta\hat{\sigma}_{ee} - \hbar(\Omega\hat{\sigma}_{+} + \Omega^{*}\hat{\sigma}_{-}), \tag{3.3.1}$$

$$\hat{C}_{eg} = \sqrt{\Gamma}\hat{\sigma}_{-}, \tag{3.3.2}$$

$$\hat{C}_{ee} = \sqrt{\gamma}\hat{\sigma}_{z}. \tag{3.3.3}$$

One feature missing from this model is spectral diffusion. We assume that spectral diffusion leads to frequency shifting in time about the centre of the transition frequency in a Gaussian distribution. To model this we solve the system dynamics for a number of detunings about the specified Δ, where each solution is weighted based on the Gaussian distribution that is given by the spectral diffusion. The FWHM of the Gaussian is equal to the measured value of spectral diffusion. We sample a discrete number of points that capture the Gaussian distribution rather than integrating over the whole function.

3.3.1 Optical Driving

Before diving into time dependent solutions, we check the steady state solution of the two-level system to confirm that it matches the observed properties of the T-centre with the parameters we have set. In Figure 3.2a, the T-centre spectrum is shown through sweeping the transition detuning about 0. The simulated long-term homogeneous linewidths are 29 MHz and 548 MHz for bulk and single centres respectively. The impact of temperature on linewidth is depicted in Figure 3.2b where the bulk ^{28}Si parameters have been used in order to properly illustrate the lower range of temperatures.

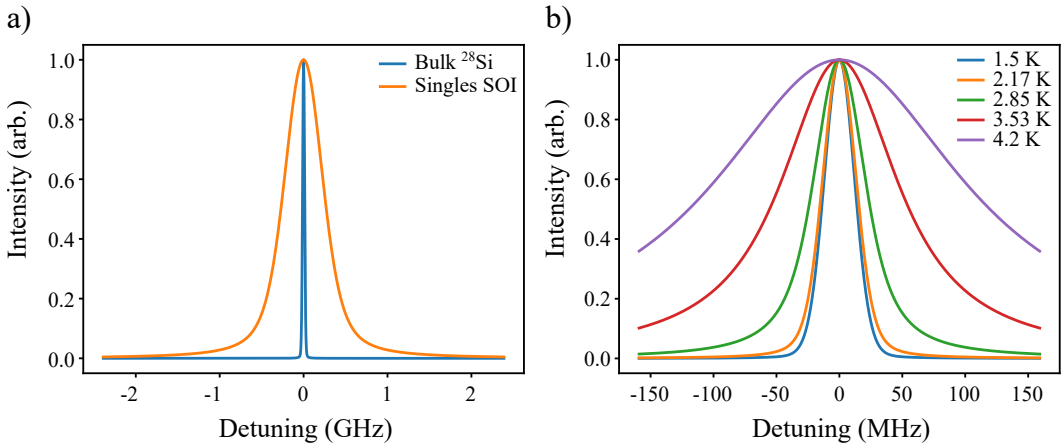

Figure 3.2: Simulated two-level spectra of the T-centre. a) Comparison of the bulk ^{28}Si and ^{nat}Si SOI singles lineshapes at 1.5 K and 4.2 K with respect to optical field detuning. b) Temperature dependence of the linewidth shown in the spectra of the bulk ^{28}Si two-level resonance.

Next, using the time dependent solution of the master equation, we can drive with a constant field defined by a given Rabi frequency and detuning. Figure 3.3 shows the excited state population versus the expected rotation angle for different powers. These give a quantitative idea of what Rabi frequency is needed to see any oscillations. For bulk

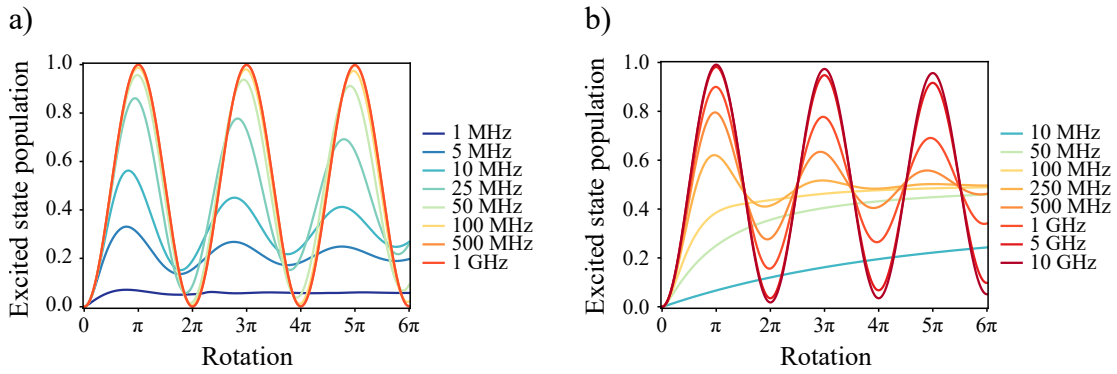

Figure 3.3: Simulated optical Rabi oscillations for a two-level system. a) Bulk ^{28}Si optical Rabi oscillations at different Rabi frequencies. b) Single ^{nat}Si SOI T-centre optical Rabi oscillations at different Rabi frequencies.

^{28}Si, visible oscillations can be seen starting near 1 MHz despite transferring very minimal population up to the excited state. Meanwhile, the single centres in SOI require more than 100 MHz in order to see oscillations. For reference, the temperature dephasing for these systems ($\gamma(T)$) is $2\pi \cdot 13$ kHz and $2\pi \cdot 37$ MHz for ensemble and single centre apparatuses respectively. The bulk linewidth is then limited by $\Gamma \approx 2\pi \cdot 0.16$ MHz), whereas the singles are limited by $\gamma(T)$. Visible oscillations therefore rely on driving a Rabi frequency near or above the instantaneous linewidth. In practice, the best instantaneous homogeneous linewidth in the bulk apparatus was still a factor of four greater than the lifetime limit [21]. Using Eq. 3.2.1 with a conservative estimate of $\eta_R = 0.03$, a laser power of 103 mW is needed to drive $\Omega = 5$ MHz in the bulk apparatus, while a laser power of 64 µW is needed to drive $\Omega = 500$ MHz in the single centre apparatus. These powers are both reasonable to achieve.

Finally, our last metric of the quality of optical Rabi oscillations is the π-pulse fidelity as a function of our system parameters. The figures report infidelity (100%-fid.). The π-pulse infidelity relative to the Rabi frequency and temperature is shown in Figure 3.4. Looking at Figure 3.4a, we see that the optical Rabi approaches unit fidelity as the Rabi frequency increases, which is to be expected. Due to the difference in dephasing and spectral diffusion, the ensemble fidelity for a given frequency is significantly better than that for singles above ~20 MHz.

The impact of temperature on fidelity, shown in Figure 3.4b, follows expectations as decreasing the temperature of either system will improve the fidelity until approximately 2.5 K, where the rate of dephasing approaches the relaxation rate. At high temperature the

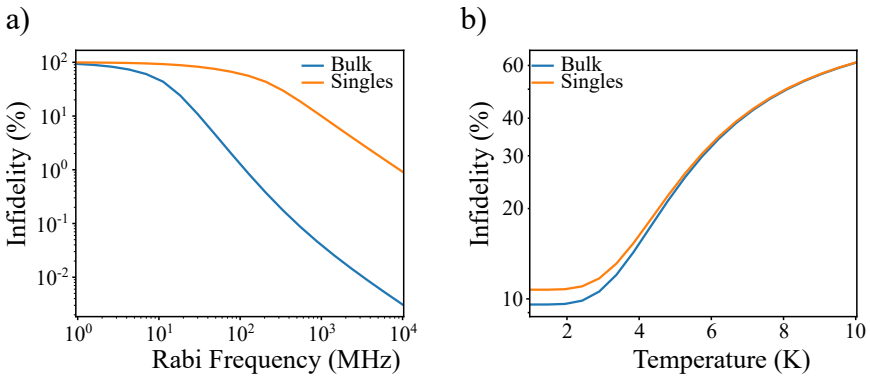

Figure 3.4: Simulated two-level π-pulse fidelities per a) Rabi frequency and b) temperature. A Rabi frequency of 1 GHz was used for the temperature sweep.

bulk and single centre apparatuses considered here have nearly identical fidelities, but as they approach the lifetime limit the difference in spectral diffusion separates the fidelity for bulk and singles.

3.4 Three-Level System

We now consider the electron spin and optical transitions in a Λ-system, as in §2.2.6. While the T-centre is better represented by a four-level model, the Λ-system model is computationally simpler to run and we shall show in §3.5 that the four-level model can be treated as a small perturbation on a three-level model in some relevant cases. The two ground states of the Λ-system are the electron spin states, and they share a common excited state. Based on Figure 2.1, the two optical transitions to drive could either be A/B or C/D. To set the convention for these simulations, $|\downarrow_H\rangle$ was chosen for the excited state with transitions A and B. For simplicity, we write

$$\{|\downarrow_E\rangle = |0\rangle\,, |\uparrow_E\rangle = |1\rangle\,, |\downarrow_H\rangle = |2\rangle\}, \tag{3.4.1}$$

such that the electron spin qubit is represented by the typical $|0\rangle$, $|1\rangle$ notation.

We define our system in the reference frame of the $|0\rangle$ state. The full three level system can be seen in Figure 3.5. The two optical Rabi frequencies, Ω_1 and Ω_2, correspond to the $0\leftrightarrow2$ and $1\leftrightarrow2$ transitions (B and A) respectively. The detunings for these transitions are given by Δ_1 and Δ_2, with the two-photon detuning from $|0\rangle$ to $|1\rangle$ given by $\delta = \Delta_2 - \Delta_1$. The excited state relaxation will be given by Γ and the optical dephasing by γ. The electron spin dephasing is then denoted by γ_e.

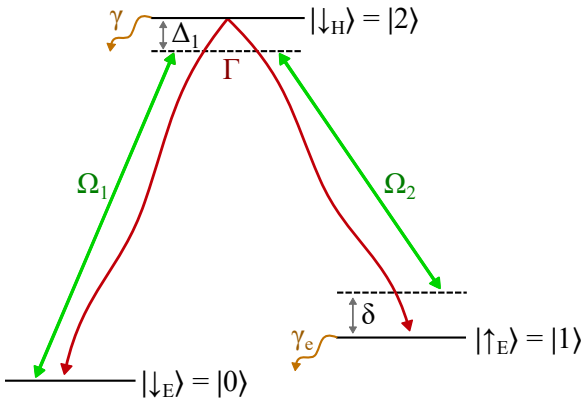

Figure 3.5: Λ-system energy level diagram. Each optical transition has a corresponding Rabi frequency Ω_n. The detunings for the Λ-system are Δ_1 and δ for $|\downarrow_H\rangle$ and $|\uparrow_E\rangle$ respectively. The relaxation and dephasing terms are represented as Γ, γ, and γ_e.

We define our system in the same form as in §2.2.6, but now with an additional electron spin dephasing term $\hat{C}_{11}$:

$$\begin{aligned}\hat{H} = &-\hbar\left(\Delta_1\hat{\sigma}_{22} + \delta\hat{\sigma}_{11}\right) \\ &-\hbar\left(\Omega_1\hat{\sigma}_{20} + \Omega_2\hat{\sigma}_{21} + \Omega_1^*\hat{\sigma}_{02} + \Omega_2^*\hat{\sigma}_{12}\right),\end{aligned} \tag{3.4.2}$$

$$\hat{C} = \begin{cases} \sqrt{\Gamma}\left[\hat{\sigma}_{20} + \hat{\sigma}_{21}\right], \\ \sqrt{\gamma}\hat{\sigma}_{22}, \\ \sqrt{\gamma_e}\hat{\sigma}_{11}. \end{cases} \tag{3.4.3}$$

Due to the long time scale of the electron spin dephasing (> 2 ms), many scenarios take place on timescales where $\gamma, \Omega \gg \gamma_e \approx 0$. However, this term has been included for when the optical control timescale begins to approach milliseconds. We can rewrite our Rabi frequencies in terms of a magnitude and phase in order to make the phase a defined parameter for each transition. This gives us the transformation $\Omega \to \Omega e^{i\phi}$.

Spectral diffusion has been implemented similarly to the two-level scenario, such that the excited state varies under spectral diffusion, but the ground states do not.

Having established the structure of the T-centre in a three level model, we can next begin to apply time-dependent optical schemes to determine their viability for all-optical manipulation of the electron spin qubit. The following simulations, unless otherwise stated, have the initial state $|0\rangle$ and record the fidelity of transitioning to $|1\rangle$ (flipping the electron spin). When not otherwise specified, the Rabi frequency is set to 100 MHz. The detuning will be set to 0 GHz and 10 GHz for StiRAP and the far-detuned Raman schemes respectively.

3.4.1 Stimulated Raman Adiabatic Passage

We start by looking at the Stimulated Raman Adiabatic Passage (StiRAP), following the pulse sequence outlined in §2.4.2. In Figure 3.7a, as the Rabi frequency decreases, the

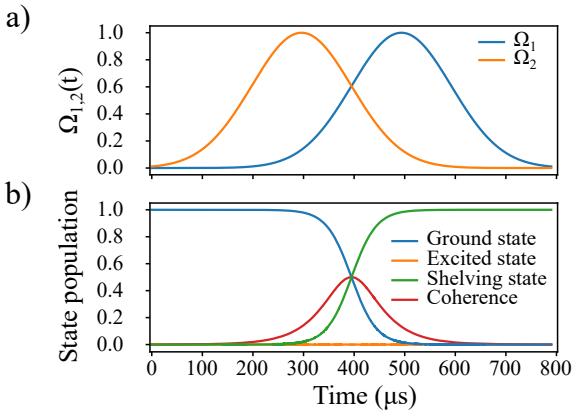

Figure 3.6: Three-level simulation of StiRAP for the T-centre in the single centre apparatus. a) $\Omega_{1,2}$ normalized and varied in time according to the optical pulse scheme. $\Omega_{1,2} = 100$ MHz at the maximum, and $\Delta_{1,2} = 0$ MHz. b) The population and coherence plotted with respect to time.

fidelity worsens because the adiabatic criteria from Eq. 2.4.10 is no longer met. However, the improvement in fidelity from increasing $\Omega_{1,2}$ begins to have diminishing returns after a certain point where the adiabaticity has been sufficiently satisfied. For our parameters, this occurs around $\Omega = 100$ MHz for bulk and $\Omega = 5$ GHz for singles.

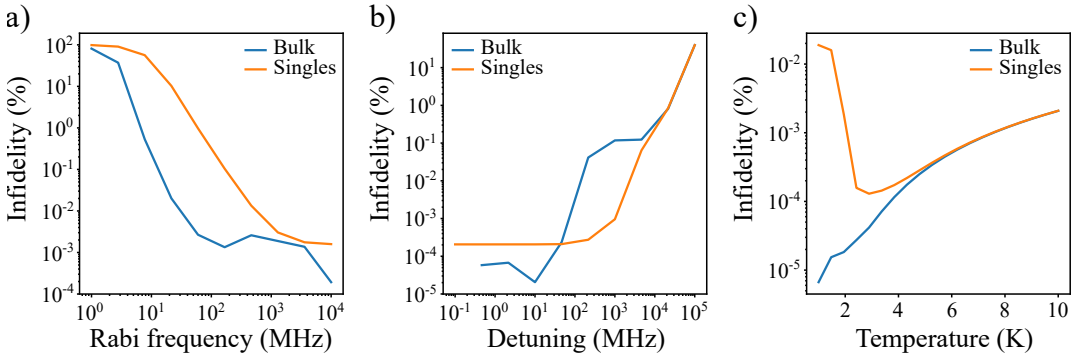

Figure 3.7: Three-level simulation of StiRAP fidelities. a) StiRAP fidelity for a fixed time interval with a varied maximum Rabi frequency. b) Fidelity with respect to detuning for a Rabi frequency of $\Omega_{1,2} = 100$ MHz. c) Fidelity with respect to temperature for $\Omega_{1,2} = 100$ MHz.

Shown in Figure 3.7b, the fidelity improves as the temperature drops from 10 K down to 3 K. However, below 3 K the infidelity for the single centre apparatus begins to spike back up.

Finally, Figure 3.7c shows that as the optical fields are detuned from the optical resonances, the StiRAP fidelity decreases. The bulk apparatus shows better fidelity for a given Rabi frequency and temperature. Optimally both systems would operate near zero detuning, in which case the bulk apparatus exceeds 99.999%.

3.4.2 Far-Detuned Raman Scheme

We now explore the far-detuned Raman scheme in which the two-photon resonance is driven using bichromatic square pulses. Being far off resonance, the pulse times for a given optical power will be greatly increased, following the effective Rabi frequency in Eq. 2.4.11. A balance must be struck between π-pulse time and fidelity.

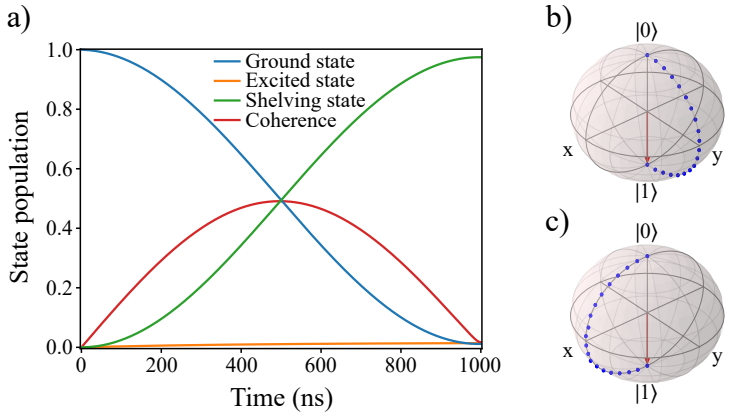

Figure 3.8: Simulated far-detuned Raman control. a) Population response to a far-detuned Raman π-pulse with $\Omega_{1,2} = 100$ MHz and $\Delta_{1,2} = 10$ GHz, such that $\Omega_{\text{eff}} = 1$ MHz. Bloch sphere representation of the π-pulse rotation, where b) $\phi_2 - \phi_1 = 0$, corresponding to an x-axis rotation, and c) $\phi_2 - \phi_1 = \pi/2$ radians, corresponding to a y-axis rotation.

Figure 3.8 shows far-detuned driving can result in a spin π-pulse with minimal population driven to the excited state. This far-detuned scheme is operating on a µs timescale while StiRAP takes nearly 1 ms for the same Rabi frequency. The Bloch sphere evolution of the electron spin qubit (Fig. 3.8b and c) illustrates how changing the phase relation between the two optical fields leads to a change in the axis of rotation. Adjusting the integrated pulse area will in turn adjust the angle of rotation. Two orthogonal axes of rotation will be able to produce any arbitrary rotation.

We consider how the π-pulse fidelity changes with Rabi frequency, detuning, and temperature. Figure 3.9a shows the infidelity as a function of the Rabi frequency. As the Rabi frequency decreases, the fidelity improves for both the bulk and single apparatus parameter sets. Recall from §2.4.3 that the condition for far detuning is maintaining $|\Delta_{1,2}| \gg \gamma, \Omega_{1,2}$, and, with a fixed $\Delta_{1,2} = 10$ GHz, once the Rabi frequency dips below 1 GHz the change in fidelity becomes significantly smaller as the detuning condition has been satisfied. When the pulse scheme is operating in the far-detuned regime, we see that

the bulk apparatus fidelity separates from that for the single centre apparatus with a noticeably better fidelity for the bulk case. Once the Rabi frequency drops below ∼5 MHz the effective Rabi frequency approaches the electron spin dephasing rate (500 Hz), which leads to an increase in infidelity.

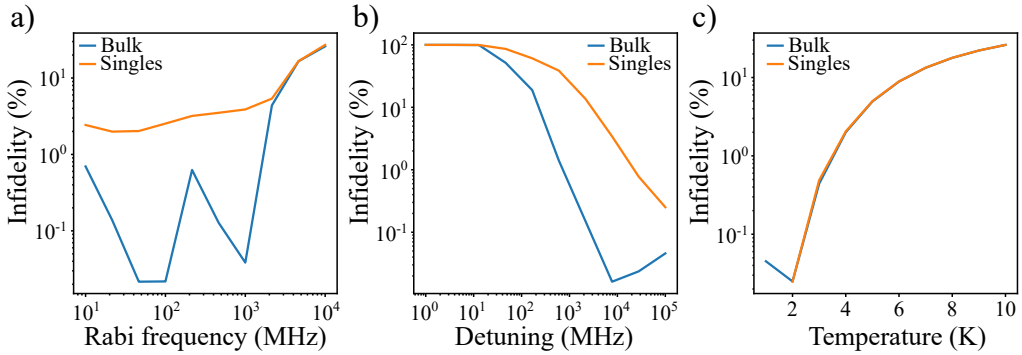

Figure 3.9: Simulated far-detuned Raman π-pulse fidelities relative to a) Rabi frequency, b) excited state detuning, and c) temperature.

Figure 3.9b shows the relationship between the infidelity and single transition detuning. With a Rabi frequency of 100 MHz, once the detuning drops below 500 MHz the fidelity drops below 90% for both parameter sets. The bulk apparatus is able to tolerate smaller detunings due to the smaller dephasing that plays into the detuning condition, leading to much better fidelities for a given Rabi frequency and detuning.

The temperature dependence of this scheme is explored in Figure 3.9c. The difference between the bulk apparatus and single centre apparatus response to the temperature is negligible.

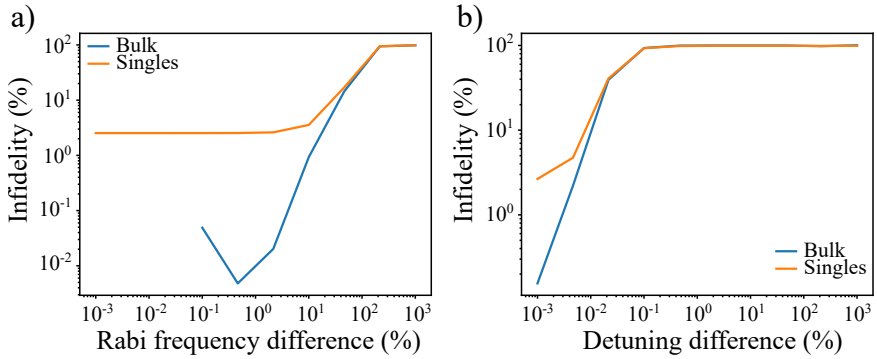

Figure 3.10: Simulated far-detuned Raman π-pulse fidelities per difference in a) Rabi frequency and b) excited state detuning.

Finally, we consider how disparities in the Rabi frequency and excited state detuning between the transitions impact the fidelity. We are considering static differences to simulate the error in matching the power of two lasers and setting their frequency separation. In Figure 3.10a we see that the fidelity remains mostly unchanged until the frequency dif-

ference reaches 10% of the magnitude of the Rabi frequency, at which point the fidelity quickly drops below 90%. We keep the pulse length constant, but the effective Rabi frequency changes as the difference increases. The Raman scheme breaks down when the field becomes effectively monochromatic.

The fidelity is more sensitive to detuning differences. Figure 3.10b shows that only a 0.001% difference can be tolerated in the bulk detuning to keep the fidelity above 90%. By deriving $\Omega_{1,2}$ from the same laser, the detuning difference can be made very small ($<$ 0.0001 %). A highly stable laser source in amplitude and frequency will then be necessary to drive such a system with this scheme.

The highest fidelities in this far-detuned Raman scheme were seen with the bulk apparatus. With these parameters, we simulated fidelities $>$ 99.9%. The best fidelity was simulated with $\Omega_{1,2} = 10$ MHz, $\Delta_{1,2} = 10$ GHz, and $T = 1.5$ K for the bulk apparatus. Achieving such a Rabi frequency with bulk excitation requires a 412 mW laser based on Eq. 3.2.1 assuming the worst case bound $\eta_R = 0.03$. Such a laser power can be achieved using optical amplification, meaning that we could reasonably achieve π-pulse fidelities $>$ 99.9% using the far-detuned Raman scheme.

3.5 Four-Level System

We now consider the addition of the upper excited state of TX_0. We will show this effects the detuning dependence of both stirap and Raman control. It has been shown in previous work that the addition of a second Λ-system can affect the scheme fidelity [55, 68, 7]. We show in this section that the four-level system is a small perturbation of the three-level system.

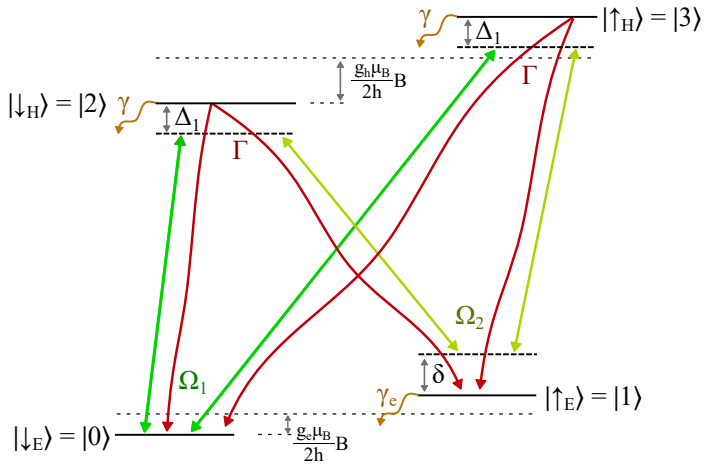

Figure 3.11: Four-level energy level diagram.

Figure 3.11 shows the four-level structure in which two optical fields drive an additional, parasitic Λ-system. We have defined Ω_1 as the laser responsible for both transitions

stemming from $|0\rangle$ and Ω_2 as the laser for the transitions from $|1\rangle$. This represents the double Λ-system produced by having two excited states. The Λ-system for $\{|0\rangle, |1\rangle, |2\rangle\}$ has been mirrored for $\{|0\rangle, |1\rangle, |3\rangle\}$. This expanded Hamiltonian is

$$\begin{aligned}\hat{H} = &-\hbar\left[-\frac{g_e\mu_B B}{2\hbar}\hat{\sigma}_{00} + (\delta + \frac{g_e\mu_B B}{2\hbar})\hat{\sigma}_{11} + (\Delta_1 - \frac{g_h\mu_B B}{2\hbar})\hat{\sigma}_{22} + (\Delta_1 + \frac{g_h\mu_B B}{2\hbar})\hat{\sigma}_{33}\right] \\ &-\hbar\left[\Omega_1(\hat{\sigma}_{20} + \hat{\sigma}_{30}) + \Omega_2(\hat{\sigma}_{21} + \hat{\sigma}_{31}) + \Omega_1^*(\hat{\sigma}_{02} + \hat{\sigma}_{03}) + \Omega_2^*(\hat{\sigma}_{12} + \hat{\sigma}_{13})\right].\end{aligned} \tag{3.5.1}$$

The Zeeman splitting is given by $\frac{g_{e,h}\mu_B B}{\hbar}$, where $g_{e,h}$ is the corresponding Lande g-factor, μ_B is the Bohr magneton, and B is the magnetic field. Regarding the detuning Δ to attach to state $|3\rangle$, we are still working in the reference frame of the unshifted $|0\rangle$ state, so we use Δ_1 for the detuning. In this configuration the parasitic Λ-system is strongest for blue-detunings, which will lead to an asymmetry in detuning behavior.

In the four-level system, only one Λ-system can have zero excited state detuning at a given time. This means that there is always a parasitic detuned Λ-system when there is a two-photon resonance in the ground state. We can therefore expect that StiRAP will have worse performance in the four-level system.

In practice laser 1 can also address transitions $1 \leftrightarrow 2$ and $1 \leftrightarrow 3$ and vice versa from multi-path dynamics, which will lead to two additional parasitic Λ-systems, where the $\delta = 0$ condition is not maintained. This will lead to another source of fidelity loss for StiRAP. In the far-detuned scheme, the two additional Λ-systems will negatively impact the fidelity, but because these systems are also far-detuned, we expect this to have a small effect on fidelity. Unfortunately, this model cannot simulate this behavior to quantify the impact of this process.

The collapse operators are duplicated for the additional excited state with no further changes:

$$\hat{C} = \begin{cases} \sqrt{\Gamma}\left[\hat{\sigma}_{20} + \hat{\sigma}_{21} + \hat{\sigma}_{30} + \hat{\sigma}_{31}\right] \\ \sqrt{\gamma}\left[\hat{\sigma}_{22} + \hat{\sigma}_{33}\right] \\ \sqrt{\gamma_e}\hat{\sigma}_{11}. \end{cases} \tag{3.5.2}$$

Spectral diffusion is carried out with the same discrete sampling as in §3.4. Following the development of this model, we successfully used it to fit the optical spectrum of a single T-centre at field in Ref. [27].

We expect an asymmetry between red and blue detunings because blue detuning from the lower excited state will lead to a resonance with the higher energy excited state.

3.5.1 Stimulated Raman Adiabatic Passage

Figure 3.12 shows the StiRAP infidelity for the bulk and single centre apparatuses simulated using both the three- and four-level systems as a function of the excited state detun-

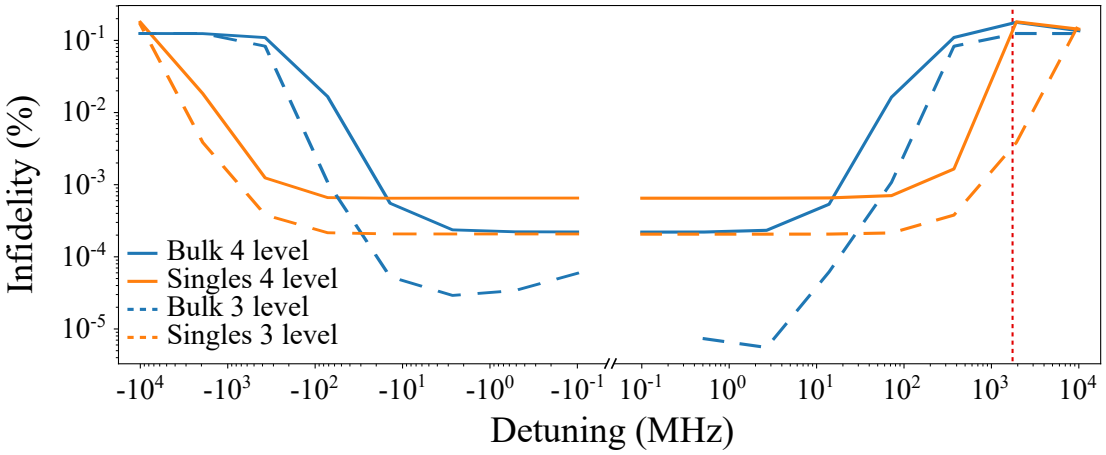

Figure 3.12: Comparison of simulated StiRAP fidelities between the three- and four-level systems. The infidelity is plotted relative to the excited state detuning. The parasitic excited state is indicated by the red dotted line.

ing. For small excited state detunings, the infidelity of the bulk simulation increases by one to two orders of magnitude when including the parasitic excited state. When the excited state detuning becomes larger than the excited state splitting (∼3.8 GHz), the three- and four-level simulations converge. A small difference in behavior exists for the four-level system between the positive and negative detunings in the range of the excited state splitting. This change is most clearly seen in the difference in the positive and negative detuning infidelity of the four-level singles.

3.5.2 Far-Detuned Raman Scheme

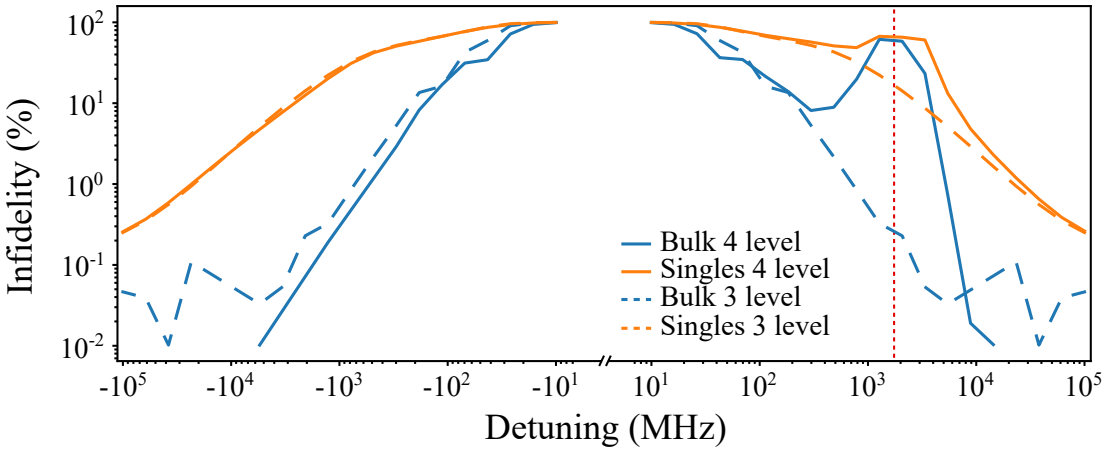

Figure 3.13: Comparison of simulated far-detuned Raman pulse fidelities between the three- and four-level systems. The infidelity is plotted in relation to the excited state detuning, which is relative to the lower excited state. The detuning for the higher energy excited state is indicated by the red dotted line. $\Omega_{1,2} = 100$ MHz

Figure 3.13 shows the comparison of the three-level and four-level systems when using the far-detuned Raman pulses. When introducing the parasitic Λ-system, we recalibrate the π-pulse time for each case. Focusing on the negative detuning region, the infidelity for singles is relatively unchanged. For the bulk apparatus, there is a slight improvement in the π-pulse fidelity, which becomes more apparent as the detuning increases. On the positive detuning side, we see a region about the value of the excited state splitting ($\sim$3.8 GHz) where the optical fields come into resonance with the second excited state.

Unlike StiRAP, the far-detuned Raman scheme proves resilient to the addition of a second excited state outside of the parasitic resonance. In some instances the fidelity is improved due to the simultaneous driving of two Λ-systems.

With the three-level model we determined that a $> 99.9\%$ fidelity in π-pulse rotations can be achieved with the reasonable parameters $\Omega_{1,2} = 10$ MHz, $\Delta_{1,2} = 10$ GHz, and $T = 1.5$ K for the bulk apparatus. Under these same conditions, the four-level system shows that only a fidelity of $< 95.3\%$ is achievable. This parameter set results in a π-pulse time approaching T_{2e}, and the π-pulse time is longer in the four-level system, leading to a $\approx 4.6\%$ decrease in fidelity.

However, with $\Omega_{1,2} = 100$ MHz and $\Delta_{1,2} = 10$ GHz, fidelities $> 99.9\%$ can be achieved with the bulk apparatus according to the four-level model. Rabi frequencies at 100 MHz or greater require a laser power greater than 1 W even with the optimal bound $\eta_R = 1$ in the bulk apparatus, which is not a reasonable regime. To achieve 100 MHz Rabi oscillations in the single centre apparatus, only 2.6 µW are required in the worst case scenario that $\eta_R = 0.03$. The limited cooling capability reduces the fidelity of the current single centre apparatus, but should a similar apparatus be developed in the future to address single centres at 1.5 K, optical control of the T-centre with fidelities $> 99.9\%$ could be achieved under reasonable conditions.

3.6 Summary

These simulations show that optical control of T-centre through the far-detuned Raman pulse scheme can reasonably achieve fidelities $> 99.9\%$ with confocally-addressed single T-centres at 1 K. With the equipment available for this thesis, we predict higher fidelities using the bulk spectroscopy apparatus from Bergeron et al. [10]. These results indicate that T-centre optical control could be achieved with 95.3% fidelities with the bulk spectroscopy apparatus.

The two-level simulation indicated that visible Rabi oscillations could be seen with laser powers of 103 mW and 16 µW for the bulk apparatus and the single centre apparatus. In §4.1 we develop a narrow-linewidth laser system for this application, capable of delivering up to 1W of laser power. However, the single centre apparatus would require pulsing faster than 500 MHz, beyond the capabilities of this laser system.

Taking these simulations into consideration, we determined that the bulk spectroscopy apparatus with an isotopically enriched sample was the more promising optical control testbed.

Chapter 4

Experimental Design and Methods

Optical control requires a stable, coherent laser source and optically-addressable spin states. To handle these requirements we developed a multi-channel, ultra-stable laser system as well as two magnetic field apparatuses for applying fields to bulk ^{28}Si T-centre samples. The two different magnetic field setups attain the different regimes and requirements for the optically-driven Rabi oscillations, hyperfine ODMR, and optical CPT experiments in this work. The apparatus used for demonstrating optical Rabi oscillations used a rotational sample mount between two disk magnets. An apparatus with a variable magnetic field produced by a Helmholtz coil array was used for both the hyperfine ODMR and optical CPT measurements due to the fine control over the magnetic field orientation and strength. All experiments made use of the multi-channel, ultra-stable laser system.

4.1 Multi-Channel Ultra-Stable Laser

The key requirements of a laser for this work include a narrow linewidth, frequency stability, fine tuning of the laser frequency, coherence, and high-powered pulsing. CPT and optical control schemes require multiple independently tunable and pulsable, coherent optical fields. Finally, driving optical Rabi oscillations requires fields at powers up to 103 mW as determined in §3.2. The laser apparatus we built in this work satisfies all of these requirements. With an ultra-stable tunable laser source, it will be possible to probe narrow spectral features below the resolution limit of Bergeron et al. [10], MacQuarrie et al. [45], and Higginbottom et al. [27], such as the CPT linewidth $\Delta\omega_{\mathrm{CPT}} \geq 1/T_2 \approx 500$ Hz. We therefore target a laser linewidth < 1 kHz.

The core of the laser is a seed laser with feedback from a stable reference cavity from Stable Laser Systems. This stabilized laser source is split, modulated, and filtered, producing two coherent laser channels that can be independently frequency tuned. Finally, the laser signal is amplified through optical amplifiers that can be pulsed. The schematic of this apparatus is shown in Figure 4.1.

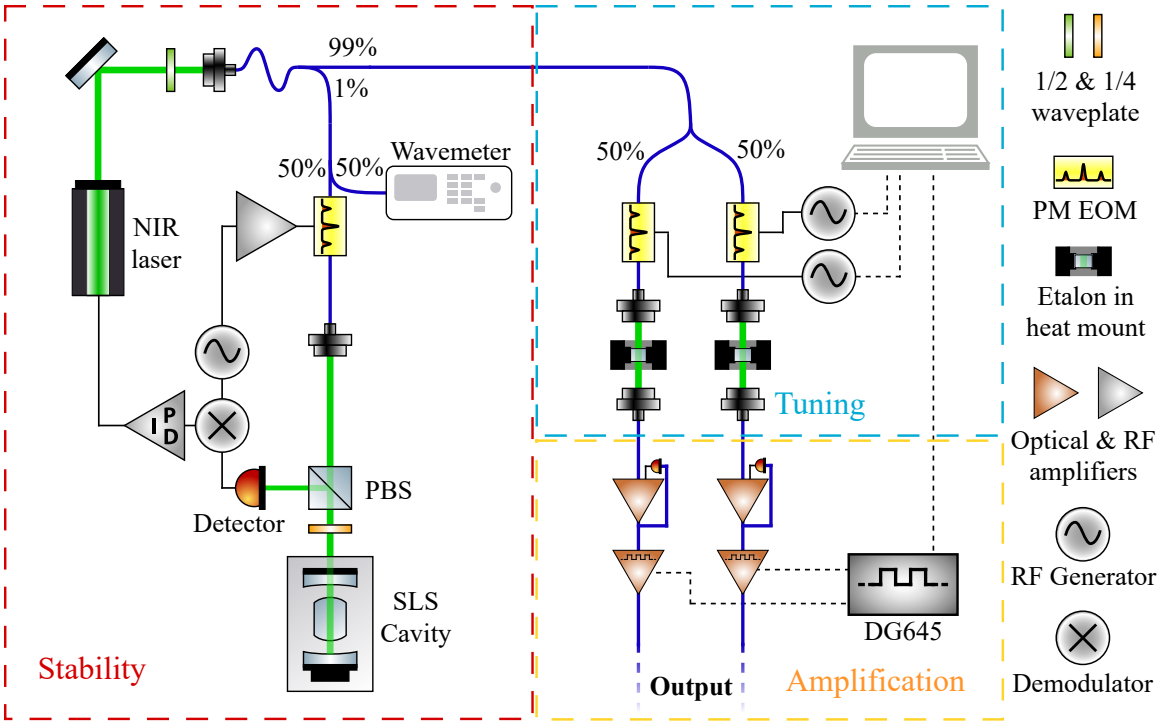

Figure 4.1: The tunable ultra-stable laser. There are three major sections: stability, tuning, and amplification.

4.1.1 Stability: Laser Locking

Locking a laser to an external reference improves stability and can reduce the laser linewidth by eliminating phase fluctuations. There are three main components involved in locking this laser: a narrow linewidth Fabry-Perot (FP) cavity, feedback control electronics, and the laser itself. A small portion of the laser is picked off and sent to the FP cavity, where the reflected signal from the cavity is then picked up by a detector.

Seed Laser and Control Electronics

The seed laser is the DL100 pro from Toptica. This is a tunable diode laser with a wide range of 1270–1350 nm and max output power of 50 mW. The DL100 is coupled using a collimator into a polarization maintaining (PM) fibre. A half-wave plate (HWP) in the collimated beam adjusts the polarization. Once in fibre the laser signal is split using an in-fibre 99:1 beam splitter. 99% of the signal will be sent to be tuned and used for experimentation. A 50:50 splitter was used in order to send some of the 1% tap to a Bristol 871 wavelength meter. The remaining portion of the 1% tap is sent to our cavity.

Natively, the DL100 has a linewidth of 1–2 MHz, but we improve the linewidth and stability with a Pound-Drever-Hall (PDH) laser lock [13]. In a Toptica PDD 110F, the detector signal is demodulated, producing an anti-symmetric error signal about the peak or

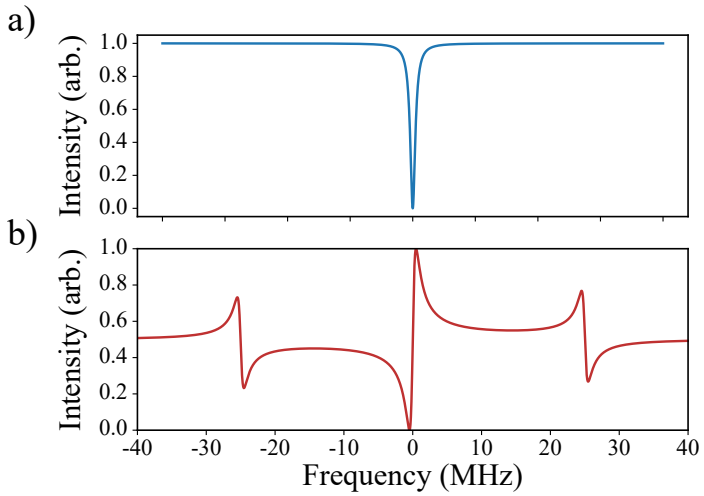

Figure 4.2: Example illustrating a) a cavity resonance and b) a PDH error signal b). The cavity linewidth is larger than the SLS cavity by a factor of ∼10 for the purpose of visualization. All other parameters roughly match the setup, including the modulation frequency (25 MHz) and free spectral range (1.5 GHz)

dip of the resonance (see illustration Fig. 4.2). The PDD 110F handles the PDH error signal generation and produces a sine wave modulation signal with a frequency of 25 MHz.

Feedback to the laser is produced by a proportional–integral–derivative (PID) control loop [4]. A Toptica FALC 110 provides an integrated PID loop into the control electronics for the DL100, allowing for a stable lock over the course of days.

Optical Modulation

To modulate the portion of the laser signal in the path used for locking we use a fibre coupled phase modulating EOM from Jenoptik. Designed for 1310 ± 50 nm, the PM1310 can handle optical signals up to 300 mW and RF frequencies up to 1 GHz. We use an LZY-22+ amplifier from Mini-Circuits to drive the EOM. This amplifier can handle frequencies from 0.1-200 MHz.

Ultra-Stable Fabry-Perot Cavity

Our Fabry-Perot cavity comes from Stable Laser Systems with a free spectral range (FSR) of ≈1.5 GHz and finesse $\mathcal{F} \approx 15,000$ for light near 1325 nm. To relate these values to the cavity linewidth we use the equation

$$\Delta\nu_c = \frac{\Delta\nu_{FSR}}{\mathcal{F}}, \tag{4.1.1}$$

where $\Delta\nu_c$ is the cavity linewidth and $\Delta\nu_{FSR}$ is the cavity FSR, giving a cavity linewidth of $\sim$ 100 kHz. The cavity comprises two mirrors 1" in diameter with anti-reflective (AR)

coatings on the external sides. The cylindrical cavity is housed horizontally in a vacuum chamber with a connected heater and thermistor in order to control both pressure and thermal fluctuations. The temperature of the cavity is set to the zero expansion point of the cavity, which in our case is 36.98 °C.

Resonances		
Wavenumber (cm-1)	Frequency (GHz)	Notes
7541.633	226092.47	∼-5 GHz from ^{28}Si T ZPL
7541.683	226093.97	
7541.733	226095.46	
7541.783	226096.96	Closest to ^{28}Si T ZPL
7541.833	226098.46	
7541.883	226099.96	
7541.933	226101.45	∼+4 GHz from ^{28}Si T ZPL
7541.983	226102.95	

Table 4.1: Notable resonances of the SLS cavity in the vicinity of the ^{28}Si T-centre ZPL that are useful for locking the laser.

A collimator takes the linearly-polarized laser out of the fibre in a collimated beam through a free-space optics array aligned to the input of the cavity. The laser initially passes through a Wollaston prism polarizing beam splitter (PBS) and a quarter-wave plate. The reflected beam from the cavity will pass back through the quarter-wave plate resulting in a total 90° rotation in polarization. Re-entering the PBS with an orthogonal polarization, the light now refracts at a different angle. The refracted beam is sent to a FPD510-FC-NIR detector from Menlo-Systems with a 250 MHz bandwidth. The output from this detector is sent directly to the PDH module. The free-space optics and cavity are mounted to a breadboard with Herzan AVI vibration isolating legs to reduce vibrations from the table passing on to the cavity system.

The cavity linewidth $\sim$ 100 kHz is sufficient for a laser linewidth $<$ 1 kHz with optimized PID parameters. The 1.5 GHz FSR provides adequately fine spacing for locking locations since our tuning components can utilize a ∼5 GHz range. The resonances about the T-center lines in ^{28}Si are given in Table 4.1 with notable resonances labelled.

4.1.2 Tuning: Laser Modulation

In order to properly make use of the stabilized laser, there needs to be some means of tuning the laser over the relevant spectral features of the T-centre. To accomplish this we use tunable sidebands from optical modulation and spectral mode filtering to keep only the desired frequency from the modulated laser. In addition, this section of the laser

setup splits the laser into two channels such that two independent laser frequencies can be produced.

Tunable Optical Modulation

Using all PM components the laser is separated into two channels by a 50:50 splitter. In order to modulate up to 6 GHz we use MPZ-LN-10 phase modulating EOMs from iXblue, which are rated up to a 10 GHz RF modulation and 16 mW input optical power. These EOMs are paired with DR-AN-10-MO RF amplifiers from iXblue to provide the necessary modulation strength to optimally populate the first order sidebands. Each fibre path goes through an in-line polarizer (ILP) before passing through an EOM in order to clean up the polarization before modulation, which is polarization dependent.

To produce the modulation signals we use Stanford Research Systems (SRS) SG386 signal generators, which operate up to 6.075 GHz. The frequency stability is rated as $< 10^{-11}$ Allan variance for 1 second. Comparing this stability to the measured stability in §4.1.4, we conclude that modulation does not significantly impact the linewidth of the laser.

Sideband Filtering

After the EOM we are left with a modulated signal, and all that remains is to isolate a single sideband. After the EOM in each path, the beam exits the fibre through a collimator in order to pass through a solid-silica etalon from Light Machinery in free space. A collimator at the output couples the light back into PM fibres where it is sent to the final section of the laser preparation. Etalons act as fixed-separation FP cavities, allowing for spectral filtering. The etalons we use have a rated FSR of 80 GHz and finesse > 100 near 1300 nm. This gives a linewidth of 800 MHz. The peak transmission through the resonance of each etalon is rated at $> 65\%$.

If we assume that our sideband is passing through the center of the etalon resonance, then the extinction of the carrier in transmission should be > 10 dB as long as it is more than the full width of the etalon resonance separated from its sideband. We avoid going below 1 GHz to ensure carrier extinction > 10 dB. For the best results the laser is locked to an SLS cavity resonance 5 GHz from the target frequency, where the carrier extinction exceeds 20 dB. Figure 4.3 illustrates the selective filtering used to pick out a single, tunable laser frequency.

In order to shift the resonance to the range of interest, the etalons can be tuned both by angle and temperature. Angle tuning requires fine control and results in changes to the linewidth of the etalons. Therefore, the etalons have been aligned such that the incident light is normal to the surface while individually mounted in a temperature controlled lens tube. We use the Thorlabs SM1L10HR mount along with the TC200 temperature controller

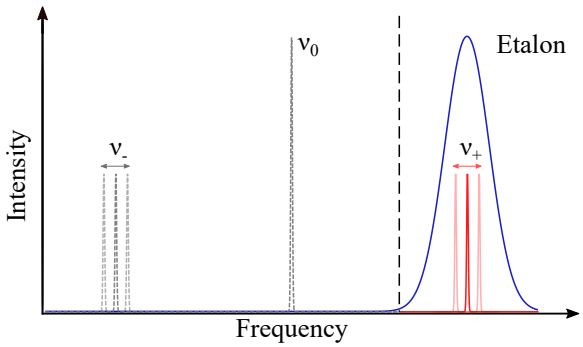

Figure 4.3: Visualization of sideband filtering to select a tunable sideband. The three peaks ν_0, ν_+, and ν_- represent the carrier and first order sidebands. The etalon resonance is represented by the light blue curve. In this example the sideband ν_+ has been selected.

in order to stabilize and tune the temperature. To ensure the etalons are isolated from environmental temperature changes, a window sits on either side of the etalon in the temperature mount with AR coating for O-band light. For a given resonance near 1326 nm, the frequency will decrease by approximately 1.3 GHz per degree Celsius. The frequency response to temperature for etalon resonances can be seen in Figure 4.4. Tuning the etalon resonance by temperature is slow, particularly when cooling down, but fortunately most experiments run with this setup do not need to scan over a range greater than ~1 GHz. Through the use of amplitude stabilization described in §4.1.3, this range in frequency does not require sweeping the etalon temperature with the laser frequency.

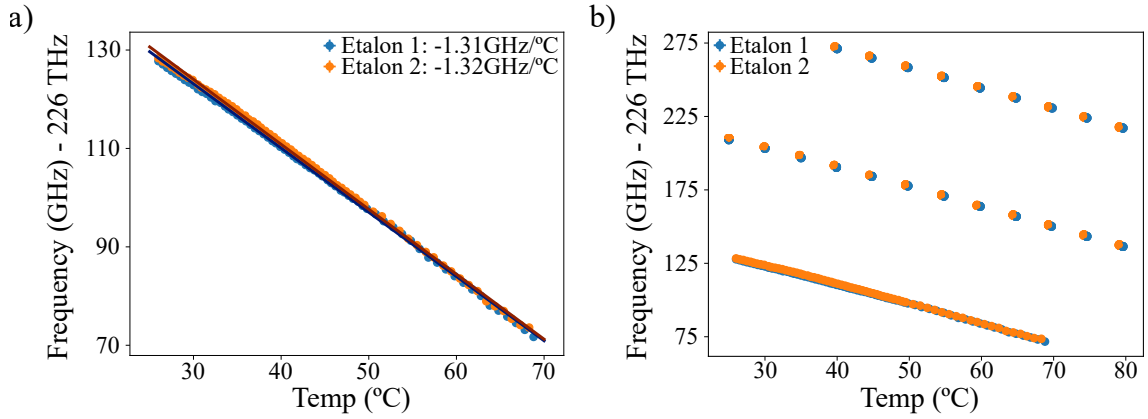

Figure 4.4: Measured etalon resonance frequency versus temperature. a) Primary etalon resonance used for tuning to ^{28}Si T-centre ZPL features. b) The primary resonance shown along with two other higher energy resonances separated by the 80 GHz FSR. The slight non-linearity in the temperature tuning range can be attributed to the temperature not having totally settled

4.1.3 Amplification & Pulsing

By the time the laser has passed through all of the optical components of the past two sections, the power has dropped by a factor of $> 10^3$, requiring amplification in order to reach the necessary powers for experimentation. In addition, optical amplifiers with a low power input allow for easily tunable power, power stabilization, and optical pulsing. Through the use of two amplifiers per channel, we make use of all of these features.

Amplitude Stability

In order to prevent unintended power fluctuations from back-reflections, in-fibre isolators are used on both ports of each optical amplifier. The first set of optical amplifiers are the Thorlabs BOA1017P, which operate between 1290-1330 nm. This amplifier is mounted using its butterfly package in a Thorlabs CLD1015, which provides temperature and current control. With temperature held constant, they can be set in either constant current or constant power mode. In order to run in constant power mode, there needs to be some sampling of the output power. Because the BOA1017P does not have an internal reading for the output power, we have mounted a Thorlabs FGA01FC InGaAs photodiode to measure the power. An in-fibre 99:1 splitter is used after the amplifier, where the 1% port is sent to the photodiode. Stabilizing the power in a low range (20–50 µW) has two important benefits: increasing the operational range of the laser for a fixed etalon resonance position and allowing for maximal extinction between the on and off powers of the following amplifiers when they are pulsing. With the set power low as the laser is scanned across the

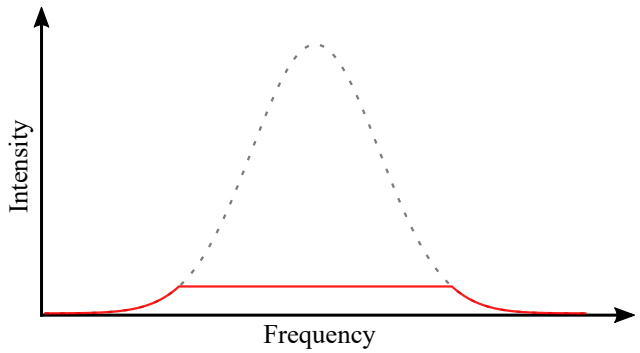

Figure 4.5: Visualization of amplitude stabilization across an etalon resonance. The dotted line represents the etalon resonance, while the red line is the stabilized output power.

resonance of an etalon, the laser amplitude has a flat response between 1.5 GHz and 2 Ghz about the centre frequency.

Pulsed and Tunable Amplification

Following the initial optical amplifiers that stabilize the signal amplitude, the laser passes through Aerodiode semiconductor optical modulators (SOM) with high pulse-performance

(SOM-HPP-S1310). These SOMs are rated for 23 dB gain for small input signals, with a max output of 30 mW. They can operate in a constant current mode or a pulsed mode where the on and off powers can be independently set. In pulsed mode the extinction ratio is 50 dB assuming the input signal is not greater than 10 mW. The pulse switch speed between the on and off state is 1 ns, with a repetition rate of 250 MHz.

After the final isolators in each channel, the two channels are recombined in-fibre using a 50:50 splitter/combiner. We use an SRS DG645 delay generator to pulse the SOMs, which can generate square pulses with a resolution of 5 ps and max repetition rate of 10 MHz.

4.1.4 Laser Linewidth Measurement

We characterized the laser linewidth, confirming that it will operate with sufficient stability for the later experiments. The targeted linewidth ($<$ 1 kHz) is much smaller than the resolution of any spectrometer. We utilize a heterodyne detection scheme [44] to determine the laser linewidth based on the fast Fourier transform (FFT) of a beat signal.

No other laser in our possession should be able to match the linewidth stability of this laser setup, meaning the laser will have to be compared to itself. We separate two frequency channels by 50 kHz and send one through a 25 km fibre to produce a 83 µs delay. The two channels are recombined and sent to a Thorlabs FPD510-FC-NIR detector with a 250 MHz bandwidth, which provides ample headroom to sample the 50 kHz beat signal. The detector output voltage was then processed using the FFT of the Agilent Technologies DSO9254A oscilloscope.

This measurment scheme will be limited in its ability to determine the laser linewidth by the path difference between the two channels. To determine the measurement limit, we consider the case where the laser is coherent along the length of the fibre. The linewidth ($\Delta\nu$) for a laser of a given coherence length (L) is

$$\Delta\nu = \frac{c}{n\pi L}\,, \tag{4.1.2}$$

where c is the speed of light and n is the index of refraction. Our fibres have an index of refraction of 1.47 [47]. We find that the corresponding linewidth for a coherence length of 25 km is 2.6 kHz. This means that the lowest linewidth measurable by this setup will be 2.6 kHz, while larger linewidths, which correspond to shorter coherence lengths and times, should be accurately measured.

Looking at Figure 4.6, we see the resulting FFT spectra about 50 kHz. We can see two harmonic peaks split $\pm$0.4 kHz from our beat frequency. 0.4 kHz corresponds to the feedback timescale of the PID electronics in the PDH loop. The center line can be fit to a Gaussian curve, and we find that the FFT linewidth is 3.84 Hz, though because the measurement corresponds to the difference between two frequency signals, the laser linewidth should then be half this value, 1.92 Hz. Since our measured linewidth is well below the

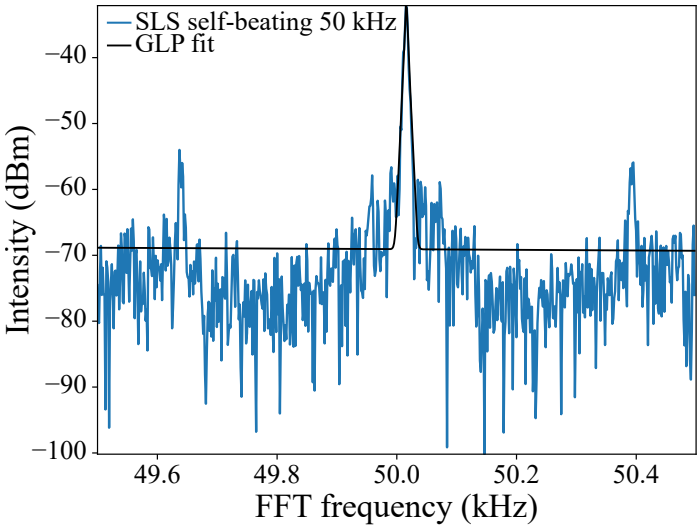

Figure 4.6: Ultra-stable laser linewidth measurement. This data is the beat frequency spectrum taken from the FFT of the DSO9254A oscilloscope.

2.6 kHz threshold, we can be confident that the laser is coherent along a 25 km fibre length, meaning we can set the upper bound of 2.6 kHz on the linewidth for this laser system. This is a factor of $\sim 10^3$ reduction in linewidth from the unlocked DL100. Although this is larger than the expected minimum CPT linewidth, it will not prove to be the limit of CPT linewidths we measure in this thesis.

4.2 Experimental Techniques

The experiments in this work centre around three main types of measurements: photoluminescence spectroscopy, photoluminescence excitation spectroscopy, and optically-detected magnetic resonance measurements.

4.2.1 Photoluminescence Spectroscopy

Photoluminescence (PL) spectroscopy is used to characterize the different spectral components of sample emission. To do so, a fixed frequency laser is used to excite the sample, which can be either resonant with some transition of interest or exciting above the bandgap. Above-bandgap excitation produces free excitons that bind to centres in the sample, leading to subsequent luminescence. The spectrum is measured on a spectrometer.

4.2.2 Photoluminescence Excitation Spectroscopy

In order to overcome the resolution limits of a spectrometer, one measurement method used is photoluminescence excitation (PLE) spectroscopy. Excitation spectroscopy is performed by sweeping a laser across an optical transition, while a photodiode or single-

photon detector records the change in emission intensity. PLE is distinct from PL as the emission intensity is measured as a function of the excitation frequency, rather than the emission frequency. The resolution of PLE is limited by the laser linewidth, which can be much better than what is available from the best spectrometers. As an example of a PLE measurement, the T-centre can be excited by sweeping a laser over its ZPL while the emission is filtered to only include the PSB so as to avoid sending the laser to the detector.

Hole-Burning and Multi-Colour PLE

There are a number of variations of PLE also used in this work that all function under the same principle of measuring the intensity of the emission relative to the change in excitation frequency. One such measurement is known as hole-burning. This involves fixing the frequency of one laser while sweeping another across that frequency. Hole-burning falls under a more broad term: two-colour PLE. As the name suggests, two-colour PLE involves two laser frequencies, which can either be swept together or independently (pump-probe). Two-colour PLE is useful for characterizing features of the sample that require two frequencies to be seen. In addition, more frequencies can be added to the sample excitation in multi-colour PLE, as long as the emission intensity is still being measured relative to at least one swept laser frequency.

4.2.3 Optically-Detected Magnetic Resonance

Finally, some features of the sample require probing transitions in the regime of radio frequencies (RF) or microwave (MW) frequencies. Optically-detected magnetic resonance (ODMR) is similar to PLE with its use of optical excitation and detection. However, the laser excitation remains at a fixed frequency while an additional RF or MW field is swept in frequency. Therefore the change in optical emission produced from the laser is measured as a function of the RF or MW field frequency.

4.3 Detection Methods

The apparatuses described in the following sections utilize several detection methods. The different methods of excitation require a range of measurement methods, be it a wavelength sensitive detection, or intensity measurements sensitive at the single-photon level. Here we describe the different detection methods used.

4.3.1 Fourier-Transform Infrared Spectroscopy

In order to measure photoluminescence (PL) spectra, we use a Fourier-transform infrared (FTIR) Michelson interferometer. The interferometer simultaneously measures all present frequencies by producing an interference pattern based on path length difference,

known as an interferogram, that is picked up by a detector. This interferogram can be converted to a spectrum with a Fourier transform.

This work uses a Bruker IFS 125HR FTIR spectrometer. The Bruker IFS 125HR has an absolute accuracy of 1 µeV (∼242 MHz), relative accuracy of 0.1 µeV (∼24.2 MHz), and minimum resolution of 0.25 µeV (∼60 MHz). We use a liquid nitrogen cooled Ge diode detector due to its high sensitivity in the NIR range.

4.3.2 Photodiode with Lock-in Amplification

For PLE measurements, we perform lock-in amplification in order to amplify our signal relative to background noise. We use an Ametek 5210 Dual-Phase Analog Lock-in Amplifier for our signal processing. The Ametek 5210 can handle frequency responses over a range of 0.5 Hz to 120 kHz. For this work we use the square pulse setting. The voltage sensitivity ranges from 100 nV to 3 V, and the integration time can be set from 1 ms up to 3 s. Typically, we record data with a 1 V scale and integration time of 0.1-1 s. In addition, a high-gain amplifier is used on the lock-in signal, which is kept at the highest possible setting that does not overload the lock-in amplifier in order to lessen the impact of spikes caused by cosmic rays.

4.3.3 Single-Photon Detection

Single-photon counting in this work was only used for characterization of the laser pulse shape. In order to get time-resolved photon counts on very short time scales (picosecond up to microsecond scales), we use an avalanche photodiode (APD) and a time tagger that counts the photons measured in separated time bins.

We use the ID230 APD from ID Quantique, which has a low-temperature InGaAs/InP sensor. The ID230 is operational from 900-1700 nm with a quantum efficiency that can be set up to 25% for 1550 nm (slightly higher at 1326 nm). Signal attenuation was necessary to not over saturate the ID230. With the sensor at its typical set temperature of -90 °C, the dark count rate is rated at 50 Hz (200 Hz) for a 10% (20%) quantum efficiency. The deadtime between detection and the next available detection window can be set between 1 µs to 100 µs. An SMA output sends low-voltage transistor-transistor logic (LVTTL) pulses with 100 ns width to be counted.

For photon counting, we use the Swabian Instruments Time Tagger Ultra. This time tagger allows for precise time binning of counts from TTL pulses with a resolution of 1 ps, maximum data transfer of $70 \cdot 10^6$ tags/s, and dead time of 2.1 ns.

4.4 Samples

The two samples used in this work are referred to as '*Phoenix*' and '*Chai*.' These samples are the two best ^{28}Si T-centre samples in our possession in terms of strong emission

and narrow linewidths. Both samples were cut from an isotopically purified ^{28}Si crystal produced for the Avogadro project [8], which are enriched to 99.995% ^{28}Si.

Phoenix was originally prepared for G centre studies, but was repurposed as a T-centre sample. The initial treatment involved irradiation at 320 kGy with 10 MeV electrons followed by a 17 hour anneal at 100 °C in boiling water. Following this, *Phoenix* was annealed in steps of 50 °C from 350 °C to 450 °C in air on a hotplate, spending around 30 minutes at each temperature. Finally, *Phoenix* went through polishing and a short HF/HNO_3 etch in order to limit laser scatter off of the surface and to reduce surface strain.

Chai is a similar ^{28}Si sample that went through the same annealing process, except for a slight variation in the hotplate anneal, in which it was held in hydrogen gas and went to a maximum temperature of 440 °C. The other notable difference between *Phoenix* and *Chai* is their carbon concentrations of $< 5 \cdot 10^{14}$ cm^{-3} and $\sim 1.5 \cdot 10^{15}$ cm^{-3} respectively.

4.5 Magnetic Field Apparatuses

To hold our samples in an adjustable magnetic field, we created two apparatuses designed to meet the needs of the different experiments in this work. The first system provides a static $\sim$100 mT field at which the electron and hole spin optical transitions resolve in ^{28}Si [10]. The sample mount provides coarse rotational tuning, allowing for spectral isolation of T-centre orientations. These features are necessary for the optical Rabi experiment in §5.3.

The coarse tuning of the magnetic field orientation, lack of variable field strength, and lack of RF control prove insufficent for measurements of the T-centre hyperfine and optical CPT. These experiments do not require fields up to 100 mT, so we created a second magnetic field apparatus with a variable magnetic field up to 2 mT with higher precision control and an RF line.

4.5.1 Static Magnetic Field Rotation Apparatus

The first apparatus is a rotation sample mount held between two disk magnets. A sample is held in a brass mount by a window that is AR coated for the O-band, with a larger cylindrical brass frame housing the mount. This frame slots into a larger brass block that holds two disk magnets apart with a separation of 0.9" (see Fig. 4.7). In order to view the sample in its suspended orientation, a 45° mirror is placed in its own cylindrical frame such that a laser in the plane of the table is able to reflect up into the sample and the emission can reflect back out. The height of the mirror frame is adjusted such that when the sample frame is rested on it, the sample is centered within the magnetic field, minimizing field inhomogeneities across the sample.

Field simulations on the K&J Magnetics website for these magnets estimate a field inhomogeneity between 1.1-5.5 mT about a 110.8 ± 0.4 mT field for a volume of radius 5 mm.

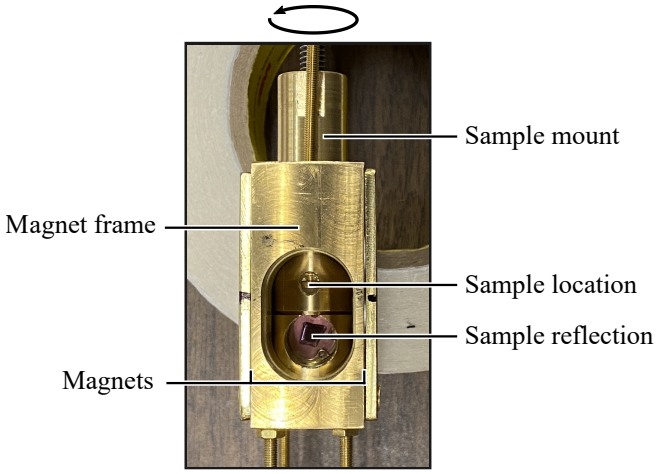

Figure 4.7: Static magnetic field rotation apparatus. The sample can be seen through the reflection off of a 45° mirror as it is suspended in the rotation mount. The magnets are housed under the brass plates on either side of the magnet frame.

We anticipate a 3.109 GHz electron spin splitting at this field. We estimate a spectral shift between 300 kHz and 3 MHz across the sample based on the inhomogeneity and depending on sample placement. The accuracy and precision of the sample rotation angle was found to only be within several degrees as the brass cylinder that houses the sample often sticks to the magnet frame.

This mount is placed in a Cryo Industries model 100N-3859-VT0 varitemp dewar. The cylindrical sample frame is connected to a sample rod which is accessible from the outside of the dewar, meaning that the sample can be rotated while submerged in liquid helium. Using liquid helium, the sample chamber is able to reach 4.2 K at atmospheric pressure, but we often operate at 1.4 K by pumping on the chamber with a Stokes pump. Through the use of pressure regulation we can tune anywhere between 1.4 K and 4.2 K. The Cryo Industries dewar has four windows around the sample chamber, but for this setup only the one facing the detection path optics is used.

4.5.2 Variable Magnetic Field Apparatus

In order to provide better field homogeneity, field precision, and a tunable RF signal, we developed a setup based around a three-axis Helmholtz coil array and an RF coil wrapped around the sample. The RF coil resonantly drives the spin state transitions, while the Helmholtz coil array provides a tunable magnetic field up to 2 mT.

The sample is seated in a delrin mount, held in place by a wire wrapped around 3 times (see Fig. 4.8). This wire is used to produce an RF field through the sample. Unlike the previous apparatus, the sample sits with a fixed orientation relative to laser excitation and surrounding environment. This sample mount is attached to the end of a sample rod within a Janis model SVT-200 varitemp dewar. Functionally, the Janis dewar has the

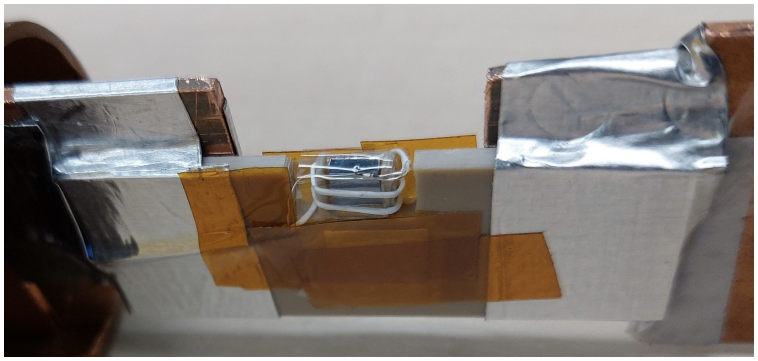

Figure 4.8: Image of *Chai* mounted in the RF coil.

same temperature control capabilities as the Cryo Industries dewar, but has a smaller bore hole for the sample chamber. In practice the sample chamber of the Janis dewar has a slightly higher minimum temperature due to differences in vacuum seal quality and radiation shielding about the sample rod. The Janis dewar can be operated in the range 1.5-4.2 K.

A three-pair Helmholtz coil array surrounds the sample chamber. By individually addressing the current in each pair, it is possible to generate a magnetic field in any direction. The Helmholtz array we use is the Ferronato BH300-3-A. Each coil pair is rated for 500 µT/A (or 5 Gauss/A) with a maximum field of 2 mT. Field homogeneity is rated to have differences smaller than $\pm 1\%$ ($\pm 5\%$) for a volume out to 35 mm (50 mm) from the center. For reference, the dimensions of *Chai* are 1.9 mm $\times$ 4.2 mm $\times$ 5.4 mm. While not strictly measured, the estimated difference for a 5 mm displacement from the center is $\pm 0.01\%$ – $\pm 0.05\%$.

Chapter 5

Optical Rabi Oscillations

The first step we take towards optical controlis driving optical Rabi oscillations. Building up to the first observation of optical Rabi oscillations, we characterize the magnetic field of the apparatus from §4.5.1. The resulting Rabi oscillations demonstrated in this chapter illustrate the limits of optically-driving T-centre ensembles, but highlight the potential for coherent driving of the T-centre's optical transitions.

5.1 Optical Rabi Measurement Method

Our experiment utilizes the static magnetic field rotation apparatus described in §4.5.1. For resonant excitation of the sample, the two ultra-stable laser channels are each sent into free space from their own collimators (see Fig 5.1). These collimators produce 8 mm beams with fairly uniform intensity in order to homogeneously illuminate *Phoenix*. It is possible to individually address them for polarization, chopping, or additional amplification. Both paths include a 1326 nm bandpass (BP) filter to remove broadband spontaneous emission due to the optical amplifiers. Each beam was aligned to the sample as shown in Figure 5.1. This nearly collinear alignment was chosen over combining through a beamsplitter in order to preserve laser power.

Sample emission is collimated using a parabolic mirror and directed to the input window of the Bruker FTIR spectrometer using a second mirror. The emission is filtered for PLE using a combination of two 1319 nm longpass (LP) filters and a 1375 ± 50 nm BP filter. The 1375 nm BP selects a specific range of the T-centre PSB, while filtering out the silicon Raman line at 1426 nm, which produces a constant background signal and can dominate the PSB emission. The Ge diode detects the signal after filtering.

We record PLE signal using lock-in amplification. The Ge diode detector puts out a DC signal that can be recorded, but, by chopping the optical excitation, the resulting modulated signal can be sent through a lock-in amplifier in order to cancel out sources of noise.

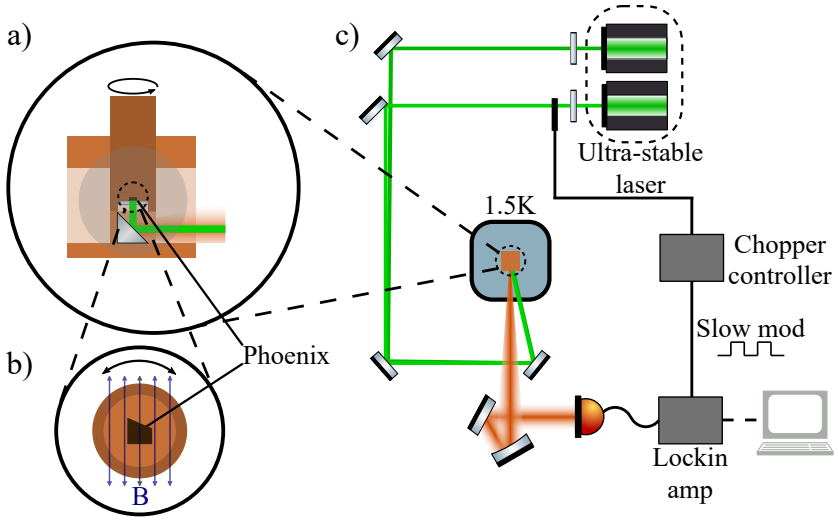

Figure 5.1: Diagram of the optical Rabi setup. a) The design of the sample mount housed within the magnet mount from a side view. Here the closer magnet is represented by the faint circle, while the second is on the backside of the mount such that the field points along the axis going in and out of the page. b) *Phoenix* as it is held in the sample mount looking from below. c) The two lasers are aligned from separate collimators to be nearly collinear using the top two mirrors. The collection optics send the signal to the Bruker FTIR spectrometer Ge diode.

5.2 Magnetic Field Characterization

The T-centre was previously characterized by Bergeron et al. [10] at various field strengths for a set field orientation that optically resolved 11 orientation subsets. However, it was not yet observed how these subsets split depending on the magnetic field direction. In order to perform an optical control scheme it is important that all of the T-centres being excited experience the same drive strength. One problem that could arise is having transitions from two T-centre orientations partially overlap spectrally, leading to a mixed signal from each with different Rabi frequencies. We characterize the magnetic field of our static field apparatus in order to select a spectrally isolated orientation subset.

5.2.1 Strong Subset Identification

Rotating *Phoenix* in a plane within the static external magnetic field should allow us to select a strong subset for driving optical Rabi oscillations. The Zeeman splitting, given by the equation

$$\Delta f = \frac{g_e \mu_0}{\hbar} B\,, \tag{5.2.1}$$

gives an electron spin splitting of 3.109 GHz for the estimated 110.8 mT field and $g_e = 2.005$ [10]. Since g_h varies based on orientation, we are able to optically select different orientations with the different Zeeman splittings in the excited state.

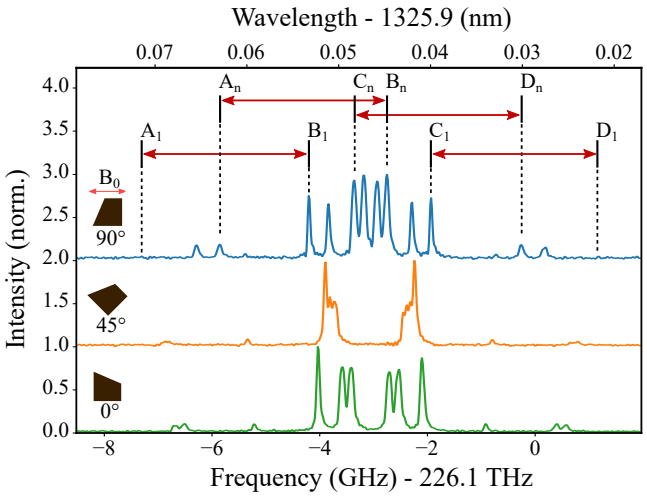

Figure 5.2: T-centre magneto PL measurements showing different transitions for the various subsets of orientations. The sample is rotated relative to the ∼110 mT field. The ABCD transitions for two orientation subsets studied with the +90° magnetic field orientation are labelled. Not all transitions are bright enough to be seen in PL. (inset) Sample orientations relative to the magnetic field.

We began by measuring the PL spectra of *Phoenix*. We aligned a 1047 nm laser in the beam path to provide above-band excitation and the signal was read using FTIR spectroscopy. For PL measurements it is only necessary to filter out the 1047 nm laser, for which we use a 1064 nm longpass filter. PL spectra for three magnetic field orientations are shown in Figure 5.2, and the electron spin splitting can be matched for some sets of visible peaks. Seeing as 12 orientations are not uniquely distinguishable, we must have multiple T-centre orientations within the visible subsets.

The sample orientation labelled +90° in Figure 5.2 is believed to be similar to the configuration in Ref. [10] given the pattern of transitions. We decided to pursue two different subsets in the 90° configuration. These two subsets are labelled 1 and n under the assumption that orientation 1 matches the similarly numbered orientation in Bergeron et al. [10]. The A, B, C, and D transitions for these two subsets are labelled in Figure 5.2, which follow the naming convention we set in Figure 2.1.

5.2.2 Optical Linewidth Characterization And Observation of g_e Anisotropy

With the rotation mount fixed in the +90° position, the setup was adjusted to conduct two-colour PLE with the lock-in amplifier in order to probe the resonant spectral properties relevant to optical Rabi oscillations. Two-colour excitation is necessary at this field as pumping from a single electron spin state will result in polarizing the electron spin into the undriven spin state.

We use two methods of two-colour scans. First, we sweep the two frequencies in tandem with a fixed frequency separation. By setting the separation to the electron spin split-

ting, we probe the inhomogeneous distributions of different orientation subsets. Focusing on the two laser sweep in Figure 5.3a, we see that the two colour resonance of the A_n/B_n lines partially resolves two orientation subsets. The corresponding g_h for these subsets most closely resemble the measured values for orientation 8 and 9 by Bergeron et al. [10]. The inhomogeneous linewidths we get from these two constituents are 54.2(1) MHz and 52.3(2) MHz for A_8/B_8 and A_9/B_9 respectively with a splitting of 43.66(4) MHz. These two subsets produce the largest resonant signal of the surrounding subsets, though they do overlap. We choose A_8/B_8 for optical Rabi oscillations due to the strong signal. Figure 5.3b shows the A_1/B_1 subset, which has an inhomogeneous linewidth of 32.6(1) MHz.

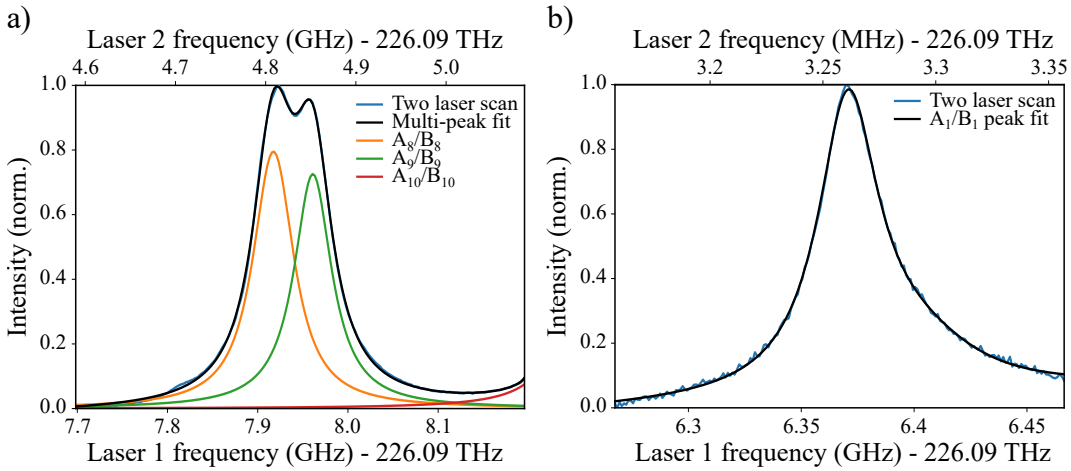

Figure 5.3: a) PLE two-laser scan over the A_n/B_n resonance, revealing the A_8/B_8 and A_9/B_9 orientation subsets which were not resolved in the PL measurement. b) PLE two-laser scan over the A_1/B_1 resonance.

Second, we perform a pump-probe measurement to measure the instantaneous homogeneous linewidth for a given subset of T-centres. In Figure 5.4, both the A_8/B_8 and A_1/B_1 transitions were driven such that the pump was centered on the A transition and the probe laser swept across B. The electron spin splitting for each subset is 3.106(2) GHz and 3.1097(7) GHz for the 8 and 1 subsets respectively. These splittings correspond to g-factors of 2.0052(4) and 2.002(1) with our magnetic field of 110.8 mT. This anisotropy is significant, but smaller than the uncertainty in g_e reported by Bergeron et al. [10] and is much smaller than the anisotropy in g_h, which matches the model of a strongly localized electron and loosely bound hole. The low-power homogeneous linewidths are 12.9(2) MHz and 10.1(1) MHz for A_8/B_8 and A_1/B_1 respectively in the low power limit.

The homogeneous linewidths we measured are significantly higher than the 0.69(1) MHz zero-field holeburning linewidth from another measurement carried out during the course of this project [21]. A likely culprit is increased sample temperature brought about by the sample mount. Since the sample is held in the brass mount by a window, it is unlikely that *Phoenix* is in direct contact with the surrounding liquid helium in the dewar. In addition,

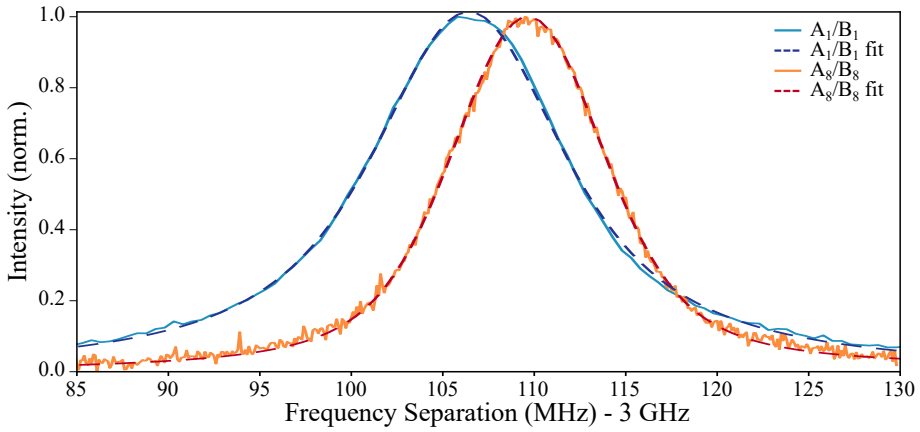

Figure 5.4: Pump-probe PLE measurement of the A_8/B_8 and A_1/B_1 orientations. Two different electron spin splittings are observed: 3.106(2) GHz and 3.1097(7) GHz.

due to the downward facing mount, it is possible that a small bubble can form on the window. A 10.1(1) MHz linewidth corresponds to a temperature of ∼2.46 K from Eq. 2.1.1 [10].

Based on our simulations, we expect to see optical CPT for a homogeneous ensemble under these conditions. In performing these pump-probe measurements for the electron spin, there is no sign of optical CPT, which would lend credence to the existence of inhomogeneities across the sample. The estimated field inhomogeneity from §4.5.1 is between 300 kHz and 3 MHz. Nearby ferromagnetic materials may introduce additional inhomogeneity, but their distance from the sample should make this effect negligible. A 0.3–3 MHz electron spin splitting inhomogeneity would wash out the expected narrow CPT response. In addition, the two frequency splittings that lead to CPT are dependent on the anisotropic hyperfine. Lack of precision in orienting the sample will likely lead to the different orientations composing the observed subsets to split slightly from each other, further washing out CPT. This result demonstrates the importance of field homogeneity and alignment for measuring CPT.

5.2.3 Attempt to Optically Resolve Hyperfine Structure

This apparatus failed to achieve optical linewidths sufficient to resolve the ground state hyperfine structure. Figure 5.5 shows the results of four-colour hole burning for two different orientation subsets. This apparatus is still sufficient to measure optical Rabi oscillations despite the linewidth being larger than in the simulations in §3.3.1.

5.3 Optical Transition Rabi Oscillations

Having characterized our magnetic field and chosen a strong T-centre orientation subset (A_8/B_8), we now attempt optically-driven Rabi oscillations. A Toptica BoosTA pro

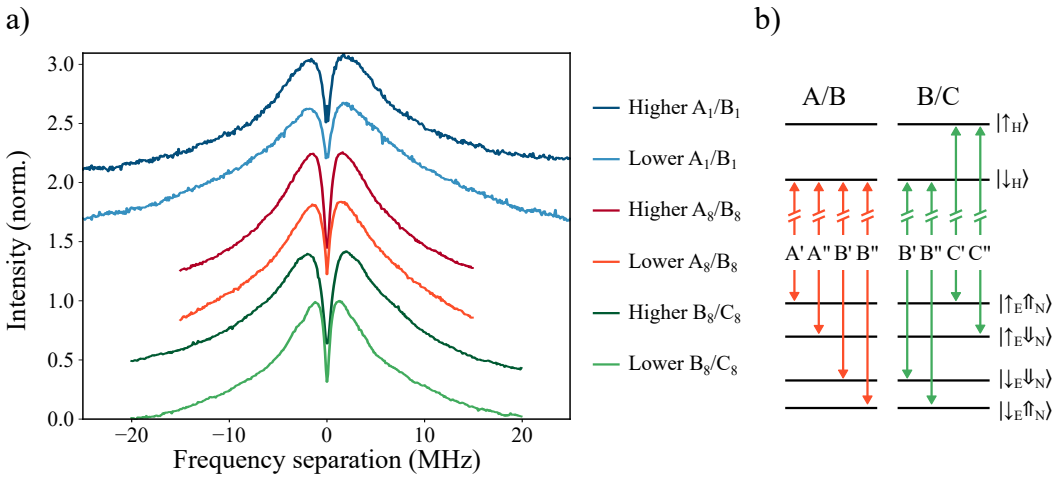

Figure 5.5: Four-colour PLE pump-probe. a) Attempt at nuclear spin readout by performing nuclear spin hole burning at field. Three different sets of transitions were tested, with hole burning performed on both the $|\uparrow_E\rangle$ and $|\downarrow_E\rangle$ sets of nuclear spin states. b) Level diagram with the four driven transitions for the A/B and B/C configurations. We denote the transitions with $|\Downarrow_N\rangle$ and $|\Uparrow_N\rangle$ with ′ and ". Scans labelled 'higher' have one of the laser frequencies on the higher frequency transition of A/B or B/C swept, while scans labelled 'lower' sweep a laser on the lower frequency transition.

replaces one of the collimators in the setup from Figure 5.1. The BoosTA pro is a high-powered tapered laser amplifier, which can output a signal up to 1 W. The beam profile from this amplifier is noticeably less uniform than that of the beams from the collimators. This boosted channel is used for pulsed excitation of the T-centre at field. The un-boosted laser frequency is used as a weak re-pump that is left on at all times. The re-pump laser is chopped for use with the lock-in measurement. The PL spectra in Figure 5.2 suggests that the B and C transitions have stronger dipoles than the A and D transitions based off of the relative intensities. Therefore we address the B transition with the pulsed laser in order to drive Rabi oscillations on the stronger B transition.

We start by characterizing our optical pulse shape at durations between 1 ns and 500 ns. A collimator was set up to collect the scattered light coming off of an iris in the pulsed laser path. With some neutral density (ND) filters placed in between to cut the intensity, the laser signal was sent through fibre to the ID230 for single-photon detection. Histograms of time-binned counts are shown in Figure 5.6. There is a small hump at the beginning of the pulse from the pulsed amplifier. This hump is accentuated or diminished depending on the boosted output power.

In order to account for the difference in pulse shape from an ideal square pulse, we measure the integrated power from these different powered pulses as they vary in length. We use a power meter equipped with a Thorlabs S132C Ge diode sensor, giving the time averaged power of the laser. The integrated power readings for the various amplification settings are shown in Figure 5.7.

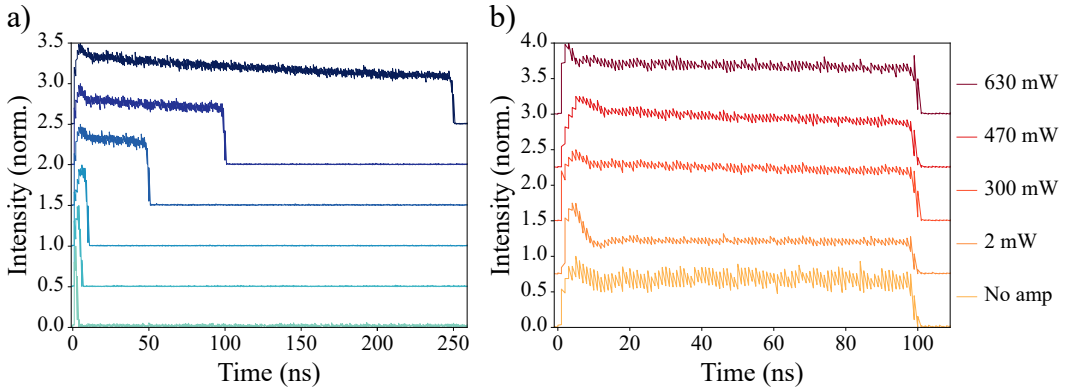

Figure 5.6: Pulse shape of the laser for different a) pulse lengths and b) amplification. The amplified powers correspond to the output power from the BoosTA pro amplifier, while the non-amplified signal comes directly from the Aerodiode pulsed amplifier.

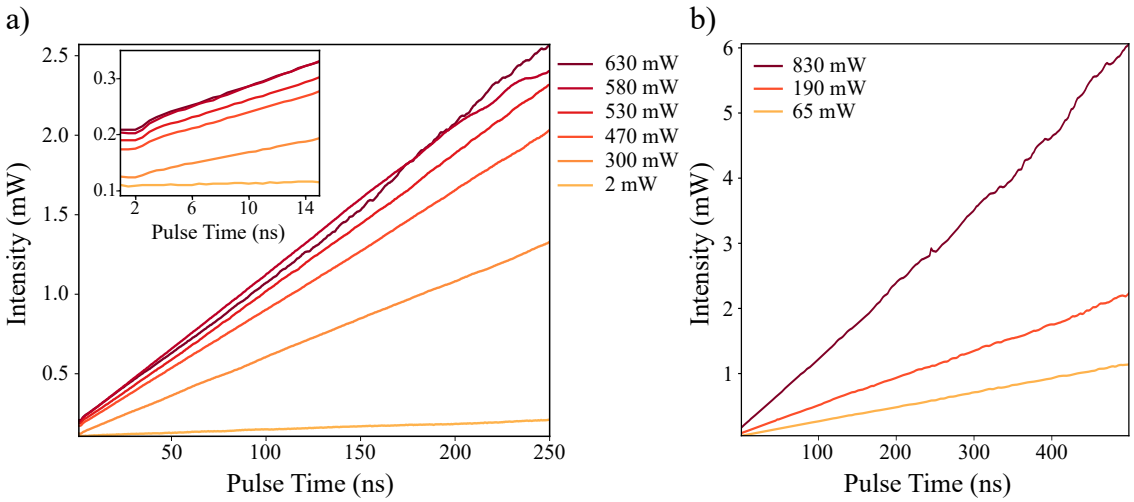

Figure 5.7: Integrated laser power per pulse length for a) characterization powers and b) optical Rabi powers. (inset) The shorter pulse times shows that the minimum pulse length is approximately 2.5 ns.

5.3.1 Rabi Oscillations

We measure the combined signal of the fluorescence during the pulse and the decay fluorescence

$$S(\tau) = \Gamma \int_0^\tau \rho_{22}(t)dt + \rho_{22}(\tau)\,, \tag{5.3.1}$$

where $\rho_{22}(t)$ is the excited state population at time t and τ is the pulse length. The detected signal, illustrated in Figure 5.8, comprises the integrated emission (red) produced during the laser pulse (black) and the fluorescence decay (blue). In order to not cut off a significant portion of the decay and to allow for ample time to re-initialize the state back into the proper state, the repetition rate for the pulse was set to 5 µs $> 1/\Gamma$.

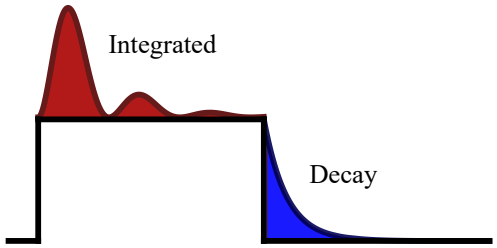

Figure 5.8: Components of the integrated optical Rabi oscillation signal.

The measured signals can be seen in Figure 5.9 along with the bare Rabi oscillations as determined from the fit. The data was fit using the three-level model from §3.4 and Eq. 5.3.1. The steady-state excited state population will be considerably smaller than 0.5, because we have a three-level system with a weak re-pump. Oscillations of $7(2)$, $5(4)$, and $4(4)$ MHz were fit for laser powers of 0.83(2), 0.19(2), and 0.07(2) W. These Rabi oscillations correspond to π-pulse times of 67 ns, 104 ns, and 147 ns. Following the same order, the dephasing rates of these fits were 12.7(1), 9.35(9), and 8.28(9) MHz. These dephasing rates do not precisely match our observed homogeneous linewidth (12.9(2) MHz). The rate of dephasing increases with power, indicating heating due to the laser. In Figure 5.9b we consider how the Rabi oscillations would appear with $0.69(1)$ MHz dephasing.

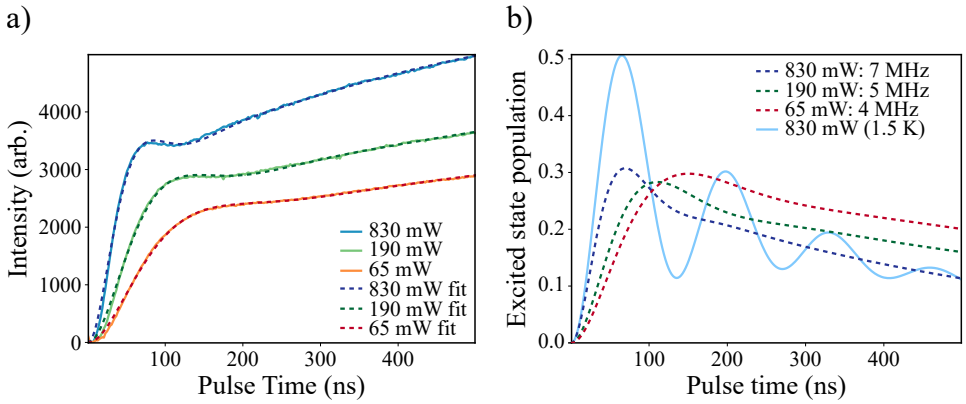

Figure 5.9: Optical Rabi oscillations. a) Measured fluorescence fit to the three-level model of the T-centre. b) The Rabi oscillations as determined by the fit. The solid line is predicted performance at 830 mW and 1.5 K from Ref. [21].

The Rabi frequencies we report are significantly lower than what we estimate from §3.2 given our laser powers. Even at the 3% lower bound on the radiative efficiency and accounting for the 70% transmission into silicon, we would expect to see Rabi frequencies of 11.8 MHz for our highest power based on Eq. 3.2.1. This discrepancy in Rabi frequency corresponds to the T-centres only receiving 39% of the laser power. In Figure 5.10 we fit a Rabi frequency power dependence of 8(2) MHz/W$^{1/2}$, which is smaller than the 13 MHz/W$^{1/2}$ we estimated based on $\eta_R = 0.03$. There are a number of challenges with exciting a bulk sample that could be at play here.

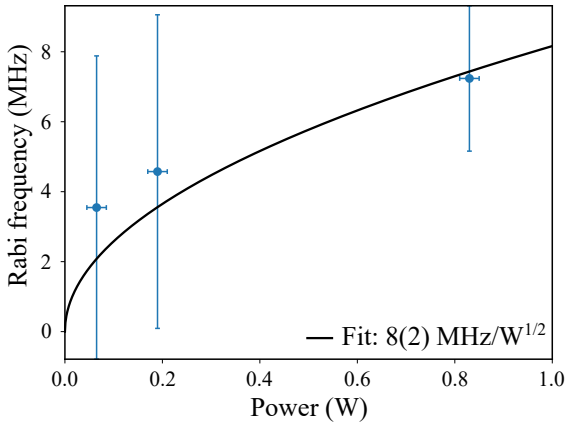

Figure 5.10: Rabi frequency as a function of laser power.

In a bulk sample, centres detuned within the homogeneous linewidth will be driven. The detuned centres will be driven more weakly, smearing out the apparent oscillations. The A_9/B_9 orientation contributes $\sim 23.5\%$ of the signal at the peak of the A_8/B_8 resonance in Figure 5.3. This contribution washes out the Rabi oscillations and lowers the observed Rabi frequency. There are also internal reflections and reflections off of the brass sample mount, causing non-uniformity across the sample.

We attempted to drive Rabi oscillations on more isolated orientations, but only observed weaker responses similar to the data reported for 70 mW. In all cases we used HWPs in each beam path in order to maximize the coupling strength through laser polarization. It it likely that our polarization is still not perfectly matched to the dipole for the transition.

In conclusion, we have demonstrated optical Rabi oscillations with frequencies as high as $7(2)$ MHz. The apparatus we built to perform these measurements failed to achieve the cooling we expected, which led to much less distinct oscillations. We showed that with adequate cooling multiple oscillations should be visible. Observed Rabi frequencies suggest that non-radiative decay paths exist for the T-centre. An apparatus capable of addressing single T-centres at 1.5 K will allow for improved measurements of optical Rabi oscillations through the removal of inhomogeneous effects. In addition, we measured an anisotropy in g_e not previously detected. Since the apparatus used in this chapter was not adequate for optical measurements of hyperfine structure and CPT, we developed a new apparatus to produce the results in the following chapters.

Chapter 6

Optically Detected Magnetic Resonance of the Hyperfine Structure

In this chapter we characterize the hyperfine structure of the T-centre ground state. By measuring the ground-state splittings from zero field up through the intermediate field regime for different magnetic field directions, we can understand the anisotropic hyperfine coupling that splits the T-centre orientations.

The measurements in this chapter are all optically-detected magnetic resonance (ODMR) spectra performed on the variable magnetic field apparatus in §4.5.2. We fix the ultra-stable laser frequency to the centre of the inhomogeneous distribution, while sweeping the RF signal across the splittings between T-centre ground states. When the RF signal comes into resonance with one of these splittings, the signal increases due to a reduction in hyperpolarization. All of the analysis of the hyperfine tensor based off of these ODMR measurements was performed by my colleague Joshua Kanaganayagam and is detailed in his thesis [34].

6.1 ODMR Measurement Method

In this chapter we measure the ground-state structure by ODMR with the ^{28}Si sample *Chai*, in the tunable magnetic fields apparatus from §4.5.2. The sample is wrapped with a copper wire coil 'RF antenna' that carries the RF drive to produce the ODMR signal. To provide the RF signal to the sample coil, we use the same SRS SG386 signal generators that were used in the tuning of the ultra-stable laser. The frequency stability of $< 10^{-11}$ 1 second Allan variance is more than sufficient to resolve the smallest typical hyperfine splittings ($\sim$ 0.1 MHz). A Keysight EDU36311A multi-channel power supply provided the currents to all three pairs of Helmholtz coils. The Keysight has a rated current noise and ripple of < 4 mA.

Only one channel from the ultra-stable laser is necessary for optical readout. The collimated beam is filtered using a 1326 nm BP filter to remove any background, includ-

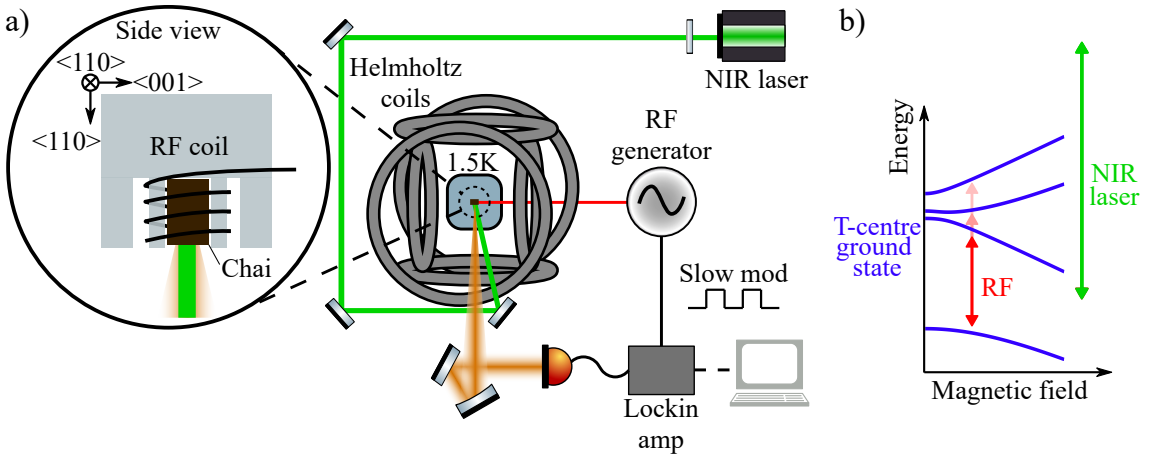

Figure 6.1: a) Diagram of the variable magnetic field setup used for ODMR. Three pairs of Helmholtz coils surround the cryostat centred on the sample. The RF generator sends the signal to an antenna coil around the sample. The close-up shows *Chai* held in the sample mount by the wiring of the RF coil. b) Energy level diagram of ODMR. The laser is fixed at the centre of the inhomogeneous distribution while the RF field is swept in frequency.

ing spontaneous emission from the optical amplifiers. Figure 6.1 shows how the beam is aligned to the sample.

Fluorescence is detected using a Ge diode detector. We perform a lock-in measurement of the optical signal by modulating the RF drive at 193 Hz. With this method we achieve high SNR with an ODMR background close to zero.

6.2 Zero-Field Level Structure

Figure 6.2 shows the results of performing an RF power study under Earth's magnetic field. Starting at an RF power of 6 dBm and ramping down to -30 dBm, we see in Figure 6.2 that, in the region of the previously measured anti-hole splitting of 3.85 MHz [21], there are 3 peaks that resolve into several resonances. This shows us that there is both sufficient drive strength from the RF coils to power broaden these resonances and Earth's field is strong enough to resolve the ground state structure of different orientations.

We next tuned the current in the coils to cancel out the Earth's magnetic field. In order to determine the zero field point for the sample, we monitored the ODMR spectra as the field was adjusted, using the T-centres as our magnetometer. While the exact zero field level structure was unknown, the different T-centre orientations should all be degenerate at zero field. Once the different resonances we see with Earth's field collapse down to a minimum number of lines, the Helmholtz coils should have canceled out all external magnetic fields to within the precision of the ODMR linewidths.

A comparison of ODMR between Earth's field and zero field is given in Figure 6.3a. At zero field we get three resonances near the expected 3.85 MHz transition, meaning

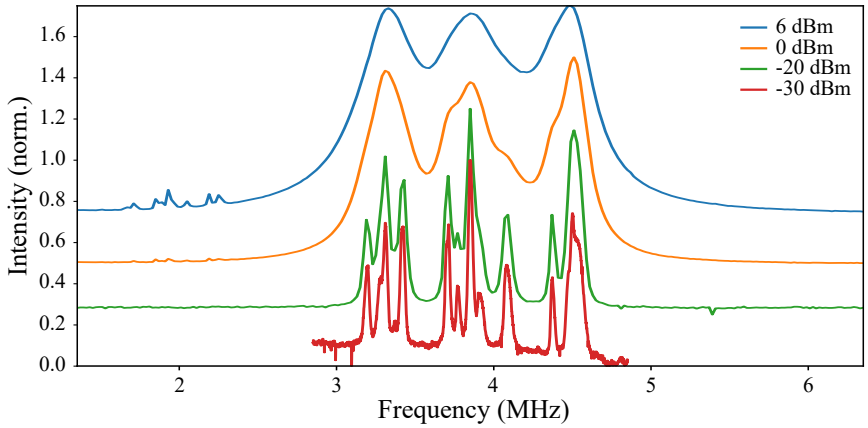

Figure 6.2: RF power study on the T-centre hyperfine splittings under Earth's magnetic field. The different orientation-related lines for each of the three ground state level splittings in the 3-5 MHz range become better resolved as the RF was turned down from 6 dBm to -30 dBm.

that the triplet state is not degenerate at zero field as it is for an isotropic hyperfine coupling, such as hydrogen. While not degenerate at zero field, we shall refer to the three higher energy states from the symmetry-broken triplet as a 'triplet' for simplicity. The three singlet-triplet resonances occur at 3.482(3) MHz, 3.713(4) MHz, and 4.268(3) MHz. The three triplet-triplet transitions are shown in Figure 6.3b, and at zero field they occur at 220(29) kHz, 551(7) kHz, and 785(6) kHz, equalling the differences between the three singlet-triplet frequency resonances. When optically pumping on one of the triplet states $|T_n\rangle$ at zero field, more population will hyperpolarize to the singlet state $|S\rangle$ than one of the other $|T_n\rangle$ due to the greater overlap of the optical transitions from $|T_n\rangle$. Therefore, the ODMR signal produced by a $|T_n\rangle$-$|T_m\rangle$ resonance is small unless simultaneously driving one of the $|S\rangle$-$|T_m\rangle$ resonances. In Figure 6.3b the higher frequency resonances are driven while an additional RF drive sweeps the low frequency range. This measurement has, for the first time, revealed the zero-field ground state structure of the T-centre.

As seen in previous high-field measurements [10], certain combinations of drive frequencies produce coherent population trapping (CPT). Figure 6.3c shows the CPT seen on the 551 kHz line while driving the 3.71 MHz line. This CPT feature has a contrast of 95(3)% and linewidth of 5.6(2) kHz, suggesting that we are still power broadening beyond the electron decoherence limit ($\sim$500 Hz). Because the contrast is nearly 100%, we know that the magnetic field inhomogeneity across the sample is small enough to not cause significant differences in the CPT frequency relative to the linewidth from one T-centre to the next. We next track the behavior of the level splittings for a few field orientations in order to pin down the anisotropic hyperfine tensor.

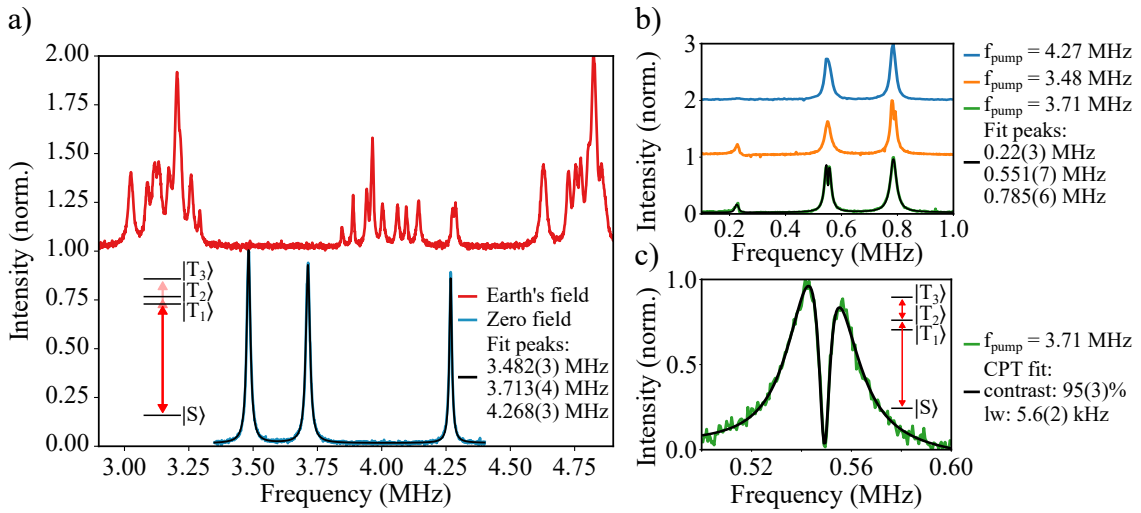

Figure 6.3: Zero-field T-centre hyperfine structure as measured through ODMR. a) The ODMR lines at zero field and Earth's field. These resonances represent the transitions from the singlet $|S\rangle$ to each of the triplet states $|T_n\rangle$. (inset) Ground-state level diagram from the RF resonances. b) Three additional low frequency resonances at zero field as seen while driving one of the higher frequency resonances. These resonances correspond to the splittings between $|T_n\rangle$. c) RF CPT seen on the 551(7) kHz line, when $f_{\text{pump}} = 3.71$ MHz. (inset) RF configuration for CPT.

6.3 Low-Field Level Structure

While the crystal axes of *Chai* are known relative to the cut surfaces of the sample, there is, in this apparatus, a slight misalignment between these surfaces and the axes of the Helmholtz coil pairs. In order to accurately orient the magnetic field relative to sample we will need to have a method of determining this misalignment. To do this we once again used the T-centre as our field sensor. This required knowing the orientational degeneracy along different symmetry axes of the T-centre. The monoclinic I symmetry of the T-centre informs us of the high symmetry axes [56]. A magnetic field aligned along the <001>, <111>, or <110> crystal axes produces two, three, or four distinguishable subsets. We start with magnetic fields near alignment with these axes, then tune the fields until there are the corresponding number of resonances for each of these field directions.

When aligning the <110> field orientation, we had a choice of direction as this orientation represents multiple directions. Before performing the full magnetic field spectrum, we roughly set the field along two orthogonal directions in the <110> plane, one axis in which the field is roughly perpendicular to the optical excitation, and one roughly parallel to the optical excitation. Figure 6.4 shows the corresponding ODMR spectra for the ~87.5 μT fields. Regardless of the orientation subset, the <110> field choices alter which resonances produce the most signal. This is likely due to transition polarization. The field perpendicular to the optical excitation was chosen for the <110> field study.

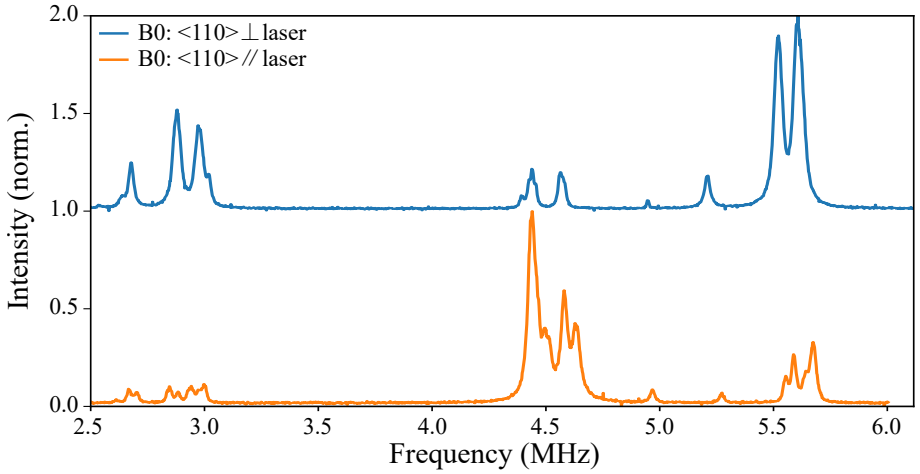

Figure 6.4: Comparison of the perpendicular and parallel <110> magnetic field hyperfine interaction ODMR data. This data was taken at a magnetic field of approximately 87.5 µT. The field for each orientation was not fully tuned to perfectly align or match in amplitude.

Figure 6.5 shows the ODMR spectra for each of the three magnetic field directions between 0 mT and 300 µT, along with curves fitting the hyperfine tensor provided by Joshua Kanaganayagam [34]. For this measurement, we did not track the lower frequency resonances below 75µT due to weak signal. However, once we pass 100 µT some of these components begin to increase in intensity and frequency. One of these low frequency resonances per orientation subset crosses over a high frequency resonance, which represents the transition from the low-field singlet and triplet level structure to the high-field level structure with two doublets per electron spin. The different curve colors correspond to the different orientation subsets that can be seen for the different magnetic field orientations. We see in both the <110> and <111> cases one orientation appears to have an anti-crossing where the level splitting goes to approximately zero.

Beyond 300 µT the signal begins to drop off as the largest splitting surpasses the homogeneous linewidth and starts approaching the magnitude of the inhomogeneous linewidth. As the transitions resolve optically, a single optical field and a single RF field become insufficient to prevent hyperpolarization. This range of fields provides ample data for fitting a hyperfine tensor model. Within the 0–300 µT range, we capture the low and intermediate field behavior of the hyperfine structure.

The anisotropic hyperfine tensor was fit by Joshua Kanaganayagam [34], giving

$$A = \begin{bmatrix} -4.03\ \text{MHz} & 0 & 0 \\ 0 & -2.93\ \text{MHz} & 0 \\ 0 & 0 & 4.50\ \text{MHz} \end{bmatrix}. \tag{6.3.1}$$

In order to use this in relation to a known direction in the lab reference frame, a rotation onto a crystal axis will need to be applied to this matrix. The exact rotation depends on the

T-centre orientation within the crystal lattice, of which there are the 24 distinct orientations. The details of these rotations can be found in Joshua Kanaganayagam's thesis [34].

This ODMR data allowed a complete and unambiguous determination of the T-centre ground state structure. We now have the ability to predict the ground state energy levels for all magnetic fields and centre orientations. This novel information is crucial for modelling the T-centre spin-states, optical transitions, selection rules, and cyclicity, and allows us to proceed towards optical control over the ground state spins. In the next chapter we measure optical CPT as an important precursor to coherent optical control.

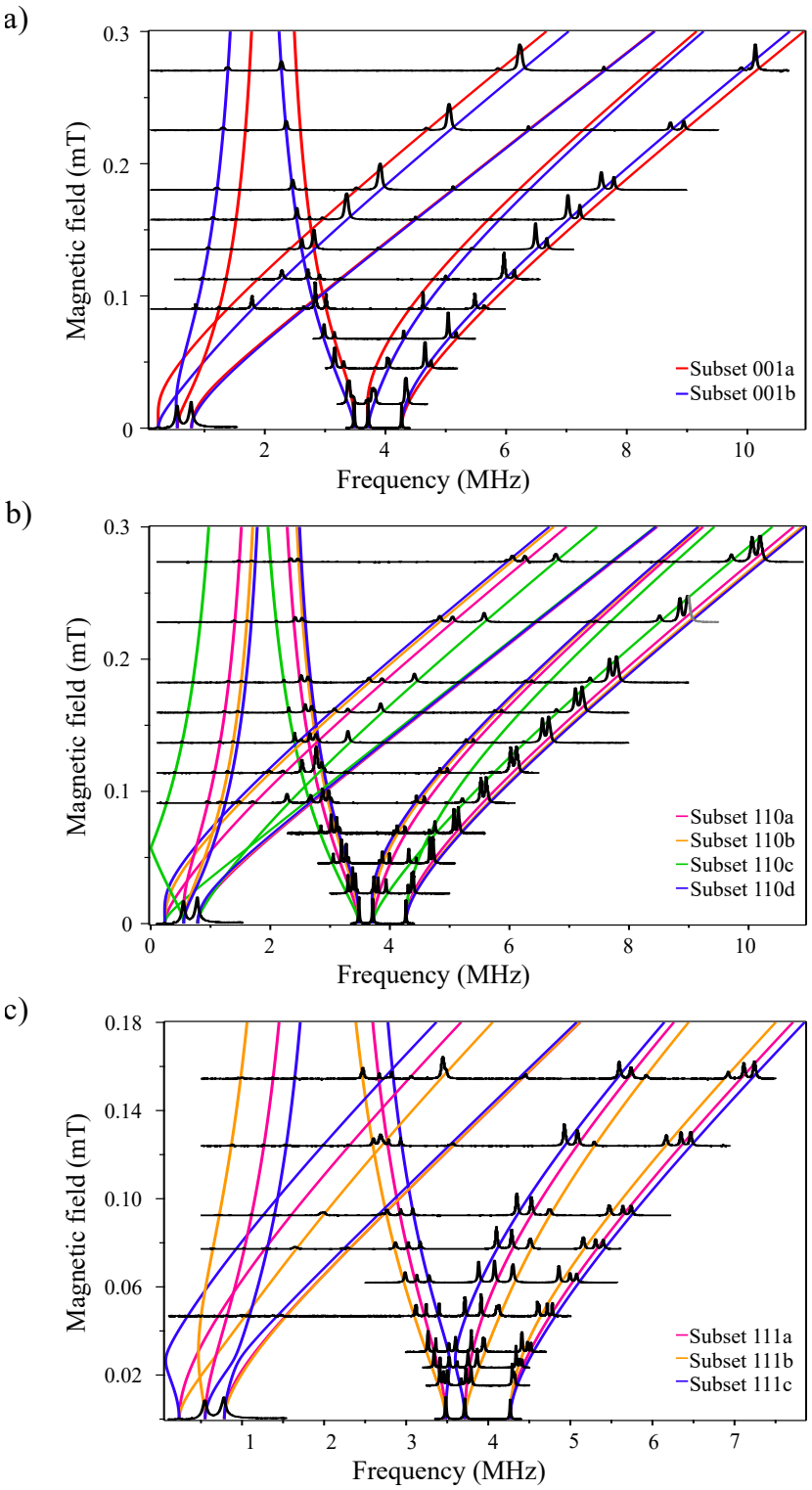

Figure 6.5: Energy level splittings as determined from the hyperfine tensor fit to the ODMR data [34]. The energy level splitting curves are plotted for the a) <001>, b) <110>, and c) <111> magnetic field orientations.

Chapter 7

Optical CPT

Having demonstrated optical Rabi oscillations and measured the hyperfine tensor of the T-centre, we now demonstrate, for the first time, optical coherent population trapping (CPT) with the T-centre. This is a pivotal first step towards optically controlling the spin qubits of the T-centre as it demonstrates the ability to coherently prepare a dark state of the ground-state spin. In order to alleviate the inhomogeneity in the initial measurements, we used same improved magnetic field apparatus that made possible the ground state hyperfine characterization in §6.

7.1 Optical CPT Measurement Method

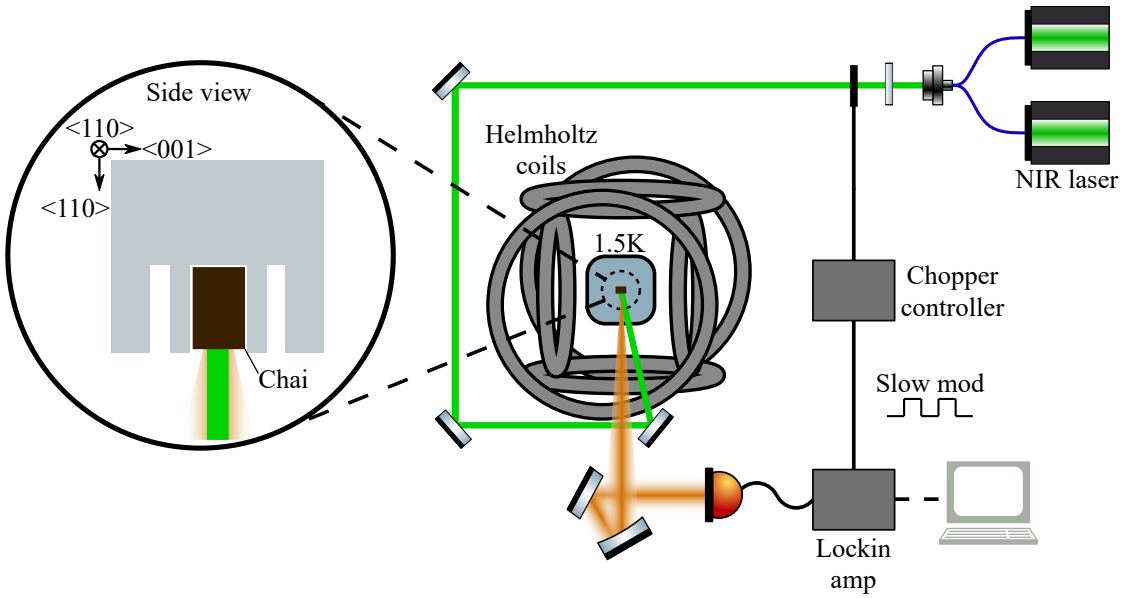

Figure 7.1: Diagram of the variable magnetic field setup as used for CPT. The Helmholtz array is shown around the cryostat holding the sample. A chopper modulates the laser excitation and provides a modulation signal used for lock-in measurements. The close-up shows a side view of the sample mount with the sample *Chai*.

We measure optical CPT using the experimental configuration shown in Figure 7.1. We began our measurements of optical CPT at the maximum 2 mT field of the Helmholtz coils in order to minimize the overlap between the optical transitions from the electron spin ground states. The Helmholtz coils require a current $I = 4$ A to produce a 2 mT field, which the Keysight EDU36311A used in §6 cannot supply. We also require minimal current noise, which translates to noise in the magnetic field, as this causes the CPT feature to move in time, leading to an increase in linewidth and decrease in visibility. We used the Rhode & Schwarz HMP4040.04 power supply to provide the 4 A current. In constant current mode the ripple and noise is rated at < 1 mA, which is a factor of 4 improvement over the Keysight EDU36311A current noise.

Once again the ultra-stable laser is used for optical excitation. Two channels are combined in-fibre using a 50:50 beam splitter and output into free space using a collimator. The collimated beam is filtered using a 1326 nm BP filter to remove any background spontaneous emission from the optical amplifiers. The lock-in modulation is generated through chopping of the collimated beam, meaning that both laser signals are chopped.

7.2 Observation of Optical CPT

We aligned the magnetic field along the <001> axis of the crystal lattice, which has two spectrally distinguishable subsets, as shown in §6. The HMP4040.04 1 mA minimum

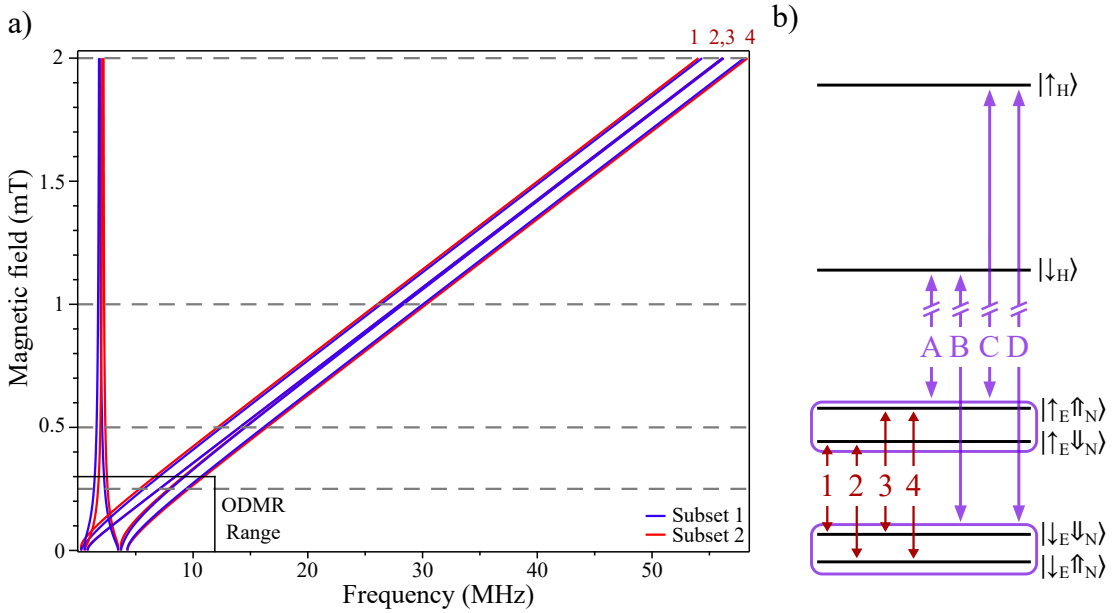

Figure 7.2: a) Ground-state splittings for a <001> magnetic field up to 2 mT based on the hyperfine tensor from §6 [34]. The gray dashed lines indicate the fields we use in §7.5. b) T-centre level diagram with the optical transitions A-D and ground-state splittings 1-4 involving opposite electron spins. We label the high-field electron, hole, and nuclear spin states for convenience, but the actual eigenstates vary with field.

step size corresponds to a $\sim 0.5\,\mu$T change in field, resulting in a maximum 15 kHz shift for a ground state splitting depending on orientation and field magnitude. Figure 7.2 shows the level splitting curves up to 2 mT [34]. We expect the major ground state splittings (1-4 in Fig. 7.2) to be between 50-60 MHz, with 2 and 3 being nearly degenerate. The roughly 55 MHz splitting between the electron spin states ensures that there is little to no overlap between the $|\uparrow_E\rangle$ and $|\downarrow_E\rangle$ ground states. The orientational separation in the ground state (red vs. blue in Fig. 7.2) is also expected to be much smaller than the optical linewidth of the transitions.

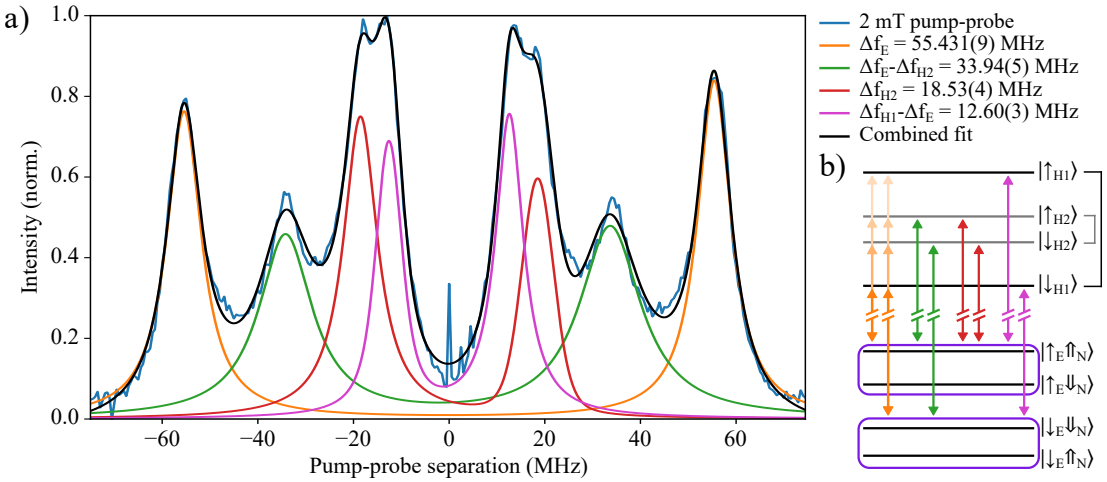

Figure 7.3: a) Two-colour PLE measurement at 2 mT showing the two-colour resonances for the 55.431(9) MHz electron spin splitting and 18.53(4) MHz hole spin splitting along with two resonance pairs for driving the B and C transitions of each orientation subset. b) Energy level diagram with the two-colour laser configurations for each set of resonances.

We performed a two-colour pump-probe PLE scan over a 150 MHz range with the 'pump' laser fixed at the centre of the inhomogeneous distribution. We find two-colour resonances corresponding to 55.431(9) MHz, 33.94(5) MHz, 18.53(4) MHz, and 12.60(3) MHz splittings. The largest splitting, 55.431(9) MHz, corresponds to the electron spin splitting Δf_E, with the nuclear spin not resolved. The lower frequency features include the mixed spin transition for each orientation $|\Delta f_E - \Delta f_{Hn}|$, and the hole spin splitting Δf_{H2}. We have denoted the subsets with the larger and smaller Δf_H as '1' and '2' respectively. Resonances for Δf_{H1} and $\Delta f_E + \Delta f_{Hn}$ were too weak to be seen.

We further measured the ensemble by two-colour PLE with a fixed frequency separation of Δf_E. This reveals a broad distribution with two clear peaks. Knowing that there are two distinct orientation subsets we fit the data with four Gaussian curves for $|\uparrow_{H1}\rangle$, $|\uparrow_{H2}\rangle$, $|\downarrow_{H1}\rangle$, and $|\downarrow_{H2}\rangle$. From the fit we find $\Delta f_{H1} = 70.3(6)$ MHz and $\Delta f_{H2} = 21(5)$ MHz, where Δf_{H2} is consistent with the 18.53(4) MHz observed from the pump-probe measurement.

We next perform two-colour pump-probe PLE by setting the pump frequency at an arbitrary location in the middle of the inhomogeneous distribution and scanning over the

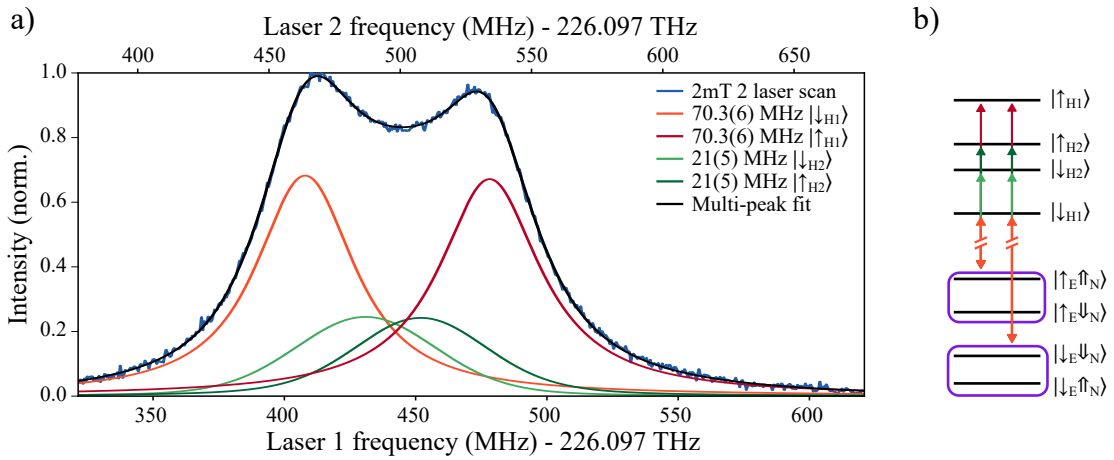

Figure 7.4: Two-laser scan at 2 mT with a frequency splitting equal to the electron spin splitting, showing the different lines for the hole spin of each orientation. The splitting between these lines for each orientation is 70.3(6) MHz and 21(5) MHz.

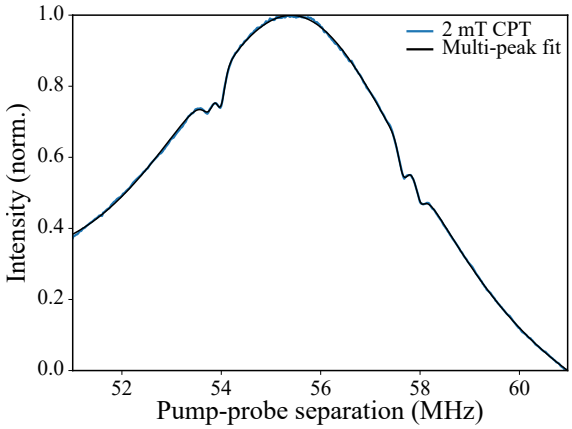

Centre (MHz)	Amp.	Linewidth (kHz)
53.754(1)	0.073(6)	366(9)
53.9938(5)	0.079(5)	186(4)
57.6581(4)	0.064(4)	208(5)
58.0103(7)	0.057(4)	256(5)

Figure 7.5: Initial measurement of optical CPT, fit using a multi-Voigt peak function. The fit properties for each dip are given in the table.

Δf_E resonance with the other laser frequency. This laser frequency configuration will create Λ-systems for each orientation subset, which we expect to produce CPT for different probe frequencies. Figure 7.5 shows the resulting peak with evident CPT resonances. The two dips at 53.754(1) MHz and 53.9938(5) MHz correspond to CPT from ground-state splitting 1 (see Fig. 7.2b) for each orientation. Similarly, we see CPT from ground-state splitting 4 for each orientation near 58 MHz. The resonance contrasts are all within 5-8%, which suggests that there is only ever a partial dark state formed. The linewidths are between 186 kHz and 366 kHz, much larger than both the $\sim$500 Hz spin dephasing, the 2.6 kHz laser linewidth bound, and the 5.6(2) kHz RF CPT linewidth we measured previously.

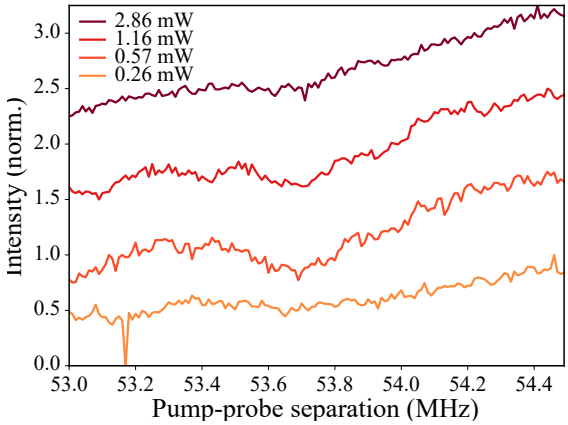

Figure 7.6: Power study of T-centre CPT, where the laser power was varied by a factor of ∼10. The best contrast was observed with a probe power of 0.57 mW, which is used for all following data.

7.3 Power Study

To improve these results we tested the effect of power broadening. All of the following data was taken on a separate day from the previous CPT data and the signal to noise was noticeably worse for the same settings. The pump laser was fixed at $P_{\text{pump}} = 10.46$ mW while we varied the probe power P_{probe} between 0.26 mW and 2.86 mW. Figure 7.6 shows a close-up of the most prominent CPT resonance. We saw a factor of ∼2 improvement in the visibility of the CPT dip with a P_{probe} of 0.57 mW, though we hit a limit in our signal to noise below this power. In these measurements, we did not observe a change in linewidth. No appreciable difference was noticed for changes in P_{pump} aside from altering the overall signal intensity. Following the power study all further scans used the lowered $P_{\text{probe}} = 0.57$ mW, while maintaining $P_{\text{pump}} = 10.46$ mW.

7.4 Isolating a Well-Resolved Orientation Subset

Next, we adjusted our pump-probe frequencies to isolate a single orientation subset (see Fig. 7.7). By configuring the pump-probe frequencies such that the Δf_E resonance is on the the high frequency edge of the inhomogeneous distribution, we target orientation subset 1 with $\Delta f_{H1} = 70.3(6)$ MHz, as shown in Figure 7.7b. For this configuration, the main CPT feature has 5.9(1)% contrast and a 96(18) kHz linewidth.

We used a multiple peak/dip fit (Fig. 7.7b, black line) to model the four-level system with two orientation subsets and two unresolved excited states each. This fit includes a Voigt profile with two negative Lorentzian peaks for each orientation. From this fit we determine the average homogeneous linewidth of the optical transitions is 7(3) MHz.

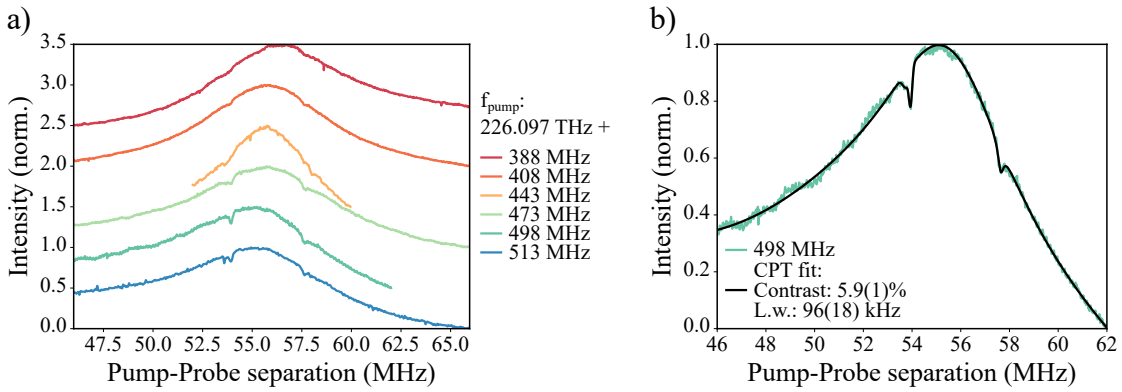

Figure 7.7: Probing different T-centre orientation CPT. a) Probe PLE spectra with evident CPT for various pump frequencies. b) The best isolation of single-orientation CPT with a contrast of 5.9(1)% and linewidth of 96(18) kHz.

7.5 Magnetic Field Study

We tested different magnitudes of magnetic field to see if the contrast or linewidth scaled with field. The pump frequency was reoptimized at each field to find the edge of the inhomogeneous distribution. The results of measuring CPT at different magnetic fields is shown in Figure 7.8.

The contrast of the CPT resonance for ground-state splitting 1 is tracked in Figure 7.8b, showing that the contrast peaks in the 0.5 mT to 1 mT range around 13% and plummets near zero field. The weak CPT response at zero field is in stark contrast to the zero-field response seen with RF fields. With low RF powers it was possible to completely resolve the ground state structure by ODMR. However, the ground state structure remains optically unresolved. As the magnetic field approaches zero, the optical CPT response dies out due to cross-excitation as all of the spin splittings fall beneath the homogeneous linewidth(see Fig. 7.9).

Cross-excitation can be incorporated into our three-level model for the T-centre as additional ground state dephasing and upwards relaxation from the ground state to the excited state. We estimate the cross-excitation rate from the Einstein rate coefficient determined for a detuning Δf_E from a Lorentzian line. For the 7(3) MHz homogeneous linewidth we observed, the cross-excitation rate is estimated to be 47% of the resonant Rabi frequency for the 0 mT splitting and 0.42% for the 2 mT field. Our model predicts contrasts of $\sim$ 1% and $\sim$ 88% for 0 mT and 2 mT respectively given these cross-excitation rates. While the model at 0 mT is close to the 2.4(1)% we observe, we measure significantly lower contrast at 2 mT than is predicted by the model.

Any misalignment in our field direction will lead to the separation of the different orientations in each subset. If this separation reaches the magnitude of the CPT linewidth for a single centre or larger, the observed contrast would be significantly smaller than

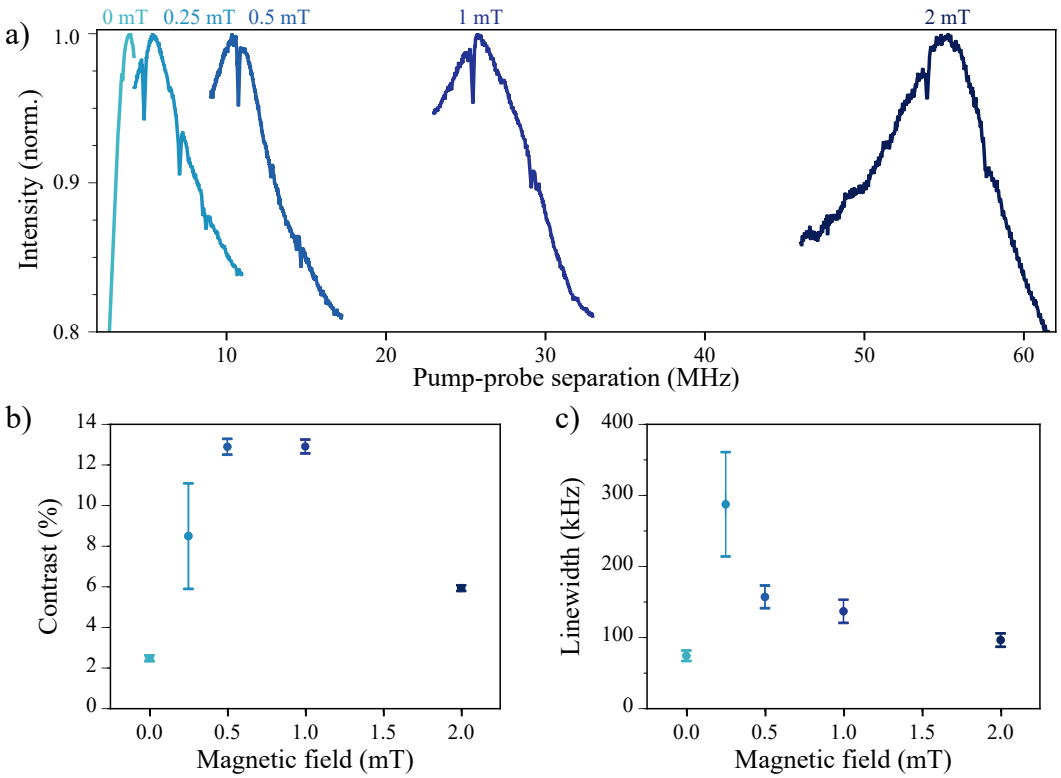

Figure 7.8: Magnetic field study of T-centre CPT. a) Optical CPT as observed for fields between 0 mT and 2 mT. The b) contrast and c) linewidth for CPT with ground-state splitting 1 with magnetic field. This CPT feature was chosen due to its proximity to the peak of two-colour resonance at all fields.

100%. For instance, if the orientational degeneracy of a subset was 6, then the contrast could be a factor of ~ 6 smaller than if a single orientation were addressed. We expect that this effect would scale with field as the errors become more pronounced with magnitude. To combat this we attempted to tune the field at 2 mT, though no indication of a field with improved contrast over what is reported here was found. The minimum step size of the HMP4040.04 in current is 0.1 mA, which corresponds to 50 nT.

In Figure 7.8c, we see that a similar pattern occurs in the CPT linewidth, though with the peak linewidth occuring at 0.25 mT. The decrease in linewidth with increased field suggests that there is no significant source of inhomogeneity or misalignment, which would scale with field. We do not currently understand the mechanism behind the large linewidths or their behavior with field. The linewidth could also be linked to a misalignment in the field, though we would expect the linewidth to increase as the contrast decreases and vice versa, which is not supported by the data.

We demonstrated the first optical CPT of the T-centre. This serves as a first step towards the development of T-centre optical control. A better understanding of why we observe small contrasts and large linewidths for optical CPT will be needed to determine the via-

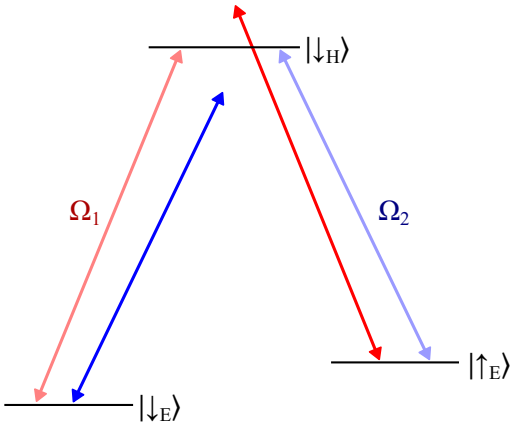

Figure 7.9: Cross-excitation in a three-level system. The light red and blue arrows represent resonant excitation between the ground states and the excited state by two lasers. The dark red and blue arrows represent the cross-excitation of each laser weakly addressing the opposite transition. The strength of the cross-excitation depends on the ground state splitting and transition linewidth.

bility of T-centre optical control schemes. If the lack of contrast is only linked to the cross-excitation and field misalignment affecting the inhomogeneous distribution, these problems can be avoided for optical control by implementing the far-detuned Raman scheme on single centres. However, if our ability to drive population into a dark state is inherently limited by some other mechanism, optical control will not be feasible.

Chapter 8

Conclusion

The characterization of silicon T-centre optical and spin properties has highlighted the T-centre's potential as a spin-photon interface. The techniques and apparatuses developed in this thesis demonstrate the fundamental techniques of optical control, and may enable all-optical control of the T-centre ground state in future work. This capability will expand the toolbox of operations available to T-centre quantum processors and networks.

We developed a model for the optically-addressable transitions of the T-centre, in which we predicted that the far-detuned Raman pulse scheme could achieve fidelities in excess of 99.9% for single T-centres at 1.5 K and optical powers of 2.6 µW. These simulations demonstrated the viability of observing optical Rabi oscillations. Based on this model and the available apparatuses we decided to use ensembles of T-centres in isotopically-purified ^{28}Si for the entirety of the experimental work.

We developed a multi-channel ultra-stable tunable laser capable of producing two independent optical fields that can be pulsed on time scales as short as 2.5 ns. We determined the linewidth of this laser to be < 2.6 kHz compared to the unlocked 1–2 MHz linewidth, and added amplification to reach powers of 0.83(2) W. Two new magnetic field apparatuses were developed for tuning the external magnetic field of the samples.

We conducted the first demonstration of Rabi oscillations for T-centre optical transitions with Rabi frequencies up to 7 MHz. The Rabi visibility was limited by an unexpectedly large homogeneous linewidth (10.1(1) MHz). We suspect that the temperature was elevated, and future studies with the low-temperature linewidth ($\sim$ 0.69 MHz) are expected to resolve more than four Rabi oscillations. In taking these measurements we observed, for the first time, two distinct electron spin g-factors of 2.0052(4) and 2.002(1) from two different T-centre orientations, demonstrating a small anisotropy in g_e.

ODMR spectra we took of the ground state was fit by Joshua Kanaganayagam to find the anisotropic hyperfine tensor is

$$\begin{bmatrix} -4.03\ \text{MHz} & 0 & 0 \\ 0 & -2.93\ \text{MHz} & 0 \\ 0 & 0 & 4.50\ \text{MHz} \end{bmatrix}, \tag{8.0.1}$$

in its diagonalized basis [34].

Finally, we demonstrated the first instance of optically-driven CPT of the T-centre. We measured unexpectedly low contrast and high linewidths without a clear cause. The possible mechanisms we discussed, cross-excitation and orientation separation due to field misalignment, should not affect the optical control operational parameters for single T-centres under the far-detuned scheme. Further investigation into the behavior of optical CPT on single cavity-coupled T-centres at 1 K (where we expect lifetime limited linewidths) should help to illuminate the mechanisms behind this behavior.

Future studies motivated by this work will characterize optical control for single centres. Measuring single, homogeneous centres of a known orientation removes two major sources of uncertainty from the measurements presented here. Newly upgraded apparatuses will allow the measurement of single centres at 1 K confocally [27] and in integrated optical resonators [63]. These studies may lead to the experimental implementation of the optical control scheme simulated in this thesis.

Bibliography

[1] Igor Aharonovich, Dirk Englund, and Milos Toth. "Solid-state single-photon emitters". In: *Nature Photonics* 10.10 (2016), pp. 631–641. ISSN: 17494893. DOI: 10.1038/nphoton.2016.186.

[2] Jesús Arjona Martínez et al. "Photonic Indistinguishability of the Tin-Vacancy Center in Nanostructured Diamond". In: *Physical Review Letters* 129.17 (Oct. 2022), p. 173603. ISSN: 0031-9007. DOI: 10.1103/PhysRevLett.129.173603. URL: http://arxiv.org/abs/2206.15239https://link.aps.org/doi/10.1103/PhysRevLett.129.173603.

[3] Frank Arute et al. "Quantum supremacy using a programmable superconducting processor". In: *Nature* 574.7779 (Oct. 2019), pp. 505–510. ISSN: 0028-0836. DOI: 10.1038/s41586-019-1666-5. URL: http://www.nature.com/articles/s41586-019-1666-5.

[4] K. J. Åström and T. Hägglund. "The future of PID control". In: *Control Engineering Practice* 9.11 (2001), pp. 1163–1175. ISSN: 09670661. DOI: 10.1016/S0967-0661(01)00062-4.

[5] David D. Awschalom et al. "Quantum technologies with optically interfaced solid-state spins". In: *Nature Photonics* 12.9 (Sept. 2018), pp. 516–527. ISSN: 1749-4885. DOI: 10.1038/s41566-018-0232-2. URL: http://www.nature.com/articles/s41566-018-0232-2.

[6] Jonas N. Becker et al. "All-Optical Control of the Silicon-Vacancy Spin in Diamond at Millikelvin Temperatures". In: *Physical Review Letters* 120.5 (2018), pp. 1–6. ISSN: 10797114. DOI: 10.1103/PhysRevLett.120.053603.

[7] Jonas Nils Becker et al. "Ultrafast all-optical coherent control of single silicon vacancy colour centres in diamond". In: *Nature Communications* 7 (2016), pp. 1–6. ISSN: 20411723. DOI: 10.1038/ncomms13512.

[8] P. Becker et al. "Enrichment of silicon for a better kilogram". In: *physica status solidi (a)* 207.1 (Jan. 2010), pp. 49–66. ISSN: 18626300. DOI: 10.1002/pssa.200925148. URL: https://onlinelibrary.wiley.com/doi/10.1002/pssa.200925148.

[9] Charles H. Bennett and Gilles Brassard. "Quantum cryptography: Public key distribution and coin tossing". In: *Theoretical Computer Science* 560.P1 (Dec. 2014), pp. 7–11. ISSN: 03043975. DOI: 10.1016/j.tcs.2014.05.025. URL: https://linkinghub.elsevier.com/retrieve/pii/S0304397514004241.

[10] L. Bergeron et al. "Silicon-Integrated Telecommunications Photon-Spin Interface". In: *PRX Quantum* 1.2 (Oct. 2020), p. 020301. DOI: 10.1103/prxquantum.1.020301. URL: https://journals.aps.org/prxquantum/abstract/10.1103/PRXQuantum.1.020301.

[11] Klaas Bergmann, Nikolay V. Vitanov, and Bruce W. Shore. *Perspective: Stimulated Raman adiabatic passage: The status after 25 years*. May 2015. DOI: 10.1063/1.4916903. URL: http://dx.doi.org/10.1063/1.4916903].

[12] H. Bernien et al. "Heralded entanglement between solid-state qubits separated by three metres". In: *Nature* 497.7447 (Apr. 2013), pp. 86–90. ISSN: 00280836. DOI: 10.1038/nature12016. URL: https://www.nature.com/articles/nature12016.

[13] Eric D. Black. "An introduction to Pound–Drever–Hall laser frequency stabilization". In: *American Journal of Physics* 69.1 (2001), pp. 79–87. ISSN: 0002-9505. DOI: 10.1119/1.1286663.

[14] H.-J. Briegel et al. "Quantum repeaters: The role of imperfect local operations in quantum communication". In: *Physical Review Letters* 81.26 (Dec. 1998), pp. 5932–5935. ISSN: 0031-9007. DOI: 10.1103/PhysRevLett.81.5932. URL: http://link.aps.org/doi/10.1103/PhysRevLett.81.5932.

[15] B.H. Calhoun et al. "Digital Circuit Design Challenges and Opportunities in the Era of Nanoscale CMOS". In: *Proceedings of the IEEE* 96.2 (Feb. 2008), pp. 343–365. ISSN: 0018-9219. DOI: 10.1109/JPROC.2007.911072. URL: http://ieeexplore.ieee.org/document/4403891/.

[16] Manuel Cardona and M. L. W. Thewalt. "Isotope effects on the optical spectra of semiconductors". In: *Rev. Mod. Phys.* 77.4 (Nov. 2005), pp. 1173–1224. URL: https://link.aps.org/doi/10.1103/RevModPhys.77.1173papers3://publication/doi/10.1103/RevModPhys.77.1173.

[17] C. Chartrand et al. "Highly enriched Si 28 reveals remarkable optical linewidths and fine structure for well-known damage centers". In: *Physical Review B* 98.19 (Nov. 2018), p. 195201. ISSN: 2469-9950. DOI: 10.1103/PhysRevB.98.195201. URL: https://link.aps.org/doi/10.1103/PhysRevB.98.195201.

[18] Qi Ming Chen and Re Bing Wu. "Optimized all-optical control of single spin quantum dynamics in diamond". In: *IFAC-PapersOnLine* 50.1 (2017), pp. 11755–11759. ISSN: 24058963. DOI: 10.1016/j.ifacol.2017.08.1983. URL: https://doi.org/10.1016/j.ifacol.2017.08.1983.

[19] Yu Ao Chen et al. "An integrated space-to-ground quantum communication network over 4,600 kilometres". In: *Nature* 589.7841 (Jan. 2021), pp. 214–219. ISSN: 14764687. DOI: 10.1038/s41586-020-03093-8. URL: https://doi.org/10.1038/s41586-020-03093-8.

[20] L. Childress et al. "Coherent Dynamics of Coupled Electron and Nuclear Spin Qubits in Diamond". In: *Science* 314.5797 (Oct. 2006), pp. 281–285. ISSN: 0036-8075. DOI: 10.1126/science.1131871. URL: https://www.science.org/doi/10.1126/science.1131871.

[21] A DeAbreu et al. "Waveguide-integrated silicon T centres". In: *arXiv:2209.14260v1* (2022). URL: https://arxiv.org/abs/2209.14260.

[22] Dapeng Ding et al. "Coherent Optical Control of a Quantum-Dot Spin-Qubit in a Waveguide-Based Spin-Photon Interface". In: *Physical Review Applied* 11.3 (Mar. 2019), p. 031002. ISSN: 23317019. DOI: 10.1103/PhysRevApplied.11.031002. URL: https://journals.aps.org/prapplied/abstract/10.1103/PhysRevApplied.11.031002.

[23] C J Foot. *Atomic Physics*. Oxford University Press, 2005.

[24] Michael Hanks, William J. Munro, and Kae Nemoto. "Optical manipulation of the negative silicon-vacancy center in diamond". In: *Physical Review A* 102.2 (Aug. 2020), p. 022616. ISSN: 2469-9926. DOI: 10.1103/physreva.102.022616. URL: https://journals.aps.org/pra/abstract/10.1103/PhysRevA.102.022616.

[25] Aram W. Harrow, Avinatan Hassidim, and Seth Lloyd. "Quantum Algorithm for Linear Systems of Equations". In: *Physical Review Letters* 103.15 (Oct. 2009), p. 150502. ISSN: 0031-9007. DOI: 10.1103/PhysRevLett.103.150502. URL: https://link.aps.org/doi/10.1103/PhysRevLett.103.150502.

[26] B. Hensen et al. "Loophole-free Bell inequality violation using electron spins separated by 1.3 kilometres". In: *Nature* 526 (2015), pp. 682–686. DOI: 10.1038/nature15759. URL: doi:10.1038/nature15759.

[27] D. B. Higginbottom et al. "Optical observation of single spins in silicon". In: *Nature* 607 (2022), pp. 266–270. DOI: 10.1038/s41586-022-04821-y. URL: https://doi.org/10.1038/s41586-022-04821-y.

[28] E Irion et al. "The defect luminescence spectrum at 0.9351 eV in carbon-doped heat-treated or irradiated silicon". In: *Journal of Physics C: Solid State Physics* 18.26 (Sept. 1985), pp. 5069–5082. URL: http://iopscience.iop.org/article/10.1088/0022-3719/18/26/018papers3://publication/doi/10.1088/0022-3719/18/26/018.

[29] F. Jelezko et al. "Observation of Coherent Oscillation of a Single Nuclear Spin and Realization of a Two-Qubit Conditional Quantum Gate". In: *Physical Review Letters* 93.13 (Sept. 2004), p. 130501. ISSN: 0031-9007. DOI: 10.1103/PhysRevLett.93.130501. URL: https://link.aps.org/doi/10.1103/PhysRevLett.93.130501.

[30] J. R. Johansson, P. D. Nation, and Franco Nori. "QuTiP: An open-source Python framework for the dynamics of open quantum systems". In: *Computer Physics Communications* 183.8 (Oct. 2011), pp. 1760–1772. ISSN: 00104655. DOI: 10.1016/j.cpc.2012.02.021. URL: http://arxiv.org/abs/1110.0573http://dx.doi.org/10.1016/j.cpc.2012.02.021.

[31] Richard Jozsa and Noah Linden. "On the role of entanglement in quantum-computational speed-up". In: *Proceedings of the Royal Society A: Mathematical, Physical and Engineering Sciences* 459.2036 (2003), pp. 2011–2032. ISSN: 14712946. DOI: 10.1098/rspa.2002.1097.

[32] Dawon Kahng and Martin M Atalla. *Semiconductor devices having dielectric coatings & Electric field controlled semiconductor device*. 1960.

[33] Benjamin Kambs and Christoph Becher. "Limitations on the indistinguishability of photons from remote solid state sources". In: *New Journal of Physics* 20.11 (Nov. 2018), p. 115003. ISSN: 13672630. DOI: 10.1088/1367-2630/aaea99. URL: https://doi.org/10.1088/1367-2630/aaea99.

[34] J. Kanaganayagam. "The silicon T centre hyperfine tensor and a proposal for coherence protection". MA thesis. Simon Fraser University, 2023.

[35] D. Karaiskaj et al. "Photoluminescence of Isotopically Purified Silicon: How Sharp are Bound Exciton Transitions?" In: *Physical Review Letters* 86.26 (June 2001), p. 6010. ISSN: 00319007. DOI: 10.1103/PhysRevLett.86.6010. URL: https://journals.aps.org/prl/abstract/10.1103/PhysRevLett.86.6010.

[36] Jack S. Kilby. "Invention of the Integrated Circuit". In: *IEEE Transactions on Electron Devices* 23.7 (1976), pp. 648–654. ISSN: 15579646. DOI: 10.1109/T-ED.1976.18467.

[37] Danny Kim et al. "Ultrafast optical control of entanglement between two quantum-dot spins". In: *Nature Physics* 7.3 (2011), pp. 223–229. ISSN: 17452481. DOI: 10.1038/nphys1863.

[38] Morten Kjaergaard et al. "Superconducting Qubits: Current State of Play". In: *Annual Review of Condensed Matter Physics* 11 (2020), pp. 369–395. ISSN: 19475462. DOI: 10.1146/annurev-conmatphys-031119-050605.

[39] Kevin Krewell. "IBM Prepares For Quantum Computing Inflection Point". In: *Forbes* (2022). URL: https://www.forbes.com/sites/tiriasresearch/2022/11/17/ibm-prepares-for-quantum-computing-inflection-point.

[40] Peter Lambropoulos and David Petrosyan. *Fundamentals of quantum optics and quantum information*. Heidelberg: Springer, 2007.

[41] G. de Lange et al. "Universal Dynamical Decoupling of a Single Solid-State Spin from a Spin Bath". In: *Science* 330.6000 (Oct. 2010), pp. 60–63. ISSN: 0036-8075. DOI: 10.1126/science.1192739. URL: https://www.science.org/doi/10.1126/science.1192739.

[42] H. H. Li. "Refractive index of silicon and germanium and its wavelength and temperature derivatives". In: *Journal of Physical and Chemical Reference Data* 9.3 (July 1980), pp. 561–658. ISSN: 0047-2689. DOI: 10.1063/1.555624. URL: http://aip.scitation.org/doi/10.1063/1.555624.

[43] Julius Edgar Lilienfeld. *Method and apparatus for controlling electric currents*. 1925.

[44] Hanne Ludvigsen, Mika Tossavainen, and Matti Kaivola. "Laser linewidth measurements using self-homodyne detection with short delay". In: *Optics Communications* 155.1-3 (Oct. 1998), pp. 180–186. ISSN: 00304018. DOI: 10.1016/S0030-4018(98)00355-1. URL: https://linkinghub.elsevier.com/retrieve/pii/S0030401898003551.

[45] E R MacQuarrie et al. "Generating T centres in photonic silicon-on-insulator material by ion implantation". In: *New Journal of Physics* 23.10 (2021), p. 103008. ISSN: 1367-2630. DOI: 10.1088/1367-2630/ac291f.

[46] Lars S. Madsen et al. "Quantum computational advantage with a programmable photonic processor". In: *Nature* 606.7912 (June 2022), pp. 75–81. ISSN: 0028-0836. DOI: 10.1038/s41586-022-04725-x. URL: https://www.nature.com/articles/s41586-022-04725-x.

[47] F. Mangini et al. "Experimental observation of self-imaging in SMF-28 optical fibers". In: *Optics Express* 29.8 (Apr. 2021), p. 12625. ISSN: 1094-4087. DOI: 10.1364/OE.419472. URL: https://opg.optica.org/abstract.cfm?URI=oe-29-8-12625.

[48] N. S. Minaev and A. V. Mudryi. "Thermally-induced defects in silicon containing oxygen and carbon". In: *Physica Status Solidi (a)* 68.2 (1981), pp. 561–565. ISSN: 1521396X. DOI: 10.1002/pssa.2210680227.

[49] K.J. Morse et al. "A photonic platform for donor spin qubits in silicon". In: *Science Advances* 3.7 (2017). ISSN: 23752548. DOI: 10.1126/sciadv.1700930. URL: https://www.science.org/doi/10.1126/sciadv.1700930.

[50] K. Muller et al. "All optical quantum control of a spin-quantum state and ultrafast transduction into an electric current". In: *Scientific Reports* 3.i (2013), pp. 1–7. ISSN: 20452322. DOI: 10.1038/srep01906.

[51] Michael A. Nielsen and Isaac L. Chuang. *Quantum Computation and Quantum Information*. Cambridge University Press, 2010. ISBN: 978-1-107-00217-3.

[52] T. E. Northup and R. Blatt. "Quantum information transfer using photons". In: *Nature Photonics* 8.5 (2014), pp. 356–363. ISSN: 17494893. DOI: 10.1038/nphoton.2014.53.

[53] N. A. Olsson. "Lightwave Systems With Optical Amplifiers". In: *Journal of Lightwave Technology* 7.7 (1989), pp. 1071–1082. ISSN: 15582213. DOI: 10.1109/50.29634.

[54] W. Pfaff et al. "Unconditional quantum teleportation between distant solid-state quantum bits". In: *Science* 345.6196 (2014). URL: http://science.sciencemag.org/content/345/6196/532.full.

[55] David Press et al. "Complete quantum control of a single quantum dot spin using ultrafast optical pulses". In: *Nature* 456.7219 (Nov. 2008), pp. 218–221. ISSN: 0028-0836. DOI: 10.1038/nature07530. URL: http://www.nature.com/articles/nature07530.

[56] A N Safonov et al. "Interstitial-Carbon Hydrogen Interaction in Silicon". In: *Phys. Rev. Lett.* 77.23 (Dec. 1996), pp. 4812–4815. URL: https://link.aps.org/doi/10.1103/PhysRevLett.77.4812papers3://publication/doi/10.1103/PhysRevLett.77.4812.

[57] Max Schulz. "The end of the road for silicon?" In: *Nature* 399.6738 (June 1999), pp. 729–730. ISSN: 0028-0836. DOI: 10.1038/21526. URL: https://www.nature.com/articles/21526.

[58] A. Schweiger and G. Jeschke. *Principles of pulsed electron paramagnetic resonance*. 2001.

[59] D. Serrano et al. "All-optical control of long-lived nuclear spins in rare-earth doped nanoparticles". In: *Nature Communications* 9.1 (2018), pp. 1–7. ISSN: 20411723. DOI: 10.1038/s41467-018-04509-w. URL: http://dx.doi.org/10.1038/s41467-018-04509-w.

[60] Peter W. Shor. "Algorithms for quantum computation: Discrete logarithms and factoring". In: *Proceedings - Annual IEEE Symposium on Foundations of Computer Science, FOCS* (1994), pp. 124–134. ISSN: 02725428. DOI: 10.1109/SFCS.1994.365700.

[61] Daniel Adam Steck. *Quantum and Atom Optics*. 2007, pp. 143–147. URL: http://www.opencontent.org/openpub/%0Ahttp://steck.us/teaching.

[62] M Steger et al. "High-resolution absorption spectroscopy of the deep impurities S and Se in Si-28 revealing the Se-77 hyperfine splitting". In: *Phys. Rev. B.* 80.11 (Sept. 2009), p. 115204. URL: http://link.aps.org/doi/10.1103/PhysRevB.80.115204papers3://publication/doi/10.1103/PhysRevB.80.115204.

[63] L. A. Stott. "Thesis In Progress". PhD thesis. Simon Fraser University, 2022.

[64] Pramode K Verma et al. *Multi-photon Quantum Secure Communication*. Springer, 2019. ISBN: 9789811086175. URL: http://www.springer.com/series/4748.

[65] G. Waldherr et al. "Quantum error correction in a solid-state hybrid spin register". In: *Nature* 506.7487 (Feb. 2014), pp. 204–207. ISSN: 0028-0836. DOI: 10.1038/nature12919. URL: http://www.nature.com/articles/nature12919.

[66] Peter J. Winzer, David T. Neilson, and Andrew R. Chraplyvy. "Fiber-optic transmission and networking: the previous 20 and the next 20 years [Invited]". In: *Optics Express* 26.18 (Sept. 2018), p. 24190. ISSN: 1094-4087. DOI: 10.1364/OE.26.024190. URL: https://opg.optica.org/abstract.cfm?URI=oe-26-18-24190.

[67] Stephen Wolfram. *The mathematica book*. 1st ed. Wolfram Research, Inc., 2003.

[68] Christopher G Yale et al. "All-optical control of a solid-state spin using coherent dark states". In: *PNAS* 110 (2013). DOI: 10.1073/pnas.1305920110.

[69] A. Yang et al. "Homogeneous linewidth of the P31 bound exciton transition in silicon". In: *Applied Physics Letters* 95.12 (Sept. 2009), p. 122113. ISSN: 0003-6951. DOI: 10.1063/1.3238268. URL: https://aip-scitation-org.proxy.lib.sfu.ca/doi/abs/10.1063/1.3238268.

[70] A. Yang et al. "Optical Detection and Ionization of Donors in Specific Electronic and Nuclear Spin States". In: *Physical Review Letters* 97.22 (Nov. 2006), p. 227401. ISSN: 0031-9007. DOI: 10.1103/PhysRevLett.97.227401. URL: https://link.aps.org/doi/10.1103/PhysRevLett.97.227401.

[71] Han-Sen Zhong et al. "Quantum computational advantage using photons". In: *Science* (Dec. 2020). DOI: 10.1126/science.abe8770. URL: http://science.sciencemag.org/.

[72] Tian Zhong et al. "Optically Addressing Single Rare-Earth Ions in a Nanophotonic Cavity". In: *Physical Review Letters* 121.18 (Oct. 2018), pp. 1–11. ISSN: 10797114. DOI: 10.1103/PhysRevLett.121.183603.